PARTICULATE EMISSIONS BY H.P.D.I. ENGINES USING THERMOPHORETIC SAMPLING AND ELECTRON MICROSCOPY

By

Anil Kumar Nair

B.Tech. (Mech. Eng.) University of Kerala, India, 1992

M.Tech. (Mech. Eng.) University of Calicut, India, 1996

A THESIS SUBMITTED IN PARTIAL FULFILLMENT OF

THE REQUIREMENTS FOR THE DEGREE OF

MASTER OF APPLIED SCIENCE

in

THE FACULTY OF GRADUATE STUDIES

DEPARTMENT OF MECHANICAL ENGINEERING

We accept this thesis as conforming

to the required standard

THE UNIVERSITY OF BRITISH COLUMBIA

April, 2001

In presenting this thesis in partial fulfilment of the requirements for an advanced degree at the University of British Columbia, I agree that the Library shall make it freely available for reference and study. I further agree that permission for extensive copying of this thesis for scholarly purposes may be granted by the head of my department or by his or her representatives. It is understood that copying or publication of this thesis for financial gain shall not be allowed without my written permission.

Department of Mechanical Engineering

The University of British Columbia
Vancouver, Canada

Date April 27, 2001

DE-6 (2/88)

ABSTRACT

A particulate sampler was designed and built for sampling particulate material from engines, on to the Transmission Electron Microscope (TEM) grids. It was designed taking into account all the challenges from different points of view of fluid mechanics, heat transfer, emission statistics, aerosol mechanics and practicability. Several instruments like temperature controller, temperature indicator, heating wire, flowmeter, valves, thermocouples and suitable conduits and other accessories for the passage of hot exhaust gas from engines were connected to the sampler to set up a thermophoretic sampling system. The intended application of the sampling system was to help in getting a good idea about parameters of interest in aerosol behaviour like particle size range, particle number concentration on the grid, particle shapes, spherule dimensions and chemical composition for the exhaust particulate material from the High Pressure Direct Injection (HPDI) engines - the compression ignition engines using natural gas as the fuel. Sampling tests were conducted in HPDI engines at different load conditions, different speed conditions and different conditions of pilot pulse-width. The particles in the grids were examined carefully with the TEM and measurements were taken. The results have been compiled and reported in this thesis. The particle average number concentration as deposited on the grid increased with increasing load conditions and increasing quantities of pilot diesel fuel consumption. Particle size ranged from about 15 nm to about 20 microns in some cases. Due to the presence of enormous number of tiny particles and single independent spherules, their number concentration could not be accurately measured using visual assessments. However, the number concentrations of particles larger than 500 nm could be found out in all cases except at 85% load condition in an engine. The spherules were of different sizes and their sizes ranged from about 15 nm to 1.5 microns in some cases. Generally, the single independent spherules were smaller in size compared to those in the agglomerates of particles. Several notable features of the particles were found during the analyses and they are reported in the results. Some assumptions were made in designing the sampler and in computing its deposition efficiency. Actual deposition was 10-20% of predicted values. The major sources of error

are also mentioned. Descriptions of some notable micrographs are presented. The data collected during the analyses were thoroughly analyzed to reach conclusions regarding the performance of the sampler and particulate emission by HPDI engines.

The research project has brought to light many aspects of particulate emission by HPDI engines and has helped in preparing a database on it.

TABLE OF CONTENTS

LIST OF FIGURES

LIST OF TABLES

ACKNOWLEDGEMENT

With great pleasure, I take this opportunity to express my heartfelt gratitude to my supervisors, Dr. S. N. Rogak and Dr. P. G. Hill, Associate Professor and Professor Emeritus respectively, at the Department of Mechanical Engineering, University of British Columbia, Canada. I am extremely indebted to Dr. S. N. Rogak, who took a genuine interest in my research work and provided the required guidance. I am truly thankful to Dr. P. G. Hill for the interest and encouragement rendered to me during the research work.

I express my sincere thanks to the staff of Westport Innovations Inc., Vancouver, Canada, for their interest and help in carrying out the sampling tests in engines. I would also like to thank the staff at the Machine Shop, Department of Mechanical Engineering, University of British Columbia, for the invaluable help in fabricating the particulate sampler needed for the tests.

I owe much to my parents for the continuous encouragement they provided throughout the period.

This thesis has gained numerous ideas from many books and journals. I express my thanks to all the authors.

Finally, I thank all, who have directly or indirectly helped me at different stages of my work.

Chapter 1

Introduction and Background

1.1 Exhaust Particulate Material

An aerosol is suspended solid or liquid particles in a gas [Hinds,1999]. There is wide variation in the particle size distribution in the atmosphere. Larger particles tend to originate from the natural sources like rock/soil debris, forest fires, sea salt spray and volcanic debris among others. The particulate matter in the atmosphere in the inhalable range (smaller particles) is contributed mostly by exhaust emissions from vehicles and industrial processes. Particulate matter found in the atmosphere can be divided into the following categories:

- PM 10 (particulates with an aerodynamic diameter of less than 10 μm)
- Fine particles (particulates with diameters below 2.5 μm)
- Ultrafine particles (particulates with diameters below 100 nm)
- Nanoparticles (particulates with diameters below 50 nm)

According to the California Air Resources Board (CARB), exhaust particulate matter is defined as follows: "Particulates are all exhaust components (with the exception of condensed water) that are deposited on a defined filter after having been diluted with air to a temperature below 51.7°C" [Schafer et al., 1995]. Particulates consist of solid (organically insoluble) and liquid (organically soluble) phases. The solid phase consists of (1) soot in the form of amorphous carbon, ash, oil additives, corrosion products and abrasion products (2) sulphates and their molecule-bound water. The liquid phase consists of fuel and lubricant contents that are combined with soot in most cases. The hydrocarbons contained in the hot exhaust still are largely gaseous and are converted into a liquid, organically soluble phase (particulates) only after having been cooled by turbulent intermixing with air [Schafer et al., 1995].

Internal combustion engines are contributors to atmospheric pollution in the form of particulate emissions. Particle size distributions from internal combustion engines have received attention due to the possible adverse effects of fine particles on human health.

Basically, soot emissions are part of particulate emissions. The particulate composition is largely dependent on the operating point and the combustion process [Schafer et al., 1995]. Soot emission from spark-ignition (SI) engines can result from combustion of overly rich mixtures of air and fuel. However, soot in the exhaust is not a significant problem in properly adjusted SI engines [Heywood, 1988].

1.1.1 Particulate emission from diesel engines

Diesel particulates consist of combustion generated carbonaceous material (soot) on which some organic compounds have been absorbed [Heywood, 1988]. Most particulate material (PM) comes from incomplete combustion of fuel hydrocarbons [Heywood, 1988]. The lubricating oil also contributes to the particulate emission from diesel engines [Heywood, 1988]. Soot formation occurs during rich combustion of hydrocarbon fuel. This rich combustion or air deficiency is present locally inside diesel engines. A separation of hydrogen leads to C-structures showing an increasing lack of hydrogen. Polymerization processes lead to formation of molecules rich in carbon that form soot particulates [Schafer et al., 1995]. The various stages of soot particle generation and growth are [Heywood, 1988] :

- Particle formation: The first condensed phase material arises from the fuel molecules via their oxidation and/or pyrolysis products. These products typically include various unsaturated hydrocarbons, particularly acetylene and its higher analogues and polycyclic aromatic hydrocarbons. These two types of molecules are considered the most likely precursors of soot in flames. The condensation reactions of gas-phase species such as these lead to the appearance of the first recognizable soot particles, often called nuclei. These preliminary particles are very small (diameter less than 2 nm) and the formation of large numbers of them involve negligible soot loading in the region of their formation.
- Particle growth: Surface growth, coagulation and aggregation takes place. Surface growth involves the attachment of gas-phase species to the surface of particles and

their incorporation into the particulate phase. During coagulation, collision and coalescence of particles occur. Later, the particles aggregate into chains and clusters.

- At each stage in the processes mentioned above, oxidation can occur where soot or soot precursors are burned in the presence of oxidizing species to form gaseous products such as CO and CO_2. The eventual emission of soot from the engine will depend on the balance of these processes of formation and burnout. The emitted soot is then subjected to a further mass addition process as the exhaust gases cool and are diluted with air. Adsorption into the soot particle surface and condensation to form new particles of hydrocarbon species in the exhaust gases occur in the exhaust system and in the dilution tunnel which simulates what happens in the atmosphere.

The emission rates of PM should be below 0.1 g/bhp-hr as per EPA (Environmental Protection Agency) regulations [Automotive Handbook, 3rd edition]. The composition of PM depends on the conditions in the engine exhaust and particulate collection system. At temperatures above 500°C, the individual particles are principally clusters of many spherules of carbon (with a small amount of hydrogen) with individual spherule diameters of about 15 to 30 nm [Heywood, 1988]. As temperatures decrease below 500°C, the particles become coated with absorbed and condensed high molecular weight organic compounds which include unburned hydrocarbons, oxygenated hydrocarbons (ketones, esters, ethers, organic acids) and polynuclear aromatic hydrocarbons [Heywood, 1988]. The condensed material also includes inorganic species such as sulphur dioxide, nitrogen dioxide and sulphuric acid (sulphates) [Heywood, 1988].

The formation process starts with a fuel molecule containing 12 to 22 carbon atoms and a H/C ratio of about 2 and ends up with particles typically a few hundred nanometers in diameter, composed of spherules 20 to 30 nanometer in diameter each containing some 10^5 carbon atoms and having a H/C ratio of about 0.1 [Heywood, 1988]. The characteristics of diesel combustion like the high gas temperatures and pressures, complex fuel composition, dominance of turbulent mixing, the unsteady process and the three-dimensional geometry make it unsuitable for detailed fundamental studies

[Heywood, 1988]. Soot formation generally takes place in diesel combustion environment at temperatures between about 1000 and 2800 K, at pressures of 50 to 100 atm and with sufficient air overall to burn fully all the fuel [Heywood, 1988]. The time available for the formation of solid soot particles from a fraction of the fuel is in the order of milliseconds.

1.1.2 Methods for reducing particulate emission in diesel engines

In diffusion flames, the higher the temperature, the greater is the amount of soot formed (in contrast to the premixed flames). But the soot is largely oxidized as it passes through the flame front into the oxidizer. In diesel engines, usually the measures that decrease NO_x emissions (related to decreasing temperature) generally increase particulate emissions. Soot emissions can be limited using fuel additives, such as some metals (nickel, sodium, potassium). These metals have a low enough ionization potential that they become charged at flame temperatures. The soot then takes on positive and negative charges. Dissimilar charges accelerate soot coagulation and like charges retard the coagulation. The net effect is that coagulation is reduced, the soot particles do not grow and therefore have a larger surface area for oxidation. An exhaust treatment technology that substantially reduces diesel engine particulate emissions is the trap oxidizer. A temperature-tolerant filter or trap removes the particulate material from the exhaust gas; the filter is then cleaned off by oxidizing the accumulated particles. But the filter increases the pressure in the exhaust system. Also, under normal diesel engine operating conditions, the collected particulate matter will not ignite and oxidize. Types of particulate filters include ceramic monoliths, alumina-coated wire mesh, ceramic foam and ceramic fibre mat.

The contribution of diesel engines to atmospheric particulate concentration points to the need for using a more environmentally benign fuel in compression ignition engines. The immediate and viable option at present is natural gas. Natural gas plays a significant role in many parts of the world as a clean-burn, cheap and abundant fuel [Walsh et al., 1997]. Natural gas has less carbon content compared to diesel and hence produces less

soot during combustion. But it cannot be directly used in place of diesel in diesel engines due to some operational difficulties - the details of which are discussed in the following section. Dual-fuel diesel engines are a special type of lean-burn engine in which the air-gas mixture in the cylinder is ignited by injection of a small amount of diesel fuel that self-ignites [Walsh et al., 1997]. Westport innovations Inc., Vancouver, Canada, has developed a fuel injection technology called the HPDI (High Pressure Direct Injection) for using natural gas in diesel engines with minimal engine modifications. This technology effectively addresses all problems associated with natural gas combustion in a typical diesel engine. The details of this technology are mentioned in the following section.

1.2 The H.P.D.I. (High Pressure Direct Injection) Technology

Westport's fuel injection technology basically consists of an injector that supplies an engine cylinder with a small amount of diesel fuel and almost simultaneously a larger amount of natural gas. Thus traditional diesel air compression ignites the diesel fuel. The natural gas is ignited by the diesel fuel and provides the force for the engine's power stroke. The technology works with either CNG or LNG [Douville et al, 1998].

Westport's fuel system replaces nearly all oil-based diesel fuel with natural gas while retaining traditional diesel power and performance. The ratio of natural gas to diesel fuel is electronically controlled for an optimum mix of engine performance, fuel economy and emissions reduction. Natural gas typically constitutes upward of 90% of the fuel supply in the Westport system [Douville et al, 1998].

In addition to the fuel injectors, Westport's fuel delivery system requires the installation of electronic controls and a fuel pump [Douville et al, 1998]. In a vehicle, a storage tank for natural gas is required. For power generation, the engine would typically receive natural gas from a pipeline.

There were mainly two significant technology barriers that hindered the adaptation of diesel engines from diesel fuel to natural gas. One is that natural gas needs help to ignite at the pressures and temperatures in the combustion chamber of a typical diesel engine. The other is that natural gas needs help to force its way into a pressurized diesel engine cylinder [Douville et al, 1998]. As mentioned earlier, Westport's High Pressure Direct Injection Technology (HPDI) overcomes the natural gas ignition barrier by injecting a small amount of diesel fuel into the heated cylinder as a micro-pilot ignition source after [Douville et al, 1998]. The diesel fuel ignites after a short ignition delay and burns immediately. Then the natural gas is introduced and is ignited by the diesel fuel's hot combustion. To overcome the pressure barrier, Westport developed an intensifier or pump that adds compression to either liquefied or compressed natural gas

before it enters the combustion chamber [Douville et al, 1998]. Westport's pump boosts the natural gas pressure upto approximately 300 bar, which is the level required to force the fuel into a diesel engine cylinder [Douville et al, 1998].

The increase in pressure is especially significant for liquefied natural gas, which is typically stored in a tank at a pressure of just 50 psi [Douville et al, 1998]. Compressed natural gas needs only a small amount of intensification when a tank is at its fully loaded peak pressure of 3600 psi. The need for intensification increases as the tank empties and the internal tank pressure reduces to about 300 psi [Douville et al, 1998].

High Pressure Direct Injection is superior to other technologies for using natural gas in diesel engines, because direct injection and high air compression are essential characteristics of typical compression ignition engines [Douville et al, 1998]. They allow the engines to handle large amounts of fuel and air and deliver large amounts of power and torque at low revolutions per minute, because late-cycle direct injection allows to run the engine unthrottled and with high compression ratio, maintaining the high efficiency of the diesel platform.

1.3 Review of Aerosol Measurement and Sampling

The study of aerosol behaviour has gained importance as a branch of science since it was recognized that the presence of airborne particles is undesirable not only to human health but also to atmospheric visibility and climate. The need to measure aerosols thus became closely linked with the attempts to control and limit them. Aerosol sampling thus became a major issue in applied aerosol science. The science and practice of aerosol sampling has been the subject of a large number of scientific papers and books related to aerosol science [Vincent, 1989]. Interest in aerosol sampling is stimulated by the need to assess the properties of airborne particles. The properties of interest include aerosol mass concentration (which is expressed in milligrams per cubic metre), number concentration, particle size distribution and chemical composition. Aerosols are suspended solid or liquid particles in a gas medium - usually air. They constitute a wide range of particulate clouds encountered terrestrially like naturally occurring snowstorms, sandstorms, mists, clouds, volcanic eruptions etc. and man-made clouds of smoke, fume, coal dust, cement dust, asbestos dust etc. Airborne pollens, viruses and bacteria are also referred to as particulates. Thus aerosols feature widely in nature and human experience [Vincent, 1989].

Particle size is among the most important properties in relation to aerosol sampling. If the particle is spherical, the particle size is represented by its geometric diameter. However, no such single dimension exists for particles that are not spherical. In such cases, it is appropriate to define particle size in terms of one or more equivalent diameters. The equivalent volume diameter is the diameter of a sphere that has the same volume as the particle concerned. Similarly, there are the equivalent projected area and equivalent surface area diameters. The particle aerodynamic diameter is a property of significance related to airborne behaviour [Vincent, 1989].

When aerosols consist of particles of one size, they are referred to as monodisperse systems. When they consist of particles of many different sizes, as in most cases, they are referred to as polydisperse systems.

1.3.1 Deposition methods for particulates

There are six basic mechanisms by which aerosol particles can be deposited onto a surface. They are (1) Interception, (2) Inertial Impaction, (3) Diffusion, (4) Gravitational settling (5) Electrostatic attraction and (6) Thermophoretic precipitation. These six deposition mechanisms form the basis set of mechanisms for all types of aerosol particle deposition, including deposition in a lung, in a sampling tube or in an air cleaner [Hinds, 1999]. Gravitational settling is not suitable for nano-particles due to their extremely low mass. The deposition methods of significance in the case of deposition onto a plane surface are diffusion, inertial impaction and thermophoretic precipitation. Interception mechanism may not be applicable to cases of smooth surfaces of deposition material. Inertial impaction requires the flow upstream of the surface to be in perpendicular or in an angle to the deposition surface. It happens when the particles, because of their inertia, are unable to adjust quickly enough to the abruptly changing streamlines of the flow [Hinds, 1999]. Hence this phenomenon is not applicable to some cases like parallel streamlined flow over and parallel to a plane surface. Diffusion and Thermophoresis depend on concentration gradient and temperature gradient respectively. These two mechanisms are explained briefly in the following sub-sections.

1.3.2 Deposition by diffusion

The pressure of a gas exerted on the walls of a container is due to the mechanism of transfer of momentum by the molecules when they collide with the surface. Aerosol particles, unlike gas molecules, usually adhere to the surface when they collide. Thus a concentration gradient is established in the vicinity. Existence of a concentration gradient can cause a continuous diffusion of aerosol particles to the surface, which leads to a

gradual decay in concentration. If 'x' is the horizontal distance from the surface, the particle concentration at x at any time t, $n(x,t)$, must satisfy Fick's second law of diffusion [Hinds, 1999].

$$Dn/dt = D.\, d^2n/dx^2 \; ; \; n(x,0) = n_0 \text{ for } x > 0 \; ; \; n(0,t) = 0 \text{ for } t > 0$$

The solution for this equation is $n(x,t) = n_0 / (\pi Dt)^{1/2} . \int_0^x \exp(-p^2/4Dt)\, dp$

The rate of particle deposition per unit area of surface can be calculated by evaluating the concentration gradient at the surface and the Fick's first law of diffusion. (As per the Fick's first law, J = -D.(dn/dx), where J is the flux of aerosol particles, D is the particle diffusion coefficient and (dn/dx) is the concentration gradient). Thus, $(dn/dx) = n_0/(\pi Dt)^{1/2}$ for $x = 0$. Hence the rate of deposition of particles onto a unit area of surface at any time t is given by $J = n_0 (D/\pi t)^{1/2}$. The deposition rate can also be expressed in terms of the deposition velocity which is the ratio of deposition flux and the undisturbed concentration. The deposition velocity is the effective velocity with which particles migrate to a surface. Diffusion of aerosol particles to the walls of a tube as they flow through it is a problem of great practical importance.

1.3.3 Deposition by thermophoresis

This refers to the movement of particle resulting from temperature gradient that is established in a gas [Hinds, 1999]. The thermal force and particle motion are always in the direction of decreasing temperature. The magnitude of the thermal force depends on gas and particle properties as well as the temperature gradient. For particles smaller than the mean free path, the thermal force is a result of a greater transfer of momentum on the hot side of the particles relative to those on the cold side. When a cold surface is near a warm gas, the phenomenon of thermophoresis causes particles in the gas to be deposited on the surface. For particles larger than the mean free path, the mechanism is more complicated since a temperature gradient is established in the particle. This gradient affects the temperature gradient in the gas immediately surrounding the particle. The net result is that the particle still receives more momentum from the gas molecules on the hot

side than on the cold side and the net force is in the direction of the colder region [Hinds, 1999]. Thermal precipitators are devices that collect aerosol particles using thermophoresis. The deposition depends on the temperature gradient maintained. A detailed review of thermophoretic sampling is given in the following section.

1.4 Detailed Review of Thermophoretic Samplers

When a temperature gradient is established in a gas, the aerosol particles in that gas experience a force in the direction of decreasing temperature region. This kind of movement of particles due to the thermal force is referred to as thermophoresis [Hinds, 1999]. This effect was first observed in the nineteenth century when it was discovered that a dust-free or dark space surrounded a hot body, suitably illuminated [Friedlander, 1977]. The smoke particles appear to be repelled by the heated object and form a particle-free layer usually less than 1 mm thick, with a well-defined boundary. Measurements of the thickness of this layer showed that it is independent of the particle material and proportional to the square root of the difference in temperature between the object and the gas. It was known from later investigations that the particle-free layer is a manifestation of thermal forces in the temperature gradient near the surface of the heated object [Hinds, 1999].

The thermal force and the particle motion are always in the direction of decreasing temperature. The magnitude of the thermal force depends on gas and particle properties, as well as temperature gradient. When a cold surface is near a warm gas, thermophoresis causes particles in the gas to be deposited onto the surface. This will also occur for a hot gas flowing through a metal tube. For small particles, the thermal force is a result of a greater transfer of momentum from the gas molecules on the hot side of the particles, relative to those on the cold side.

Aside from aerosol sampling, thermophoresis has industrial implications. Thermophoresis contributes to the collection of fine particles in air cleaners having significant internal temperature gradients. It is used to reduce particle deposition onto surfaces in microelectronics industry, by maintaining the product at a higher temperature than that of other surfaces and surrounding air [Hinds, 1999]. Thermophoresis causes problems in certain process applications like petroleum refining where hot gases from fluidized beds pass through heat exchangers and the particles in them deposit on the cold

surface causing scale formation and reduction of the heat transfer coefficient [Friedlander, 1977].

1.4.1 Thermophoretic samplers

The devices that collect aerosol particles using thermophoresis to deposit the particles onto a surface are called thermophoretic samplers or thermal precipitators. These samplers employ a heated element such as wire, ribbon, plate or surface and an ambient temperature surface onto which the particles get deposited. Since the thermophoretic velocities do not decrease with particle size, these devices are excellent collectors of small particles. A conceptual diagram of a thermophoretic precipitator is given as Figure A5 in Appendix A. Thermal precipitators have typically very low volumetric flow rates, which make them particularly suitable for small quantities of particles for observation in optical or electron microscopes [Hinds, 1999]. Heated wire-and-plate type thermal precipitators are among the best samplers, but have the problem of segregation of particles due to the difference in the thermophoretic velocities of small and large particles [Hinds, 1999]. This problem could be minimized using a heated plate instead of the wire. The use of a heated plate also allows to use smaller thermal gradients due to the exposure of the particles to the thermal forces for a longer time.

1.4.2 Factors affecting thermophoretic sampling onto an electron microscope grid

If particles are to be analyzed under electron microscope, they are to be collected onto grids meant for instruments like the Transmission Electron Microscope (TEM). Particles could be collected onto the grids by thermophoretic precipitation. The thermophoretic sampling of particulates are to be done with exhaust pipe or dilution tunnel. The sampling time should be favorably below 30 minutes at any location. These factors together with the dimensions of standard TEM grid pose important design constraints. The various factors affecting the sampling process are:

1. *Location of sampling and sampling time*: The sampling could be done at the exhaust pipe or at the dilution tunnel. The positioning of sampling in the case of hot exhaust is important since the particles coming out of the cylinder are highly unstable and susceptible to physical/chemical changes in accordance with the surrounding conditions.
2. *Temperature of exhaust gas*: As stated earlier, at temperatures above 500° C, the individual particles are clusters of many spherules of carbon and at below this limit, the particles become coated with various compounds.
3. *Positioning of the TEM grid in the flow*: The grid can be positioned at any angle compared to the flow, if thermophoretic mode is employed as in usual cases. Positioning the grid horizontally enables gravity to help deposition of larger particles. The flow could be made to have a 90° impact on the grid or just allowed to flow over the grid, parallel to its surface.
4. *The temperature difference maintained*: The temperature difference cannot be too high since higher temperatures can change the composition of highly unstable particles. Even at less temperature differences, the effective temperature gradient at the immediate vicinity of the grid will be much higher and sufficient for trapping enough number of particles.
5. *The flow rate over/past the grid*: The flow rate of exhaust gas is important since it determines the number of particles passing through per unit time. Theoretical calculations of particle deposition are usually made using the flow rate and the emission statistics of engines as the basic parameters for finding the number of particles available for a particular period of time.
6. *Precise control of temperatures and times during sampling*: During sampling at various conditions, it is quite likely that the temperature conditions at the site of deposition vary frequently. This can make inconsistencies between the theory and actual deposition. The same effect is there for inaccurate sampling times. An effective temperature control circuit with a timer can solve the problem.
7. *Control of fluid flow over the grid*: The areas adjoining the sampling site should be designed in such a way that there is no hindrance to the flow of exhaust gas outwards

from the sampler. There should not be any back-flow of gas either. Problems in the smooth flow of gas can reduce the number of particles trapped.

8. *Material used for the grid and grid holder*: Grids are available which are made of copper, nickel and molybdenum. Nickel grids can be magnetically held in the holder so that maximum surface area is exposed. The grids are coated with a layer of pure carbon and the thickness of this carbon film is important for observation of the particles. Usually the thickness of carbon film is about 25 nm. The grids with a thickness of approximately 0.1 mm may deform slightly in the thermophoretic sampling method. This should be taken into account while deciding on the thickness of the gap between the grid and the heated surface. High melting point, sufficient hardness, resistance to wear and tear and non-corrosiveness are the most important desirable features of the material for the grid holder. Stainless steel and brass are suitable materials for the grid holder. The part holding the metal grid should transfer the heat from the grid and thus dissipate heat energy accumulated in the grid material. This helps to keep the grid temperature as low as possible to maintain the temperature gradient over the grid in thermophoretic sampling. Brass, due to its relatively high thermal conductivity, is better than stainless steel for this purpose.
9. *Mode of starting/stopping the exposure*: The exposure of the grid to the exhaust flow can be accomplished mainly by two ways - by introducing the grid suddenly to the flow field and removing it in a similar way or by controlling the flow with an ON/OFF valve. The latter is more feasible since it is consistent with the theoretical exposure time. Moreover, it is practically easier to have an ON/OFF valve.

1.5 Objectives and Scope of the thesis

The importance of having knowledge about exhaust particulate material, curiosity and interest in getting sufficient data on particulate emission by HPDI engines and the challenges posed by thermophoretic aerosol sampling of the particles from engines - all of these provided sufficient motivation for a research study on the characteristics of emitted particles from the predominantly natural gas-fueled HPDI engines. Perhaps the unavailability of data such as particle size range, shapes and spherule dimensions of HPDI particles contributed the most.

The main objectives of this research study are:

- To design and build a thermophoretic particulate sampler for collecting exhaust particulates from engines onto the Transmission Electron Microscope (TEM) grids
- To collect particulate samples from HPDI engines at different load conditions, speed conditions and different pilot fuel quantities
- To analyze the particles under Transmission Electron Microscope to determine parameters like particle size range, particle shapes, spherule dimensions, abundance of spherules and presence of strange particles
- To make a good database on the characteristics of particulates emitted by HPDI engines, where natural gas accounts for a lion's share of the fuel consumed

The study relies on direct measurement of parameters concerning the particles using the TEM, the TEM being the most versatile instrument among the electron microscopes. (The TEM can provide magnifications of up to 600,000). The study focuses on taking those data which could be collected from the direct observation of particles.

References

Automotive Handbook (1993), 3rd Edition, Robert Bosch GmbH, Stuttgart.

Douville, B., Ouellette, P., Touchette, A. and Ursu, B. (1998), *Performance and Emissions of a Two-Stroke Engine Fueled Using High-Pressure Direct Injection of Natural Gas*, SAE Paper 981160.

Friedlander, S. K. (1977), *Smoke, Dust and Haze*, Wiley Interscience, New York.

Heywood, J. B. (1988), *Internal Combustion Engine Fundamentals*, McGraw Hill, New York.

Hinds, W. C. (1999), *Aerosol Technology*, John Wiley & Sons Inc., New York.

Schafer, F. and van Basshuysen, R. (1995), *Reduced Emissions and Fuel Consumption in Automobile Engines*, Springer-Verlag, Wien, New York.

Vincent, J. H. (1989), *Aerosol sampling science and Practice*, John Wiley and Sons, New York.

Walsh, M.and Shah, J. J. (1997), *Clean Fuels for Asia*, World Bank Technical Paper No. 377, The World Bank, Washington, D.C.

Chapter 2

Design and Application of a Thermophoretic Sampler to study Particulate Emission by H.P.D.I. Engines

2.1 Introduction

As stated earlier, particulates are suspended solid/liquid particles in air, which are larger than single molecules. The larger particles are produced from natural sources and smaller particles from man-made sources like industrial processes and automotive fuel combustion. The smaller particles are extremely hazardous to health and their typical lifetime is a few days to a few weeks. The fine particles are those which are less than 2.5 microns in size and coarse particles are those which are greater than this limit. One of the contributors of atmospheric particulates is the diesel engine. Diesel emission standards are becoming more and more stringent and it has become increasingly advantageous to switch over to alternative fuels in compression ignition (CI) engines.

Natural gas (NG) is a viable option in CI engines. It has several advantages like low emissions and availability. But there are certain challenges to be faced before using it in traditional CI engines. These are mainly due to the inability of natural gas to burn in the conditions prevailing in CI engines and also the high pressure needed to push the fuel into the cylinder in case of a dual fuel engine with diesel. The High Pressure Direct Injection (HPDI) technology of Westport Innovations Inc., Canada, is a proven technology for using NG in CI engines with minimal engine modifications. A pilot quantity of diesel fuel is used to help in the ignition of NG in each power cycle. Data on the particulate emission from HPDI engines is required inorder to understand particulate emissions from this technology. Data like particle number concentration, particle size range, spherule dimensions, spherule size range and chemical composition of the particles need to be collected. One way to determine these parameters is to directly observe the particles using a Transmission Electron Microscope (TEM). The particles need to be sampled on to TEM grids, which are 3.05 mm in diameter and 25 microns thick.

There are several ways to collect aerosol (particulate material), but not all of them are suitable for use with engine exhaust. Thermophoretic sampling is a reliable method to sample engine particulates. It depends on the deposition of particles due to a temperature

gradient. Some studies have reported that this method, if properly employed, could be 100 percent efficient [Hinds, 1999]. The various methods of particle deposition on to TEM grids and the previous works on thermophoretic sampling are to be thoroughly analyzed before designing a thermophoretic sampler. The biggest challenge is offered by the TEM grids themselves due to their dimensions.

2.2 Review of the existing sampling techniques

The objective of most particulate emission measurement techniques is to determine the amount of particulate being emitted to the atmosphere. Techniques for particulate measurement and characterization range from simple smoke meter opacity readings to analyses using dilution tunnels [Heywood, 1988]. Most techniques require lengthy sample-collection periods because the emission rates of individual species is usually low. The physical conditions under which particulate measurements are made are critical because the emitted species are unstable and may be altered through loss to surfaces, change in size distribution (through collisions) and chemical interactions among other species in the exhaust at any time during the measurement process (including sampling, storage or examination). In the standard particulate engine exhaust emission measurement procedure, dilution tunnels are used to simulate the physical and chemical processes the particulate emissions undergo in the atmosphere. In the dilution tunnel, the raw exhaust gases are diluted with ambient air to a temperature of about 52°C and a sample stream from the diluted exhaust is filtered to remove the particulate material.

2.2.1 Typical thermophoretic sampling methods reported in literature

2.2.1a *Method reported by Maynard* [Maynard, 1995]

A thermophoretic precipitator specifically for collecting ultrafine aerosol samples onto electron microscope support grids was reported. The precipitator was designed to deposit particles of diameter less than 100nm discretely onto support grids, with uniform deposition velocity across the size range. The method used was of particle deposition between two parallel plates between which a uniform temperature gradient of 10^6 K/m was sustained by mounting a heating element flush with the surface opposite the grid. To reduce heat losses in the precipitator, the upper and lower plates were separated by strips of Kapton. Aerosol was drawn through the precipitator by a battery powered personal sampling pump. A diagram showing the major parts of the sampler is given as Figure 2.1 at the end of this chapter.

Uniform deposition could not be achieved. A temperature difference of 100° C was maintained in a plate separation of 0.1 mm. The minimum flow rate for total deposition was 0.48 lit/min.

Critical analysis of the sampler

Some of the notable drawbacks associated with the sampler were:

1. The flow channel for the aerosol particles inside the sampler was too wide (80 mm) compared to the diameter of grids (3 mm) and this might have caused escape of a fairly large number of particles without passing through the sampling zone
2. The flow channel depth was just 0.15 mm, which might have caused deposition of particles to the inner surfaces other than the grid, due to adhesion
3. The grid was held on the top surface in the flow channel, which could have reduced the chances of deposition due to gravitational forces
4. The design was fairly complex due to the large number of individual components involved in it
5. The device was specifically designed for using grids made of ferrous material

2.2.1b ***Method reported by Rogak et al.*** [Rogak et al., 1993]

A thermophoretic sampler consisting of an aerosol preheater, a nozzle to direct the hot aerosol over the microscope grid and a means for keeping the grid cool is reported. The device was used to study the structure and mobility of TiO_2 and Si agglomerates. The heating tape used for preheating incoming aerosol was designed to operate at a temperature of 300° C. The jet of sample aerosol coming out of the nozzle (nozzle diameter was 1 mm) was made to bombard the grid perpendicular to its surface. The flow rate used was in the range 0.2 - 1.5 lit/min. There was provision for cooling the grid by means of a long copper rod immersed in a water bath at about 20 °C. A diagram showing the basic details of the sampler is given as Figure 2.2 at the end of this chapter.

Critical analysis of the sampler

Some of the notable drawbacks associated with the sampler were:

1. The grid was not completely exposed to the incoming aerosol flow, thus reducing the number of particles deposited and the effective area of deposition
2. The fact that the grid was held in a recess indicates that it reduced the effective temperature gradient and thereby the deposition rate
3. The cooling system incorporated with the sampler (Copper rod immersed in a water bath) is practically difficult to implement in many other cases
4. The design was such that the replacement of grids in between experiments was rather difficult and time consuming

Thus the notable thermophoretic samplers mentioned in literature had some problems for sampling in the engine conditions.

2.2.2 PM deposition onto TEM grids - earlier works by present author

Some preliminary engine-particulate sampling tests were conducted at UBC Department of Mechanical Engineering during January-April, 2000. The engine used for conducting the tests was the Detroit Diesel DDC 6V92 engine available at the Engines Laboratory of UBC Department of Mechanical Engineering. The engine is a six-cylinder, 2-stroke diesel engine with a power output of 300 HP. The engine was water cooled and turbo-charged. It could be operated with diesel or diesel/natural gas using HPDI fuel injector. During the course of the test period, the engine was set to run on pure diesel mode. There was a mini-dilution tunnel system fitted to the engine, to sample particulate emissions.

2.2.2a The grid holder

The grid holder was designed to fit into the mini-dilution tunnel. It was made to expose the grid into the stream of the mixture of exhaust gas and air. Basically, it was a

sampler based on diffusion mode for particle deposition due to the local concentration gradient over the grid. A diagram of the grid holder is given as Figure A7 in Appendix A. The diameter of the grid is 3.05 mm and its thickness is about 25 microns. The grid material is either copper, molybdenum or nickel. The grid consists of a lot of square-shaped holes (about 200), the side length of each of them being 0.1 mm. A simple diagram of a TEM grid is given as Figure 2.3 at the end of this chapter. Since the particulate material is usually in the sub-micron size range, they can easily pass through these holes. Hence, one side of the grid is coated with a thin film of carbon, the thickness of which is less than the size of particulates. The purpose of the film is to trap the particulate material. The material used for building the grid holder was stainless steel. Mild steel was also used (for the thin metal plate over the grid hole). The grid holder is a metal rod (diameter being a quarter of an inch) having a length of 6 inches. The provision for holding the grid is provided towards one end of the holder. A thin metal plate is provided over the grid hole, which is screwed to the main holder. The metal plate has a hole having a diameter of about 2 mm at the centre to give exposure for the grid. The surface of the cover plate near the vicinity of the grid hole is recessed, in order to increase the rate of diffusion of particles into the grid, which is to be placed in the grid hole beneath the plate.

2.2.2b Sampling at different conditions

Sampling was done at the dilution tunnel as well as at the hot exhaust. Grids were exposed to different time intervals at both locations. The exposure times at the hot exhaust were 1 second, 5 seconds, 20 seconds and 60 seconds. The exposure times at the dilution tunnel were 2.5 minutes, 5 minutes, 10 minutes and 20 minutes. In the case of sampling at hot exhaust, a provision was fitted on the exhaust pipe to convey burned gases through a small hole, in order to expose the grid. Since the grid holder was designed exclusively for sampling at the dilution tunnel, it was not particularly suitable for sampling at the hot exhaust and eventually, it was to be held in hand for exposure to the hot exhaust.

2.2.2c Analyses of samples

The analyses of the samples were carried out with the help of Transmission Electron Microscope (TEM). As mentioned in chapter 1, the TEM is the most versatile instrument among microscopes. It could be used to see objects having sizes smaller than 0.05 micron. The TEM can enlarge images to 600,000 times that of the original size. It is suitable for analyzing diesel particulates. In the TEM, electrons are generated by thermionic emission from a heated tungsten filament and are focused by magnetic lenses. The focal length of magnetic lens could be adjusted by controlling the current through them. The interior of the TEM, including the sampling area, must be under a high vacuum (less than 0.01 Pa), to prevent the scattering of electron beam by air molecules. This is accomplished by a combination of mechanical and oil diffusion vacuum pumps. Particles bombarded by the electron beam absorb and scatter electrons to produce a two-dimensional silhouette image similar to that produced in optical microscopy. The magnified image is viewed by projecting the electron image on to a fluorescent screen or a photographic plate. Each sample was observed for hours under the microscope. Attempts were made to get an approximate number concentration of particles, by counting the number in some square holes in the grid.

2.2.2d Practical considerations

Copper grids were used in the first set of tests, but the thickness of carbon film in each of them was large enough to hinder detection of particulates. However, the carbon films over nickel grids were found to be thin enough to observe the particles. Hence nickel grids were used for all the subsequent tests conducted. The recess at the central portion of the mild steel cover plate over the grid hole was made after the first test, to facilitate more diffusion of particles into the grid. This could probably be another reason for the no-deposition outcome for the first test, apart from carbon film thickness over copper grids and inadequate exposure times (2.5 minutes and 5 minutes at the dilution tunnel). Since the initial test at the dilution tunnel gave no results, exposure times for subsequent tests were enhanced. This paved the way for getting good results. It was decided to take samples at the hot exhaust also apart from the mini-dilution tunnel, since

the initial results from dilution tunnel sampling were not satisfactory. But since the grid holder was designed for sampling at the dilution tunnel, it was to be held by hand before the hot gas for sampling at the hot exhaust. For all the tests, the dilution ratio used in the mini-dilution tunnel was 4. As mentioned earlier, a mini-dilution tunnel is used to simulate the physical and chemical processes the particulate emissions undergo in the atmosphere. A diagram of a mini-dilution tunnel system is given as Figure A6 in Appendix A

The sampler could produce some results, but further improvements in the design by adopting reproducible temperatures and times were required to make the sampling more reliable.

2.3 Design of a Thermophoretic Sampling System

As mentioned in earlier sections, the previously developed sampler and the notable thermophoretic samplers reported in literature were not perfectly suitable for the present application. Thus it was required to design a new particulate sampler specifically suitable for sampling exhaust particulate material from engines. An improved sampler was designed by careful consideration of the deposition process. The critical parameters of importance in the design process include sampling location, sampling period, temperature range, flow rate and reproducible temperatures. Moreover the design was to be simple and user-friendly too. These factors were considered in developing a suitable universal design for sampling exhaust particulates from engines. The various factors affecting thermophoretic sampling onto TEM grids, observation of particles under the microscope and critical parameters to be considered for the design were taken into account for the novel design.

2.3.1 Design Objectives

The major objectives of the design process include:

1. To design a particulate sampler, for collecting particulate material from the hot exhaust gas of engines onto TEM grids
2. To use standard components in the sampler inorder to make it useful for applications in different engine systems, i.e., to make it ready for sampling at different engine locations with little/no extra standard connections
3. To make the device user-friendly
4. To avoid unnecessary complexity
5. To make the design as efficient as possible in collecting the particles
6. To have provision to use grid made of any material
7. To provide maximum exposure to the grid in the stream of incoming gas
8. To have reproducible temperature for the thermophoretic sampling
9. To have an economically and technically viable design
10. To have minimum number of moving parts in the sampler system

2.3.2 Description of the design

The basic diagrams of the new design and block diagram of the test setup are given as Figures A1, A2, A3 and A4 in Appendix A. A simple diagram showing the structural details of the sampler is given as Figure 2.5 at the end of this chapter. The various important parts of the sampler are the steel tube, nozzle tube, upper and lower plates, magnetic and non-magnetic grid holder and the magnet assembly for the magnetic holder. Basically, the sampler conveys the hot exhaust gas from the exhaust pipe through a preheated and temperature-monitored stainless steel tube before making a 90° impact on the grid which is firmly held by a magnetic or non-magnetic holder. The stainless steel tube is having a length of 7 inches (178 mm) and an outer diameter of 0.25 inch (6.35 mm). The inner diameter of this tube is 0.1875 inch (4.76 mm). The tube conveys hot exhaust from a packless (high-temperature) valve to the nozzle tube. The packless valve is an ON/OFF valve for the incoming gas. It is selected to withstand the high temperature of the incoming gas and also the heat provided to the tube in the downstream. The nozzle tube is a small but wide tube which holds the steel tube perpendicular to it. It is made up of stainless steel and has the desired nozzle inside with the required tip inner diameter which is 1 mm (0.04 inch). The nozzle tube is welded to the tube upstream. It is also welded to the upper plate which is made of stainless steel. The upper plate is for providing an air-tight roof for the cavity inside. It also houses the outlet tube of the exhaust gas from the sampler and is welded to it. The upper plate is welded to the lower plate which is also made up of stainless steel. The lower plate forms the major part in the body of the sampler. It has screw holes to accommodate the grid holders. The grid holders are made of brass inorder to facilitate easy transfer of heat from the grid. All other important parts are made of stainless steel for ensuring strength and durability. The grid holders are fitted in such a way that the gap between the nozzle tip and the grid is only 1 mm (0.04 inch). A diagram showing the streamlines of the gas flow over the grid is given as Figure 2.4 at the end of this chapter. But in the case of non-magnetic grid holder, the effective gap is slightly larger due to the recess above the grid in the grid holder. The non-magnetic holder consists of two components. The upper component is in contact with the

lower plate (made of stainless steel) and the contact area is kept at the minimum possible. It houses an O-ring to prevent possible leakage of gas from the cavity inside the sampler. The hole on top has sharp edges and a diameter of 0.1 inch (2.5 mm) which is less than the grid diameter. The depth of the hole is 0.04 inch (1 mm) which forms a recess over the grid once it is assembled. The lower component has the recess on top to place the grid, so that the grid will be firmly held once the components are assembled with the lower plate. The recess has a depth of 0.1 mm and a diameter of 3.06 mm which are the approximate dimensions for standard TEM grids. The lower component also houses an O-ring to prevent gas leakage. There is a hole from the bottom which reaches just below the grid recess. The hole is approximately 0.1 inch (2.5 mm) in diameter and is meant for conveying cold air with a pump to dissipate heat from the neighborhood of the grid. The magnetic holder is a single component housing with provision for placing the magnet assembly. It also houses O-ring and has drilled-conveyors for cold air passage. The magnet assembly consists of two blocks of a magnetic material (mild steel) with a brass piece (non-magnetic) in between. There is provision for keeping the magnet inside. A recess is made on top to place the grid. Only nickel grids could be used in this holder since nickel is ferromagnetic. The grid, once placed, acts as a bridge between the mild steel blocks and is located in the magnetic flux lines. Hence it is firmly held in the holder which facilitates maximum exposure to the impinging stream of exhaust gas. The exhaust gas is conveyed in the downstream through a flow control valve and a flow-meter from the sampler using metal (copper) tube. The 7-inch (178 mm) tube in the upstream of sampling is wound with a flexible heater coil which is connected to a temperature controller which gets input from a thermocouple wire. The bead of the thermocouple is placed in the tube at a location near the sampling site. It is designed to have a control on the reproducible temperature provided to the exhaust gas.

2.4 Predicted performance of the sampler

An understanding of the mechanical behaviour of the sub-micron sized particles is required before predicting the performance of the sampler. The mechanics of particulates are briefly explained prior to mentioning the performance of the sampler.

2.4.1 Mechanics of particulates

The important ways of collecting particles on to a TEM grid are deposition by Diffusion, Thermophoresis, Gravity and Electrostatic precipitation. Design of a sampling system requires quantitative estimates of their effects. For typical diesel particulates, the prominent ways of deposition are by Diffusion and Thermophoresis as shown in Appendix B. In reality, deposition is affected by all these factors simultaneously.

The dimensionless parameters of importance in aerosol mechanics are the Reynolds number (Re), Knudsen number (Kn) and Drag coefficient (C_D). {$Re = \rho U d/\mu$; $Kn = 2\lambda/d$; $C_D = 2F/A\rho U^2$ where λ = Gas mean free path; μ = viscosity; ρ = density; F = Drag force; d = Diameter of the particle}. For small Knudsen number, the drag coefficient is $C_D = \frac{24}{Re}$; for $Re < 0.1$. For $0.1 < Re < 2$, $C_D = \frac{24}{Re}\left(1 + \frac{3}{16}Re + \frac{9}{160}Re^2 \ln 2Re\right)$. For particles comparable to the mean free path of the gas, the Cunningham slip correction factor (C_C) is to be considered.

$$C_C = 1 + Kn\left(1.257 + 0.4\exp\left\{\frac{-1.1}{Kn}\right\}\right)$$

2.4.1a Adhesion of particles

Aerosol particles generally attach firmly to any surface of contact unlike other particles/gas molecules [Hinds, 1999]. When aerosol particles contact one another, they adhere to form agglomerates. Prominent particle-collection methods including filtration method depend on the adhesion of particles to surfaces. Adhesive forces are the most

prominent forces on micrometer-sized particles. Particle adhesion is not completely understood yet [Hinds, 1999]. The major adhesive forces include van der Waals force, electrostatic force and the force arising from the surface tension of adsorbed liquid film [Hinds, 1999]. Adhesive forces are generally affected by material, shape, surface roughness, size of the particle; material, roughness and contamination of the surface; relative humidity; temperature; duration of contact; initial contact velocity. London-van der Waals forces are long range forces (unlike chemical bond forces) that exist between molecules [Hinds, 1999]. Chemical bonds are not important for the adhesion of aerosols under ambient condition [Hinds, 1999]. van der Waals forces arise because random movement of electrons in material creates momentary areas of concentrated charge called dipoles. These dipoles induce complementary dipoles in neighbouring material at any instant. These in turn produce attractive forces [Hinds, 1999]. The influence of van der Waals forces extends only a few molecular diameters away from a surface [Hinds, 1999]. The forces decrease rapidly with separation distance between surfaces.

2.4.1b Electrostatic force

Most particles 0.1 μm or larger carry some small net charge 'q', which induces an equal and opposite charge in the surface. This gives an attractive electrostatic force of $F_E = K_e q^2/x_q^2$, where K_E - constant of proportionality; x_q - separation distance of opposite charges. Equilibrium charge carried by particles larger than 0.1 μm is approximately proportional to $\sqrt{d}$, so that the electrostatic adhesion force is also proportional to the first power of particle diameter.

2.4.1c Surface tension force

Surface tension force is an attractive force between a particle and a surface, created by the surface tension of the liquid drawn into the capillary space at the point of contact. For relative humidities greater than 90% and ideal, smooth surfaces, $F_S = 2\pi\gamma d$,

where γ is the surface tension of the liquid. Except for highly charged particles, vdW forces and surface tension forces are greater than electrostatic forces.

2.4.1d Particle bounce

Kinetic energy gets dissipated when particle strikes a surface. If the rebound energy exceeds the adhesion energy, the particle may bounce away from the surface. The factors favouring bounce are hardness of particle material, large size of the particle and greater velocity. Surface roughness also plays a significant role. Surface coating with oil or grease increases adhesion energy, the deformation and the dissipation energy, thus reducing the problem of bounce.

2.4.1e Particle motion

Most aerosol motion occurs at low Reynolds numbers. The terms like Stokes's Law, settling velocity, mean free path, particle mobility, aerodynamic diameter are important in particle motion study. *Stokes's Law* [Hinds, 1999] states that $F_D = 3\pi\eta Vd$, where F_D is the total resisting force on a spherical particle moving with a velocity, V, η is the viscosity. *Settling velocity (in still air)* [Hinds, 1999] states the condition, $3\pi\eta Vd = (\rho_P - \rho_g)\ \pi d^3 g/6$. ρ_g is included to account for the buoyancy effect, but is usually negligible compared to ρ_P. For a water droplet in air, $\rho_P/\rho_g = 800$ and the terminal settling velocity, $V = \rho_P d^2 g/18\eta$, for $d > 1$ μm and $Re < 1$, where ρ_P is the density of the particle, ρ_g is the density of gas, g is the acceleration due to gravity. *Particle mobility* (B) is defined as $B = V/F_D = 1/3\pi\eta d$, for $d > 1$ μm. Terminal settling velocity of an aerosol particle = F_G B, where F_G is the force of gravity. For particles with $d < 1$ μm, Cunningham slip correction factor, C_C, is to be considered.

$F_D = 3\pi\eta Vd/C_C$, where $C_C = 1 + \frac{2.25\lambda}{d}$, where λ is the mean free path

For non-spherical particles, $F_D = 3\pi\eta Vd_e\chi$, where χ is the dynamic shape factor, d_e is the equivalent volume diameter. We have $V = \rho_P\ d_e^2 g/18\eta\chi$. Considering aerodynamic

diameter, d_a, $V = \rho_o d_a^2 g/18\eta$, where ρ_o is the standard particle density. For $Re > 1$, $V = (4\rho_P d_P g/3C_D \rho_g)^{1/2}$ where C_D = drag coefficient.

2.4.2 Theoretical calculations for deposition through various modes

The major assumptions for the theoretical calculations for the design are -

- The incoming gas jet is at a uniform temperature as adjusted by the temperature control unit, just before it impinges on the grid
- There is no loss of particles anywhere in the sampler unit upstream of the grid site
- Even though the exhaust particles have weird shapes, they are assumed to be perfect spheres with specific diameters (equivalent diameters of spheres of carbon with the same volume)
- Since sampling is done at a location not too far from the cylinder outlet, lack of sufficient time to oxidize/react in the new conditions preserves the homogeneity of the particles and as a result, the particles are composed of pure carbon only
- Density of elemental carbon is 2300 kg/m^3
- The density of exhaust gas is the same as that of atmospheric air
- The viscosity of exhaust gas and air are equal
- The thermal conductivity of exhaust gas is same as that of air

Even though the sampler is primarily thermophoretic in nature, all the important modes of particle deposition, viz. Diffusion and Inertial impaction also play their role in the overall process. The detailed version of design calculations are mentioned in Appendix B. In the calculations, assumptions are made on the emission of particles and also on their average size. Soot emission from a typical diesel engine is assumed to be 20 mg/m^3. Thus the number of particles per cubic metre of exhaust gas is calculated as 2.076×10^{12}, assuming the average size as 200 nm.

Deposition through the Thermophoretic mode

The temperature maintained for the exhaust gas is supposed to be 400°C and the temperature of the grid is assumed to be 21°C. The thermophoretic velocity, V_{th}, could be calculated as $V_{th} = (-3.\eta.C_c.H.\nabla T)/(2.\rho_g.T)$ [Hinds, 1999], where η = viscosity in Ns/m^2, ∇T is the temperature gradient in K/m (details of calculation given in section B.5 in Appendix B), ρ_g is the density of gas in kg/m^3 and T is the temperature of the particle in K. C_c is a constant which is $\{1 + (2.52\lambda/d)\}$, where λ is the mean free path of particles in meter and d is the diameter of each particle in meter. H is a constant which is $(1/(1 + 6\lambda/d)).((k_a/k_p + 4.4\lambda/d)/(1 + 2k_ak_p + 8.8\lambda/d))$, where k_a is the thermal conductivity of gas in W/m-K and k_p is the thermal conductivity of the particle in W/m-K. The details about computing the heat transfer coefficient and the temperature gradient are given in Appendix B. The temperature gradient in this case is 9.9×10^6. Hence V_{th} could be calculated as 0.077 m/s, considering the typical particle diameter as 200nm. Thus the number of particles deposited per square hole on the grid per minute is 95640, considering uniform deposition of particles over the grid (the grid has a fine mesh on it which has a lot of square holes with each hole's dimension being 0.1 mm). Thus it is assured that sufficient number of particles will be deposited on the grid through this method. Deposition efficiency of a sampler indicates the relative number of particles deposited onto the grid to the total number of particles that passed through the sampling zone. A table showing the deposition efficiency for different particle sizes is given in Appendix B.

Deposition through the Diffusion mode

As mentioned earlier, deposition of particles takes place due to the concentration gradient between the surface and the flow field adjoining it. The diffusion coefficient, D is $(kTC_c)/(3\pi\eta d)$ [Hinds, 1999], where k is the Boltzmann constant. Thus D could be calculated as 4.89×10^{-10} m^2/s. Considering that the situation is equivalent to an infinite volume of stagnant aerosol maintained at a concentration of n_0 outside the gradient

region, number of particles deposited during 1 minute is given by the expression, $2.n_0.(Dt/\pi)^{1/2}$, where t is the time in seconds, which is 60 and n_0 is the concentration of particles. Thus the deposition rate could be computed as 401247614 /m^2 per minute. This shows that the number of particles deposited per square hole during one minute is 4. This mode is very weak compared to the thermophoretic method of deposition.

Deposition through the Inertial Impaction mode

Relatively larger particles are affected by this method. Hence the exact particle size distribution of the test-engine is required for accurate calculations of particle deposited under various conditions. However, a simple calculation to find the impaction efficiency is given in Appendix B. We have Impaction efficiency, $E_I = \Delta/h$, where Δ is the radial displacement of the particle from its original streamline and 'h' is the radius of the nozzle tip. While taking the impaction efficiency into consideration, 882 particles will be collected per square hole in one minute. This shows that this method is not as prominent as the thermophoretic mode.

Other design calculations for velocity at nozzle tip, approximate minimum length required for the heating pipe, approximate power requirement and heat transfer to and from the grid are described in Appendix B.

2.4.3 Summary of F.E.M. results

Finite Element thermal analysis was performed for the sampler model using ANSYS 5.6. The results of the analyses at various conditions are given as plots in Appendix C. The main idea in the FEM analysis was to get the temperature distribution in the sampler body at various intervals of time. The analyses were done for 15 minutes, 30 minutes and 60 minutes. The element type for the analyses was Solid 75 (4-noded, 2D axisymmetric). Pure conduction cases were tried, since the heat flux due to the incoming

gas lasts for only 10 seconds. The average heat flux from the gas generally depends on the temperature difference between the inner surfaces of the model and the hot gas.

The results are as given as figures in Appendix C. The temperature rise in the grid after one hour of continuous operation was computed as 149 °C. The average values of temperature in the nodes in the vicinity of the grid were computed and used as boundary condition for the submodel. The submodel was considered for the region in the vicinity of the grid for closer analysis of the temperature rise in the grid. Generally, the temperature was concentrated in the tube region and decreased slowly towards the bottom surface in all time steps. As could be seen from the results, the convective heat flux was a minor heat load compared to conduction heat transfer. No significant temperature rise was noted for 10-second heat addition to the inner walls of the sampler from the hot gas. The Finite Element model predicted the temperature in the tube region to be above 673 K, even though it was assumed that the temperature provided by the heating wire as well as the gas is 673 K.

Analyses were performed for the pure conduction cases for time intervals of 5 minutes, 10 minutes and 15 minutes respectively inorder to compare the results with that of experimental results obtained. The results were comparable as given in Appendix C. This was mainly done to verify whether the finite element model was giving reliable results.

In the actual case, the heating wire of the sampler was switched off immediately after a period of sampling and switched on about 4-5 minutes prior to the sampling period. The sampling time used was 10 seconds as mentioned in section 2.5.1. Hence it could be safely assumed that the maximum period of continuous operation of heating wire was less than 15 minutes. From the finite element results, the temperature rise in the grid region during this period was about 30 °C. This could reduce the temperature gradient from the design value of 9.9×10^6 K/m to 9.1×10^6 K/m, thereby reducing the thermophoretic velocity (expression given in Appendix B) by 8% from its design value.

This would reduce the deposition rate on the grid. The FEM results also show that the nozzle can be up to 100 °C cooler than the heater set point, 15 minutes after turning the heater on. This indicates that significant cooling of gas is possible in the nozzle.

The major sources of error which caused the results of the FE analyses to vary slightly from the experimental measurements and theoretical predictions are :

1. Neglecting the heat losses from the outer surfaces of the sampler body. In practice, there are vibrations, which increase the heat loss from the surface.
2. Neglecting radiation effects.
3. Errors in having constant value for the convective heat flux from the hot gas to the inner surfaces. (The heat flux in reality is a time-dependent function).
4. There could be variations in the temperature provided by the heating wire to the outer surface of the tube in practice.
5. A constant initial temperature condition at a higher value was given as boundary condition for the sub-model, whereas in actual case, the initial temperature starts from 294 K and rises up to the value which was the boundary condition of the submodel.

The major conclusions of the finite element thermal analysis are -

1. The FE model gave results which are consistent with the experimental data.
2. The temperature rise in the grid was 149 K above the initial temperature of 294 K after a continuous application of heat for 60 minutes.
3. The high temperature was generally concentrated in the tube region.
4. As can be seen from the results, convection was much weaker than conduction and convection acts only for 10 seconds.
5. The sources of error as mentioned earlier caused slight variations in the results when compared to the experimental data.
6. The submodel computation was consistent with the master model.

2.5 Application of the sampling system

The sampler system was used to collect samples from different HPDI engines at different operating conditions. The collected samples were then subjected to detailed analysis using Transmission Electron Microscope (TEM).

2.5.1 Engines used for the tests

Two engines were used for the tests - Engine A (Cummins QSK60) and Engine B (Cummins ISX 400). The Engine A, used for the tests was a natural gas-powered HPDI engine. It was a 6-cylinder engine with a rated speed of 1800 RPM and a power output of 559 kW (at 1800 RPM). The details of the engine are given in the table below.

Engine and fuel data	Values
Engine Displacement	18.9 litres
Number of cylinders	6
Number of strokes per cycle	4
Cylinder Bore	0.1588 m
Piston Stroke	0.1588 m
Cylinder Clearance Volume	0.2225 litre

Engine B was smaller compared to Engine A. This was also a natural gas-powered HPDI engine. It was a 6-cylinder engine which operated at 732 RPM and at a brake torque of about 400 N-m during the experiments. The details of the engine are given below.

Engine and fuel data	Values
Engine Displacement	14.95 litres
Number of cylinders	6
Number of strokes per cycle	4
Cylinder Bore	0.1370 m
Piston Stroke	0.1690 m
Cylinder Clearance Volume	0.1361 litre

Outlet connections in the hot exhaust pipes were used for mounting the sampler. The components of the sampling system were placed near the sampler and every measure was taken to ensure the smooth flow of hot exhaust through the sampler. The block diagram of the sampling system is given as Figure A4 in Appendix A.

2.5.2 Observation Procedures

Observation under the Transmission Electron Microscope (HITACHI H-800 Electron Microscope) was intended to get the following details:

1. Number concentration of particles per square hole in the grid
2. Size range of particles
3. Shapes of particles
4. Number of spherules in particles
5. Size range of spherules
6. Shapes of spherules
7. Interesting features, if any

As mentioned earlier in the thesis, the grids made of nickel were used and they have a thickness of about 25 microns. A thin layer made of carbon, having a thickness of about 25 nm was there on one side of each of the grids. Each grid had about 200 square holes, the sides of which measured 0.1 mm. No particle would be seen normally below magnifications of about 1000. The square holes would be bright and the borders of the holes would be dark in appearance. Usually, the magnification was set at a value of 3000 to get a rough idea of the abundance of big particles. At this value of magnification, a few particles could be seen as spots or tiny dark regions. The magnification was then increased to 5000 and the area of observation was traversed from one corner of a square hole to another through the edge of the hole. Then traverses parallel to this route were done in all cases, to cover the whole area of the hole. The number of particles in various large size ranges could be estimated like this. The magnification is then increased to 10,000 or above and the same process of visual counting of smaller particles were done

from one end of the hole to the other. The process was then repeated for 3 or 4 more holes in each case and the average values were taken. The holes were chosen from different regions in the grid to account for the disparity in the distribution of particles on the grid which was observed in all the cases. There was no order for the distribution of particles on the grid and particle-abundant holes were there in many locations of the grid, some adjacent to particle-scarce holes. These could be clearly observed at higher magnifications than 3000.

Grids which were not used for sampling and unused grids which were placed in the case of sampled grids were subjected to observation under the microscope. The grids unexposed to the exhaust had no *fine* particulate on them. They had many strange *large* black particles, especially near the boundaries of the square holes. Water-bubble like structures were also found in those grids. Their analyses helped in distinguishing the particles from engines from those already present in the grid during further observations. The grids which were unexposed to exhaust, but placed in the storing-case of sampled grids, showed presence of very few particulates. They also had strange black particles and water-bubble like structures. There was no accumulation of particles near the broken edges of film unlike sampled grids and the number concentration of particulates in square holes varied from 1 to 4. There was no particle in some square holes.

2.5.3 Thermophoretic sampling procedures

A preliminary round of 8 tests was done to optimize the sampling conditions. The moisture content in the hot exhaust was noted to be very high, occasionally breaking the thin carbon films on the grid. This was evident from the fact that moisture droplets with tiny pieces of the thin carbon layer were detected in the downstream portion of the sampling location on the grid holder. The various operating modes used for the tests are given in the table below.

Table 2.1: Test modes for preliminary round of tests

Sl. No.	Test mode details for the sampling system			
	Temperature of the heating wire (°C)	**Sampling Time (sec)**	**Flow rate of hot exhaust through the sampler (lit/min)**	**Grid-Holder Type**
1	400	60	2	Magnetic
2	400	300	2	Magnetic
3	400	120	2	Magnetic
4	400	60	5	Magnetic
5	400	60	1	Magnetic
6	400	60	2	Non-magnetic
7	300	60	2	Magnetic
8	200	60	2	Magnetic

As per the design calculations, the temperature of heating wire and the sampling time were to be 400 °C and 60 seconds respectively. The pump at the downstream of the sampler could provide a maximum flow rate of 5 lit/min. Different values of temperature, sampling time and flow rate were tried as shown above. The temperature of 400 °C gave the largest number of particles deposited compared to 300 °C and 200 °C due to the higher temperature gradient. Hence the temperature of 400 °C was found to be most suitable for particle deposition. It was desired to reduce the sampling time in order to minimize the rise in temperature of the grid. There were several hundreds of particles even at 60 seconds. Inorder to reduce the number of particles to a level in which it could be counted easily and also to reduce the rise in temperature of the grid, a sampling time less than 60 seconds was desired. The flow rate of 2 lit/min gave good results (more particles) compared to 1 lit/min and the amount of moisture accumulated near the sampling location was high for 5 lit/min. Thus the flow rate of 2 lit/min was most desired among the values used for the tests. The magnetic grid holder gave better results than the non-magnetic one. This was due to the decrease in temperature gradient at the sampling location (due to the recess over the grid) for the non-magnetic holder. The particles were so abundant in all cases of test modes and it was difficult to count them accurately due to the crowded nature of them on the grid.

It was decided to use the magnetic holder and reduce the sampling time to 10 seconds keeping the temperature at the design value of 400 °C and the flow rate at 2 lit/min. The sampler heater was turned on 4-5 minutes prior to sample collection.

Various tests were to be performed at different loads, speeds and different pilot diesel fuel quantities.

2.6 Results

Tests were conducted in both Engine A and Engine B. Tests conducted in Engine A were sampling at different load conditions and different speed conditions. Samples were taken at different quantities of pilot fuel in Engine B.

2.6.1 Varying Speed and Load

All the tests were performed at the optimized operating conditions mentioned in the previous section. Test data of significance for the engine and exhaust system for some load conditions of sampling are given below.

Table 2.2: Test data for Engine A (@1800 RPM)

Test Data	75% load & 1800 RPM	50% load & 1800 RPM	25% load & 1800 RPM
Intake air temperature (°C)	22.8	22.4	22.5
Manifold air temperature (°C)	63.7	59.9	63.5
Manifold air pressure - static (kPag)	160.3	94.3	46.5
Exhaust pressure (stack) (kPag)	5.9	3.5	2.1
Air flow (kg/hr)	2640	1972	1459
Diesel flow (kg/hr)	6.2	5.6	5.4
CNG flow (kg/hr)	76.1	51	28.9
Engine oil temperature (°C)	99.8	95.6	91.2
CO (ppm-dry)	533.4	281.4	361.6
CO_2 (%-dry)	6.1	5.7	4.6
NO_x (ppm-wet)	583.6	550.6	327.1
O_2 (%-dry)	10.2	11.1	13.1
CH_4 (ppm-wet)	354.7	403.4	470.6
tHC (ppm-wet)	201.5	177.3	238.1
Exhaust gas temperature (stack) (°C)	488	456	399
Average peak cylinder pressure (bar)	145.1	109.8	64.7

The first round of tests were carried out at different load conditions, keeping the speed at the rated value (1800 RPM). The tables of results for samples at different load conditions are given below. The term "size" for the particles or spherules mentioned here refers to the maximum linear dimension. The average number concentration was obtained from the data on 4-5 square holes in each case. Measurements and observations are

summarized in Tables 2.3 and 2.4. A discussion of typical and atypical particle structures is given in 2.6.3.

There were numerous tiny particles whose sizes were less than 500 nm. These were difficult to count accurately, but attempts were made to compute the average number of particles of sizes less than 500 nm per μm^2 on the grid. This was 7, 10, 13 and 15 for the load conditions of 5%, 25%, 50% and 75% respectively. Thus the approximate average numbers of these kind of particles per square hole were 70000, 100000, 130000 and 150000 respectively.

The second set of tests were performed at different speed conditions keeping the load at 50%.

Table 2.3: Agglomerate and spherule measurements, Engine A

Speed (RPM)	Load (%)	N_{small}[1] (nm)	N_{big}[2] (nm)	Sizes (nm)			
				Agglomerates		Spherules	
				min-max	avg.	min-max	avg.
1800	5	70K	52	25-500	561	25-200	75
1800	25	100K	71	50-2300	534	50-170	63
1800	50	130K	95	30-10000	458	30-600	42
1800	75	150K	146	15-8000	269	15-500	62
1800	85	-	> 200	70-20000	278	20-800	28*
1500	50	-	93	25-10000	547	25-1250	48
1600	50	-	98	25-4500	428	25-1500	43
1700	50	-	109	30-2300	313	30-100	40

[1]Estimate of number of agglomerates/spherules with L<500 nm per 0.01 mm^2

[2]Count of number of agglomerates/spherules with L>500 nm per 0.01 mm^2

*large error estimating primary size because of abundant liquid

The number of primary particles in the agglomerates varied from 1 to a few hundreds for 5% and 25% loads and from 1 to a few thousands for other conditions. As indicated in the table, the number of particles with sizes less than 500 nm was much larger compared to those with sizes greater than 500 nm.

Table 2.4: Comments on particle structure for Engine A

Speed (RPM)	Load (%)	[1]Observed particle structures
1800	5	Agg, sph, Rock, SPH
1800	25	Agg, sph, Rock, SPH
1800	50	Agg, sph, Rock, SPH, liquid, compact
1800	75	Agg, sph, Rock, SPH, liquid, compact
1800	85	Agg, sph, Rock, SPH, much liquid, compact
1500	50	Agg, sph, Rock, liquid, worm, compact
1600	50	Agg, sph, Rock, liquid, worm, compact
1700	50	Agg, sph, Rock, liquid, worm, compact

[1]Agg = typical chain agglomerate of spherules
sph = small independent spherule
SPH = large spherical or near-spherical particle
Rock = large angular particle
worm = elongated worm or bacteria shaped particle
compact cluster = black spots like black berries
liquid = evidence of liquid layer from motion of particles under beam

Attempts were made to find the approximate average values of sizes for particles and spherules at various conditions. The average size of spherules were calculated from 25 typical spherules of varied dimensions from different particles. The average sizes of particles were calculated from 20-50 particles at each condition. Values are given in the table 2.3 along with the ranges (max, min).

The composition of a selected region in a typical particle (Micrograph Figure D5-590 in Appendix D) was determined using Energy Dispersive analysis by X-ray spectroscopy method. The area of reference for the analysis was specified as a rectangular area in the spherule-abundant region in the top-left side of the picture. The particle was part of the sample taken at 75% load and 1800 RPM. The elemental chemical composition is given in the table below.

Table 2.5: Preliminary Elemental Analysis of an Agglomerate from Engine A

Element	Percentage weight
Oxygen	60.42
Carbon	28.31
Silicon	6.09
Nickel	2.56 (present in grid)
Chlorine	0.67

Sulphur	0.64
Calcium	0.51
Zinc	0.38
Copper	0.30
Potassium	0.13

Apart from the elements listed above, traces of iron and cobalt were indicated, but these elements are present in the vicinity in the instrument. 100 kV was used for the X-ray spectroscopy, whose penetration depth was high. This permitted to find the composition of the whole particle bundle. The spectroscopy method could not detect the presence of elements whose atomic weights are less than that of beryllium. Hence hydrogen content in the particle could not be determined. No attempt has been made to validate these measurements, so they must be viewed with extreme caution.

2.6.2 Varying Pilot Fuel Quantity

Engine B was operated with different pulse-widths of the diesel pilot. The values used for the pulse-widths were 0.65 ms, 0.48 ms and 1.1 ms. The tests were conducted at low load and speed conditions. The mode of test (Mode No. 2 of AVL 8 mode) was selected in such a way as to have a pronounced effect of varying pilot quantity in particulate emission. Test data for the engine (Table 2.5) and particle measurements (Table 2.6) are given below. Note that the diesel fuel consumption increases by a factor of 6 in going from 0.48 ms pulse to 1.1 ms.

Table 2.6: Test data for Engine B

Test Data	0.48 ms	0.65 ms	1.1 ms
Engine speed (RPM)	732	732	732
Brake Torque (Nm)	402	407	409
Intake air temperature (°C)	19.6	19.8	20.2
Manifold air temperature (°C)	18.2	19.1	19.6
Manifold air pressure - static (kPag)	7.4	7.4	7.6
Exhaust pressure (stack) (kPag)	2.8	2.8	2.8
Air flow (kg/hr)	394	393	394
Diesel flow (kg/hr)	0.2	0.8	1.3
CNG flow (kg/hr)	5.4	5.1	4.8
Engine oil temperature (°C)	93.6	92.5	92.3
CO (ppm-dry)	165.8	106.8	85.9
CO_2 (%-dry)	3	3.1	3.2

NO_x (ppm-wet)	650.4	651.4	668.8
O_2 (%-dry)	15.6	15.5	15.6
CH_4 (ppm-wet)	258.7	145.8	124
tHC (ppm-wet)	114.3	71.8	63.1
PM emissions (g/bhp-hr)	0.0560	0.0565	0.0543

Table 2.7: Agglomerate and spherule measurements, Engine B

Pilot pulse (ms)	N_{small}[1]	N_{big}	% counts in size ranges				Sizes (nm)			
							Agglomerates		Spherules	
			3-100[2]	100-500	500-1000	>1000	min-max	avg.	min-max	avg.
0.48	45	5	60	30	8	2	30-4000	415	30-1000	50
0.65	81	9	60	30	8	2	25-10000	348	25-600	65
1.1	102	18	70	15	10	5	60-6000	495	20-180	53

[1]number of agglomerates with L>500 nm in a 0.01 mm^2 area

[2]minimum observable size ~ 3 nm

Table 2.8: Comments on particle structure for Engine B

pilot pulse (ms)	[1]Observed particle structures
0.48	Agg, sph, Rock, SPH, liquid
0.65	Agg, sph, Rock, SPH, liquid
1.1	Agg, sph, Rock, SPH, liquid

[1]Agg = typical chain agglomerate of spherules
sph = small independent spherule
Rock = large angular particle
SPH = large spherical or near-spherical particle
liquid = evidence of liquid layer from motion of particles under beam

The average sizes of particles and constituent spherules were calculated. 25 typical spherules of different dimensions from different particles. The approximate percentage concentration of different size-ranges of particles* was found out by visual counting and the data was used in selecting particles from the different size-ranges to compute the approximate average.

*An approximate estimate of the percentage abundance of particles in different size-ranges are given in table 2.7. These measurements were taken from visual observation under the microscope. The approximate average sizes of particles were calculated taking this size distribution into consideration. An example of the method of calculation of the approximate average size of particles is given here -

Let the relative abundance of different size-ranges of particles are as given below.

Percentage of particles in the size range A = 50 %, with an average size of "a"

Percentage of particles in the size range B = 30 %, with an average size of "b"

Percentage of particles in the size range C = 20 %, with an average size of "c"

Then average size of particles = $[(50 \times a) + (30 \times b) + (20 \times c)]/100$

2.6.3 Description of selected photos (micrographs)

Brief descriptions of the micrographs of particles from the samples of Engine A and Engine B are given below. The micrographs referred here correspond to those in section D.1 of Appendix D with the same figure numbers. The micrographs were carefully selected out of more than one-hundred pictures taken from the samples to give representation to all conditions of tests in both Engine A and Engine B incorporating most of the interesting features observed.

2.6.3a Micrographs from Engine A

D5-587: This picture was taken from the sample at 75% load and 1800 RPM. The magnification is 10K. A big structured particle agglomerate is seen with hundreds or perhaps, thousands of spherules. Some spherules are bigger than others. These kind of big agglomerates are generally less in number all over the grid compared to particles in other size-ranges. The accurate counting of the number of spherules in such particles are near-impossible since the actual particle is in 3-D. Certain regions in the particle bundle are blackened completely and offer no clue on the size of spherules there. Innumerable number of smaller particles are seen all across the picture. Many of them are single spherules or particles with less number of spherules. The sizes of spherules in the smaller particles are less compared to the big agglomerate. This kind of scattering of numerous particles on the sampling grid hinders accurate counting of number of particles on it.

D5-589: This picture was taken at 75% load and 1800 RPM. The magnification is 20K. A big particle is seen with liquid layer at its top and bottom portions. A particulate agglomerate, with a size slightly higher than 1 micron, is seen near the top right corner of the picture. The structure of the big particle at the centre is not clear due to the presence of the liquid region. Numerous smaller particles are seen scattered all over the picture, some of them being single spherules.

D5-590: This picture with a magnification of 15K is from the sample taken at 75% load and 1800 RPM. A group of particle bundles are seen with thousands of tiny spherules in them. A close look at the picture reveals that the agglomerate on the top left corner and bottom right corner are connected by structured branches of particle. There are many other smaller particles in the picture. Some of the independent single spherules are very small in size compared to those that constitute the particle bundles. Energy dispersive analysis using the X-ray spectroscopy method was done to find the composition of a region of the particle (a rectangular region in the bundle at the top left corner) and the results are given in the "Results" section.

D5-597: This picture with a magnification of 20K was taken from the sample at 75% load and 1800 RPM. A number of black round-shaped particles are seen crowded together in some regions. These are the "compact clusters" listed in the tables of section 2.6.1 and 2.6.2. There is a thin liquid-phase layer beneath them. The round particles tended to move while they were focused in the electron microscope. The peripheries of these round particles are not circular, but seem to be composed of tiny spherules. Near the central area of the picture, we can see some of these round particles sticking together along with the liquid. The crowding of these round particles along with liquid region might be a stage in the formation of big-sized particles. A lot of smaller particles are seen scattered on the region. The sizes of tiny spherules in them are less compared to the tiny round formations at the peripheries of round black particles.

D5-599: This picture was taken from the sample at 75% of load and 1800 RPM. The magnification is 20K. The picture is similar to D5-597, but the round-shaped black particles are of different sizes here. Some are not even round, but elongated or peanut-shell-shaped. Small structured agglomerates are seen beneath the liquid layer and round-shaped particles.

D5-603: This picture with a magnification of 20K was taken from the sample at 75% load and 1800 RPM. A large particle is seen which has varied amount of darkness on its

surface. Some round-shaped black particles like those mentioned in D5-597 and D5-599 are seen near the big particle which could be an indication that the crowding of round-shaped particles with liquid layer has succeeded in forming a big-sized particle. No visible liquid layer is seen in this picture. These type of big particles with unclear surfaces and structure are rare on the grid and are usually neglected for counting the number of spherules. The big particle is about 5 microns in size.

D5-611: This picture was taken from the sample at 5% load and 1800 RPM. Its magnification is 30K. Particles with unclear surfaces and edges are seen, which are not suitable for counting the number or noting the shapes and sizes of spherules. Such particles were very rare in the grid.

D5-613: This picture has a magnification of 30K and is a typical representation of the kind of particulate material in the sample taken from 5% load and 1800 RPM. The particles are composed of countable number of spherules and the sizes of spherules varied among the particles seen in the picture.

D5-615: This picture with a magnification of 3K was taken from the sample at 85% load and 1800 RPM. This represents the typical distribution in many regions on the grid at this condition. A group of large particle agglomerates are seen along with some liquid layers, round-shaped particles and cloudy regions. This appearance in many regions of the grid impeded the counting of number of particles too. At this value of magnification (3K) for other conditions, a very few particle agglomerates could be seen on the grid (it would be just like a plain picture with few tiny black spots here and there) and they too would be clearly visible only if the magnification value is raised.

D5-616: This picture was taken from the sample at 85% load and 1800 RPM. It has a magnification of 10K and still is not clear enough to study the structure. A lot of smaller particles are seen scattered all over the vicinity. The big particle has regions of varied darkness indicating the crowding of spherules there.

D5-618: This picture has a magnification of 30K and is taken from the sample at 25% load and 1800 RPM. The big bundle of particle has a layer of bubble-like structure beneath it. The bundle could consist of thousands of spherules of varying sizes, considering the fact that it actually in 3-D. Such kind of particles were very rare in this condition.

D5-619: This picture was taken from the sample at 25% load and 1800 RPM. Its magnification is 30K and shows two particles - one with hundreds of spherules and the other with countable number of them. The latter has typical structure of engine-exhaust particulates and is much different from the former in terms of abundance of spherules.

D5-620: This picture with a magnification of 20K was taken from the sample at 50% load and 1800 RPM. Many big round-shaped particles are seen embedded in the particle bundle with tiny spherules. The tiny spherules in the particle bundle are having sizes of a few nanometres.

D5-621: This was taken at a load of 50% and speed of 1800 RPM. The magnification is 10K. Big sized agglomerates are seen with countless number of spherules. Such particles were rare in this condition, but cloudy structures of particles were seen in many regions on the grid. A lot of tiny particles are also seen.

D5-627: This picture with a magnification of 40K shows a long liquid-phase particle in the shape of a bacterium. It was taken from the sample at 50% load and 1500 RPM. Numerous tiny particles are also seen. The size of the liquid-phase particle is more than a micron. Such kind of small liquid-phased particles were found in samples at other conditions too.

D5-629: This picture with a magnification of 12K shows big cloudy structures of particles from the sample taken at 50% load and 1500 RPM. A rod-shaped region is seen in the agglomerate near the centre with a liquid droplet at its root. The rod seems to point

towards the centre of the picture. The tiny spherules are seen with varying in sizes and shapes.

D5-630: This picture shows a particle which resembles a fading star. It is taken from the sample at 50% load and 1600 RPM. It has a magnification of 12K. The particle has a layer of liquid phase surrounding it. Numerous smaller particles are seen embedded in that liquid region. The particle seems to be one without much tiny spherules, but a single body of exhaust material.

D5-633: This picture with a magnification of 30K shows some typical structured particles at the condition of 50% load and 1700 RPM. Many tiny particles are also seen. The particles seem to be completely in the solid phase with individual spherules larger in size than those of the tiny particles scattered around.

2.6.3b Micrographs from Engine B

D9-571: This picture is taken from the sample at a pilot pulse-width of 1.1 ms. It has a magnification of 10K. It shows a structured agglomerate with some droplets of liquid. Some regions in the particle are not seen clearly, but the spherule dimensions could be measured from other regions. Such kind of particles were not rare in this condition. A few smaller particles are also seen.

D9-572: This picture is taken from the sample at a pilot pulse-width of 1.1 ms. It has a magnification of 15K. It shows big black regions along with clear and typical structures of particle agglomerates. This kind of particles were generally rare and was not considered while counting the number of spherules.

D9-574: This picture is taken from the sample at a pilot pulse-width of 1.1 ms. It has a magnification of 15K. It shows a big agglomerate of particle with hundreds of spherules.

Some unclear black areas are there in the particles which impede the accurate counting of the number of spherules.

D9-576: This picture is taken from the sample at a pilot pulse-width of 1.1 ms. It has a magnification of 15K. It shows a "foggy" particle with unclear boundaries between spherules. The particle seems to consist of many layers of spherules of varying sizes. Two other smaller particles are seen on its side, one being a single independent spherule.

D9-577: This picture is taken from the sample at a pilot pulse-width of 0.48 ms. It has a magnification of 15K. It shows a club-shaped particle with hundreds of tiny spherules. The spherules are in many layers and branches in the particle and of varying sizes. Such particles were rare in this condition.

D9-579: This picture is taken from the sample at a pilot pulse-width of 0.48 ms. It has a magnification of 15K. A particle agglomerate is seen with innumerable number of spherules. The surface of the particle is having varied darkness. The spherules near the edges of the particles are clear. The spherules are of many different shapes.

D9-582: This picture is taken from the sample at a pilot pulse-width of 0.48 ms. It has a magnification of 15K. It shows a particle agglomerate which is rod-shaped. As in the case of D9-579, the spherules near the periphery of the particle are clear. The other regions in the particles have varied darkness.

D9-584: This picture is taken from the sample at a pilot pulse-width of 0.48 ms. It has a magnification of 15K. It shows a big black particle (called a "rock" in 2.6.1 and 2.6.2) without any branches or well-defined spherule structures. This was counted as a exhaust particulate material during the analysis due to its relatively small size compared to other non-combustion particles usually found on the unexposed grids.

D9-588: This picture is taken from the sample at a pilot pulse-width of 0.65 ms. It has a magnification of 10K. It shows big bundles of particles which were rare for this condition. Numerous smaller particles are also seen in the picture which are having countable number of spherules. The spherule sizes of some tiny particles are less when compared to that in the big bundles.

D9-589: This picture is taken from the sample at a pilot pulse-width of 0.65 ms. It has a magnification of 40K. A typical structured agglomerate is seen with varied sizes of spherules. The spherules are of many different shapes. At this condition, most of the particles were this type of typical structured agglomerates.

D9-591: This picture is taken from the sample at a pilot pulse-width of 0.65 ms. It has a magnification of 20K. A big structured agglomerate is seen with many tiny particles. The size range of spherules in the smaller particles are less compared to the big agglomerate.. The spherules are of different sizes and shapes.

D9-594: This picture is taken from the sample at a pilot pulse-width of 0.65 ms. It has a magnification of 15K. It shows a big black particle with numerous tiny structured particles. Such kind of particles were very rare in this operating condition. The sizes of spherules in the structured particles are comparable. The big black region is unclear, but its edges show that it is composed of hundreds of tiny spherules.

D9-598: This picture is taken from the sample at a pilot pulse-width of 0.65 ms. It has a magnification of 8K. a region in liquid phase is seen with a few structured particles. Numerous particles are seen embedded in the liquid region. Some tiny single spherules are also seen. The liquid layer is seen in contact with a round-shaped black particle.

D9-600: This picture is taken from the sample at a pilot pulse-width of 0.65 ms. It has a magnification of 10K. A big bundle of particle is seen with many branches and varied sizes of spherules. One big liquid droplet which resembles a big-sized spherule is also

seen. There are many other particles seen in the picture with less number of spherules. Some independent spherules are also seen.

2.7 Discussion of Results

As mentioned earlier, tests were conducted with two engines - Engine A and Engine B. The preliminary set of tests for optimizing the sampler settings, set of tests at different loads and set of tests at different speeds were conducted using Engine A. The tests at different pilot pulse-widths were conducted using Engine B. The particles were subjected to visual observation under Transmission Electron Microscope.

2.7.1 Discussion of results from Engine A

The tests at different load conditions were conducted to study the effect of different loads in particulate emission. The different loads tried were 5%, 25%, 50%, 75% and 85%. All the tests under this category were performed at the rated speed of 1800 RPM. As can be seen from the results, the most significant feature was the increase in the number concentration on the grid as the load increased. It is logical to assume that as the load increased, more fuel is consumed to keep the speed at the set value, thereby increasing particle emission. Observation under the microscope revealed that the difference in the distribution of particles on the grid from 75% load to 85% load was tremendous compared to that with other load conditions. It was difficult to count the number concentration of particles manually at 85% load, since in most locations on the grid, the particles were so crowded together that the surface was almost fully dark. There was a considerable quantity of liquid at this load condition. Almost every particle-shapes noted in the whole analysis were present in the sample at 85% load. The smallest spherule size noted was 20 nm. In general, the minimum spherule size was large for samples from smaller load conditions. The biggest particles were noted for the sample at 85% load. Particle bundles with sizes of about 20 microns were found. The largest particle at 25% load was having a size of about 2.3 microns. This was the minimum size for the largest particle at any load condition. The minimum size of spherule found was 15 nm in size at a load condition of 75%. Typically, the minimum-sized spherules were those independent ones in all load cases. The maximum-sized spherule of 1.5 micron was found at 85%

load. Typical structured agglomerates of particles were found in all load conditions. There were a large number of tiny independent spherules in all load cases. The number of big particles of sizes above one micron was very less for all loading conditions except at 85% load.

The tests at different speed conditions were conducted at a fixed load of 50% for Engine A. The speeds tried were 1500 RPM, 1600 RPM, 1700 RPM and 1800 RPM. There was no specific trend in the number concentration of particles on the grid at various speed conditions in that order. There was no significant difference on the appearance of scattered particles on the grid at different speed conditions. The minimum size for the spherules was 25 nm. As in the case of different load conditions, the smallest spherules were generally the tiny single spherules without attachment with any big particles. Different shapes of particles were observed in all cases as mentioned in the results. The size of some particles were large, but the number of spherules they had was less compared to some other round-shaped particles which had thousands of spherules grouped together still maintaining the size within certain limits. The largest particles of about 10 microns were found at 1500 RPM and 1800 RPM.

The average sizes of particles and spherules were calculated as mentioned in the results. The average sizes of spherules were calculated from 25 typical spherules of varied sizes from different micrographs. The average sizes of particles were calculated from 20-50 particles of varied sizes from the micrographs. The particle distribution on the grid generally varied with different locations in each case. This could be a source of error for computing the average sizes of particles using micrographs.

2.7.2 Discussion on results from Engine B

The tests at different pilot pulse-widths were conducted to determine the difference in particulate emission at different quantities of pilot fuel. The pulse-widths used for the tests were 0.48 ms, 0.65 ms and 1.1 ms. The tests were conducted at low load

and low speed conditions. The load condition was kept at 21% for the three tests. The speed was 732 RPM in all the cases. The mode of tests was Mode 2 of the AVL 8 mode tests and was selected because the CNG (compressed natural gas) consumption is the lowest and the effect of varying pilot diesel quantity at this mode should be most pronounced.

As can be seen from the results, the average number concentration of particulates whose sizes were more than 500 nm increased with increased quantities of diesel fuel. This shows that particulate emission for diesel combustion is more compared to that for natural gas. The average-sized spherules in the tests with Engine B were generally larger than that of Engine A. The average sizes for spherules for those particles whose sizes were higher than 500 nm were 146 nm, 124 nm and 108 nm for the 0.48 ms, 0.65 ms and 1.1 ms cases respectively. However, if the spherules from smaller particles and independent ones were considered, the average sizes of spherules are 50 nm, 65 nm and 53 nm respectively. (this is contrary to the case with Engine A where the average sizes of spherules in big particles and that from all particles were almost the same). The biggest spherule was seen in the sample at 0.48 ms and its size was about one micron. The largest particle of about 10 microns in size was found in the sample at 0.65 ms. The spherule with the minimum size of 20 nm was observed in the sample at 1.1 ms. There was no specific trend in the average size of spherules at different cases. The presence of liquid masses were rare in the sample at 1.1 ms compared to the two other cases. The spherules and particles were in many different shapes in each condition as mentioned in the results.

The other test conditions during the tests are given in the results. The exhaust pressure in the stack was the same at 2.8 kPag for all the cases. The CO concentration decreased with increasing diesel consumption, whereas CO_2 emission in the exhaust increased with the diesel fuel consumption. The NO_x emission too increased with the pilot fuel consumption. The percentage quantity of oxygen in the exhaust was almost constant throughout the experiments. Traces of methane and hydrocarbons reduced with increasing pilot fuel consumption.

Generally, the particulates collected on the grid at various conditions of the engine for Engine B were less abundant compared to that from Engine A.

2.7.3 Comparison of predicted and observed deposition rates

The comparison of the predicted and observed deposition rates on the sampler need to be calculated in each case to get an idea about the performance of the sampler. The data on particle and spherule sizes as obtained from the TEM analysis and the data on particulate emission as obtained from filter sampling tests were used to predict the number of particles deposited on the grid. The observed number concentration of the particles were compared with the predicted number concentration to compute the comparison of observed and predicted deposition rates on the sampler at different test modes. Since filter measurement data of particulates with Engine A was not available during the time of thermophoretic sampling, data taken on a previous date with same conditions in three cases was used for the calculation of comparison of deposition rates.

Table 2.9a Observed and predicted deposition (post-test calculations) for Engine A

Item	75%	50%	25%
Filter data (mg)	0.77	0.8	2.45
PM solid mass (kg)	4.6 e-7	4.8 e-7	1.47 e-6
Volume of gas (m^3)	0.2236	0.2284	0.5788
Exhaust pressure (kPa)	107.3	104.9	103.6
Gas density (kg/m^3)	0.5554	0.5430	0.5363
Volume of PM/m^3 of gas	9 e-10	9.1 e-10	1.1 e-9
Avg. size of a spherule (nm)	62	42	63
Avg. volume of a particle (m^3)	4.7 e-20	3.5 e-20	5.61 e-20
Thermophoretic velocity (m/s)	0.1516	0.138	0.133
Number/m^3 of particles	1.9 e10	2.6 e10	1.97 e10
Predicted number of particles/0.01 mm^2	287	361	261
Observed number of particles/0.01 mm^2	146	95	71
Ratio of observed & predicted values	0.25	0.26	0.27

Table 2.9b: Observed and predicted deposition (post-test calculations) for Engine B

Item	0.48 ms	0.65 ms	1.1 ms
Filter data (g/bhp-hr)*	0.0560	0.0565	0.0543
PM solid mass (kg)	0.00024	0.00024	0.00023
Volume of gas (m^3)	0.15	0.15	0.15
Exhaust pressure (kPa)	104.9	104.9	105
Gas density (kg/m^3)	0.5430	0.5430	0.5435
Volume of PM/m^3 of gas	6.8 e-7	6.9 e-7	6.61 e-7
Avg. size of a spherule (nm)	146	124	108
Avg. volume of a particle (m^3)	1.9 e-16	1.2 e-16	7.25 e-17
Thermophoretic velocity (m/s)	0.1419	0.1480	0.1346
Number/m^3 of particles	3.6 e9	5.7 e9	9.12 e9
Predicted number of particles/0.01 mm^2	51	85	122
Observed number of particles/0.01 mm^2	5	9	18
Comparison of observed & predicted values	0.097	0.106	0.147

*bhp for the engine at all modes was 42; sampling time for filter samples was 10 minutes; flow rate was 180 lit/min; dilution ratio was 12

The deposition efficiency of the sampler depends on thermophoretic velocity. The thermophoretic velocity of the particles was calculated in each case with the formula given in Appendix B. The viscosity of the gas was assumed to be the same as that for air. Since the temperature of the gas at the site of deposition was to be taken into account, it was assumed to be 673K (the temperature set by the heating wire) for all cases. The liquid content in the particulate matter was assumed as 40% by weight. From the particulate solid mass and gas sample mass (as obtained from the filter sample data), it was able to find out the volume of particles per unit volume of gas. For this, densities of particle and gas were required. Gas density was calculated assuming it as perfect gas and taking the gas constant for air for calculations. The exhaust pressure and temperature were also considered. The density of particle was taken as equal to that of carbon after assuming them to be composed of carbon only. From the sampler data, average volume of particle in each case was found out from the data on the average size of spherules and approximate number of spherules in each particle. It was assumed that the average spherule is spherical in shape. With the thermophoretic velocity and the number concentration of particles per unit volume of gas, the number of particles deposited per square hole during the sampling period could be calculated. This value was then

compared with the actual observed sampler data. A sample calculation of the comparison of deposition rates at a case is shown below.

Sample calculation @ 50% load and 1800RPM for Engine A

Filter data = 0.8 mg = 0.0008 kg

Solid mass in the PM = 4.8×10^{-7} kg

Sample (exhaust gas) mass = 124 g = 0.124 kg

Temperature of gas inside the sampler = 673 K

Exhaust pressure = 101.4 (barometric) + 3.5 (gauge) = 104.9 kPa

Density of gas = P/(R×T) = $(104.9 \times 10^3)/(287.036 \times 673)$ = 0.54303 kg/m^3

Hence volume of this gas = 0.228348 m^3

Therefore mass of particulate material per m^3 of gas = 3.503×10^{-6} kg

Volume of particulates per m^3 of gas = 9.1×10^{-10} m^3

Average size of spherule = 42 nm (sampler data)

Average volume of a particle = 3.5×10^{-20} m^3 (sampler data)

Number/m^3 of particulates = 2.6×10^{10} (particles in 1 m^3 of gas)

Temperature gradient = 9.9×10^6 K/m

Thermophoretic velocity (V_{th}) = 0.138 m/s

(details of finding temperature gradient are given in Appendix B; details of average particle sizes are given in table 2.3)

Hence number/m^2/s = number/m^3 × V_{th} = 3.59×10^9

Predicted number of particles per square hole (0.01 mm^2) for 10 seconds = 361

Average number of particles deposited per square hole for 10 seconds = 95 (sampler data)

Ratio of observed deposition rate to predicted deposition rate = 0.26

2.7.4 Sources of error during the tests and analyses

The analyses was performed with utmost care to get reliable results, but there were some sources of error which need to be noted. Some of the major sources of error during the analyses were:

1. During sampling, the temperature of the grid was increasing due to heat transfer. This could have reduced the effective temperature gradient, thus getting deviated values in practice when compared to the design calculations. Calculations showed that this could reduce the theoretical thermophoretic velocity by 8%, if the heating wire was switched on continuously for 15 minutes.
2. All the measurements using the microscope were done manually and were subject to human errors, especially in the counting of small particles.
3. The total number of particles in each case was difficult to find due to the enormity in their actual number. Thus the average number concentration of particles whose sizes are above 500 nm was taken in each case. The number of tiny particles were very large compared to larger particles and hence it was difficult to get an accurate value of the mass or volume of all particles deposited on the grid.
4. It was difficult to find out the accurate number of spherules in most big particles. This number is specified as thousands in the results in many cases, but accurate values could not be used for the sampler deposition rate calculations.
5. Micrographs show two dimensional images of the particles whereas in reality they are three dimensional. This could make variations in the actual number of spherules in each case.
6. It was found in the cases with Engine A that the moisture content was large. Moisture was present at the exit of the pump and many particles that were embedded in it could have passed through the sampling area without deposition on the grid. This was evident from the fact that moisture particles with parts of broken carbon film embedded in them were cited, especially in higher load conditions.
7. The liquid-phase particles and regions present on the grids were difficult to quantify, but they also form part of particulate emission by the engines.

8. Assumption was made during the design of the sampler and during the computation of ratio of observed and predicted deposition rates that no particles would deposit on to the surfaces upstream of the sampling location. This could have made some deviations in the predicted values of design from the reality.
9. The tests done with the engines were not repeated to check consistency in the average number concentration of the particles deposited on the grid.

2.8 Conclusions

2.8.1 Conclusions regarding performance of the sampler

Sampling onto a TEM grid could be done using several particle-collection methods. Thermophoretic and diffusion modes of collection are prominent ones and these modes require sufficient temperature and concentration gradients respectively to effectively collect particles. Since sub-micron particle mechanics is not completely understood as on date, it is difficult to design a TEM grid sampler which could be 100 percent perfect. Moreover, the dimensions of the TEM grid offer special design challenges for holding it effectively in the hot exhaust. The major conclusions that could be drawn on the performance of the sampler are -

1. The factors affecting thermophoretic sampling onto TEM support grids were well identified and were taken into account while devising the new design for collecting sufficient number of particles in different size ranges from HPDI engines to observe under the Transmission Electron Microscope.
2. The thermophoretic sampler for collecting particulate material from engines could be made and the device could be used to collect samples at different engine conditions for HPDI engines.
3. Particles in many different shapes were collected during the sampling tests.
4. Particles having sizes from 15 nm to about 20 microns could be collected on to the TEM grids.
5. The observed deposition was less in all cases when compared with the predicted deposition, but many assumptions were made in computing predicted deposition which could alter the computed values from the actual ones.
6. The rise in temperature of the grid during sampling has contributed to reducing the thermophoretic velocity. It was computed that continuous heating of the sampler for 15 minutes could raise the temperature of the grid by about 30 °C, thereby reducing the thermophoretic velocity by 8%.

7. Considerable amount of data was obtained from the new grid sampling technique for collecting HPDI particulates, by incorporating proper design techniques based on theory.

2.8.2 Conclusions regarding particulate emission by HPDI engines

The major conclusions on particulate emission by HPDI are:

1. Particles from HPDI engines had different sizes and shapes with some interesting features
2. The particle number concentration increased with the loading condition, due to increase in fuel consumption
3. No notable trend in the difference in particulate number concentration at different speed conditions were found for speeds near the rated value
4. The particle size varied from about 15 nm to about 20 microns in some cases for Engine A and from about 25 nm to about 10 microns for Engine B
5. The particulates were composed of spherules, whose number varied from one to several thousands in some cases
6. There were numerous tiny single spherules at all load and speed conditions for Engine A and at all data points for Engine B
7. The size of spherules varied from 15 nm to 800 nm for samples from Engine A and from about 25 nm to 1.5 microns for Engine B
8. The spherules were in many different shapes for both Engine A and Engine B, but majority of them were near-spherical in shape
9. For Engine B, the average size of spherules for particles larger than 500 nm was higher than that for smaller particles
10. The average particle number concentration as deposited on the grid increased significantly with increasing pilot pulse-widths. It increased from 45 to 81 and then to 102 for particles where L<500 nm and increased from 5 to 9 and then to 18 for particles where L>500 nm. In contrast, filter based-sampling sowed almost no change in emissions.

References

Automotive Handbook (1993), 3rd Edition, Robert Bosch GmbH, Stuttgart.

Burmeister, L. C. (1993), *Convective Heat Transfer*, John Wiley & Sons, Inc., New York.

Friedlander, S. K. (1977), *Smoke, Dust and Haze*, Wiley Interscience, NewYork.

Heywood, J. B. (1988), *Internal Combustion Engine Fundamentals*, McGraw Hill, New York.

Hinds, W. C. (1999), *Aerosol Technology*, John Wiley & Sons Inc., NewYork.

Maynard, A. D. (1995), *Aerosol Science and Technology*, 23:521-533.

Rogak, S. N., Flagan, R. C., Nguyen, H. V. (1993), *Aerosol Science and Technology*, 18:25-47.

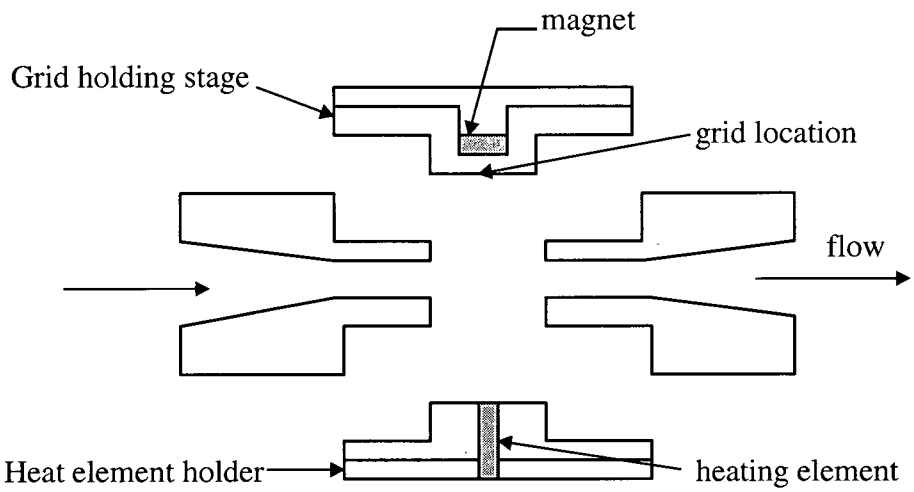

Figure 2.1: Picture showing the basic structure of the thermophoretic sampler reported by Maynard (1995).

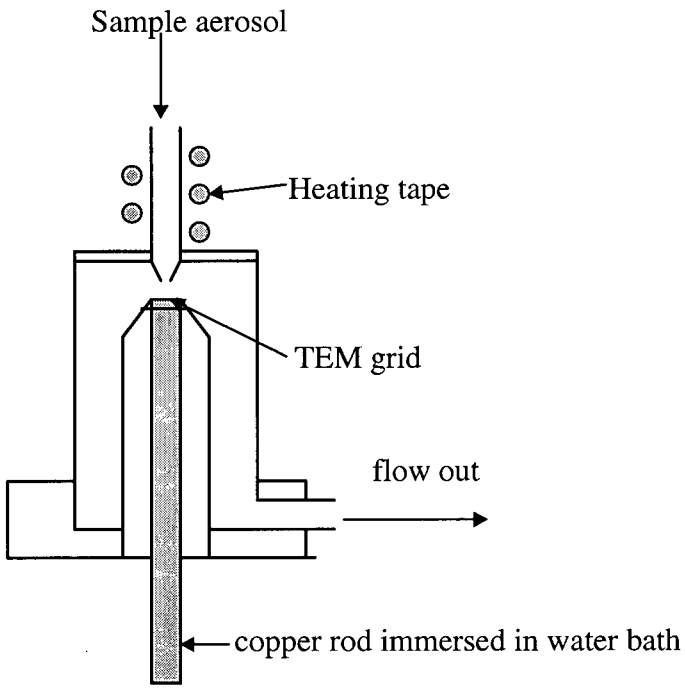

Figure 2.2: Picture showing details of the structure of the thermophoretic sampler reported by Rogak et al. (1993)

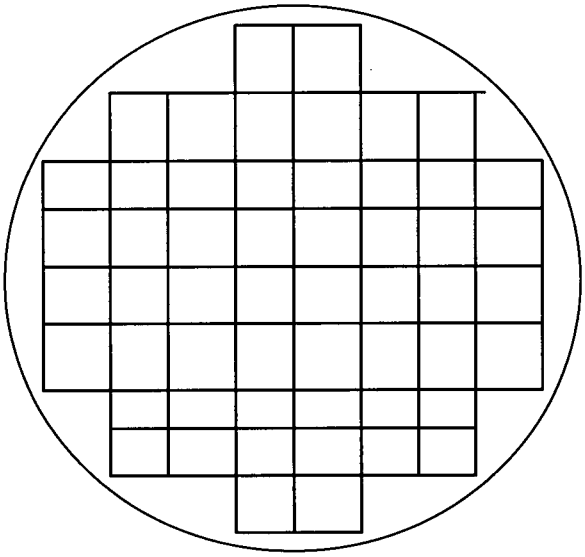

Figure 2.3: Picture showing the structure of a TEM grid (not to scale). The grid is about 3 mm in diameter and about 25 microns thick. The grids used for the present work had about 200 square holes in each of them.

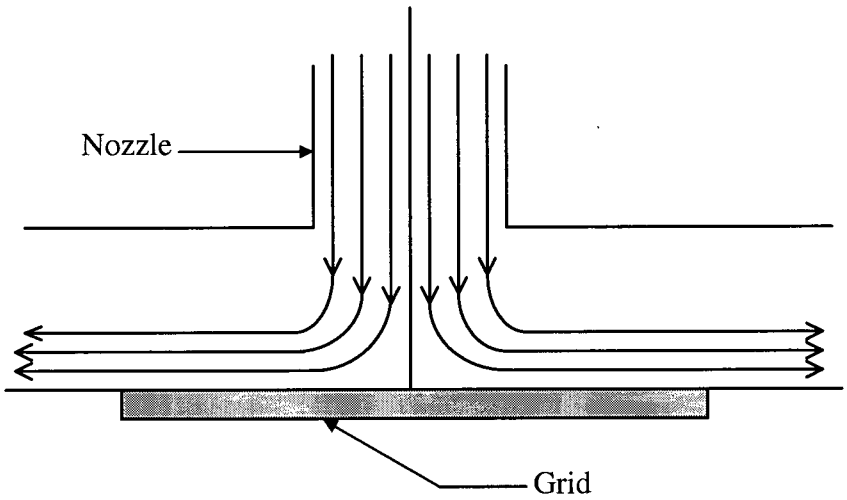

Figure 2.4: Picture showing the streamlines of flow at the sampling location of the new thermophoretic sampler. Both the diameter of the nozzle tip and the distance between the nozzle tip and the grid are equal to 1 mm (not to scale).

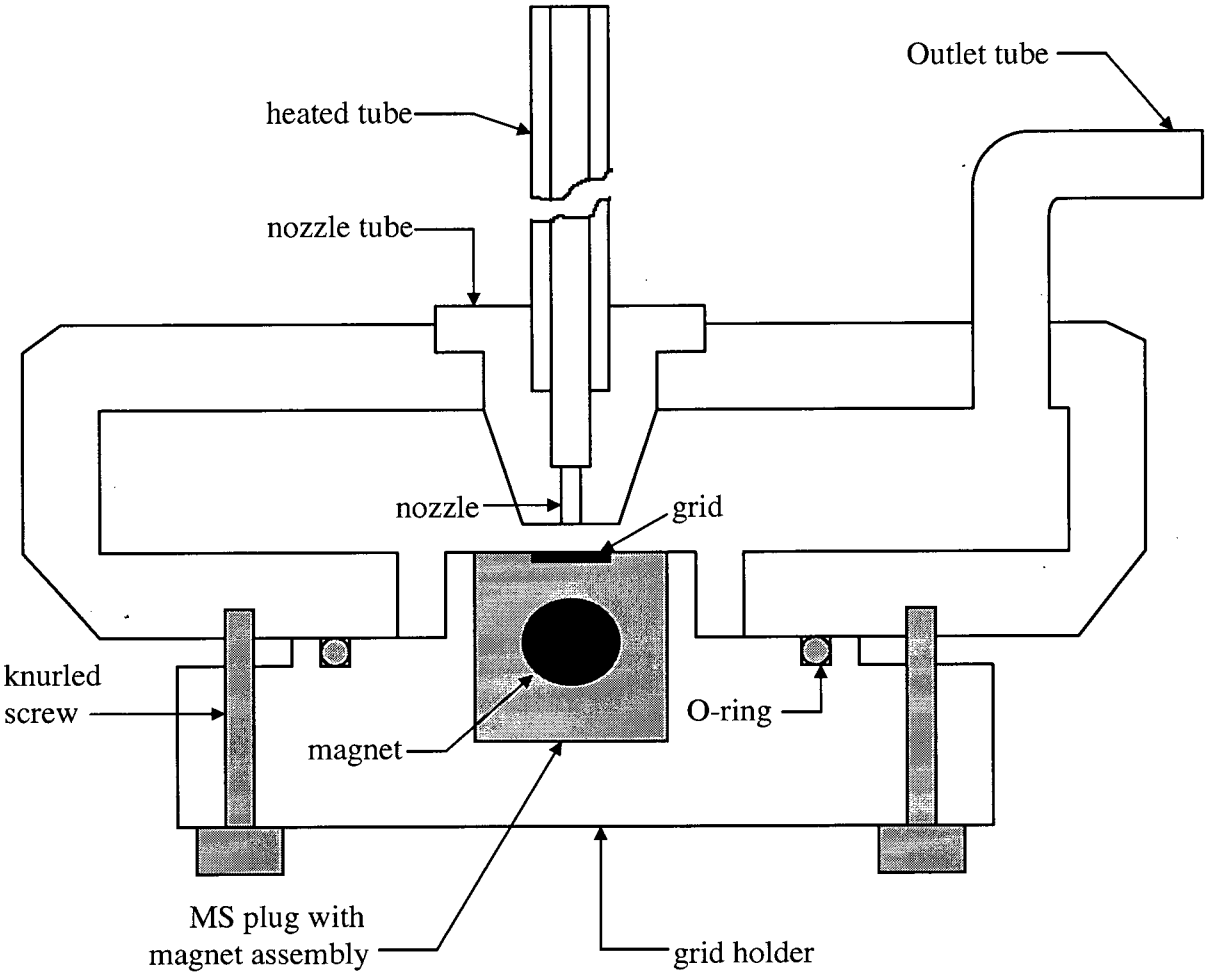

Figure 2.5: Picture showing the main body of the new thermophoretic sampler with magnetic grid holder (not to scale).

APPENDIX: A

PICTURES OF THE SAMPLER

&

OTHER FIGURES

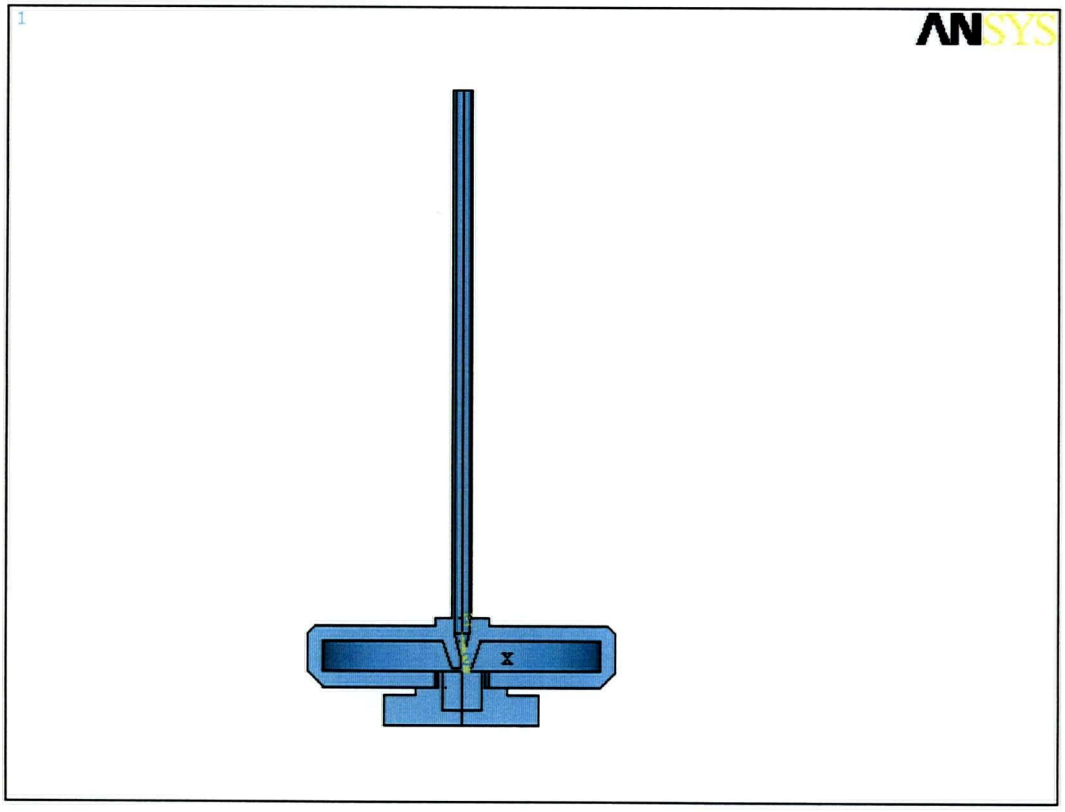

Figure A1: Sectional view of the sampler modeled with ANSYS

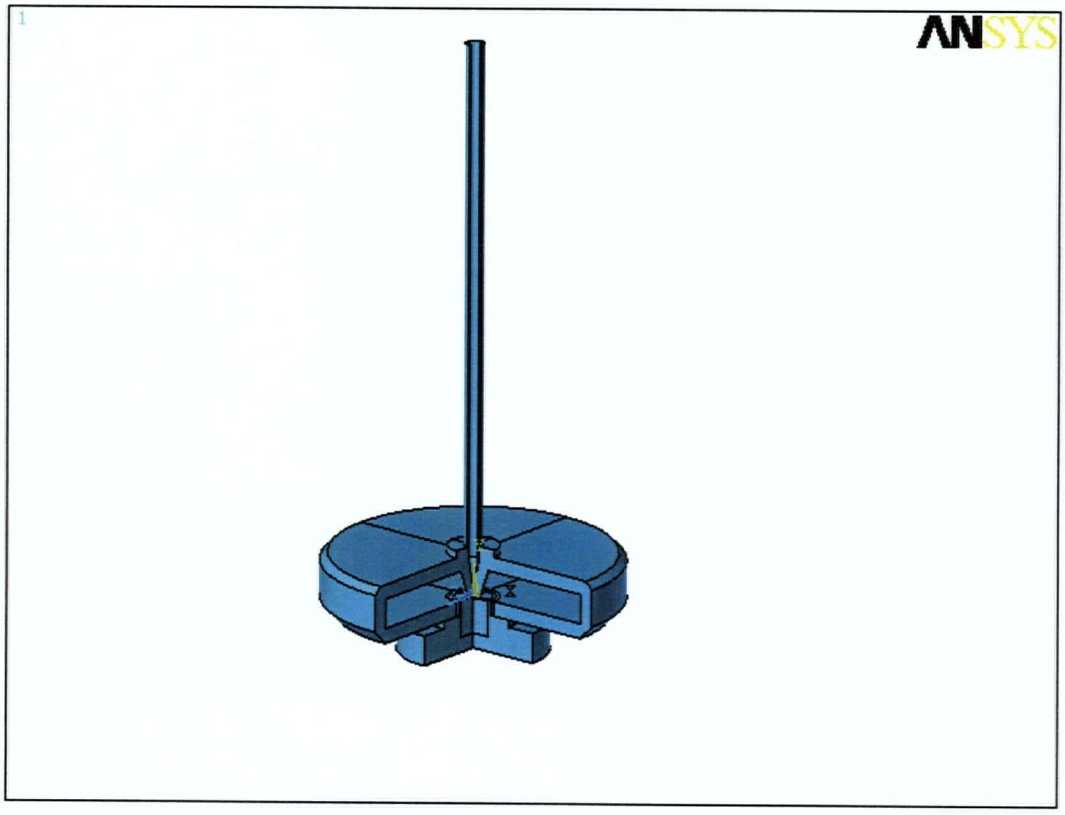

Figure A2: 3-D sectional view of the sampler modeled with ANSYS

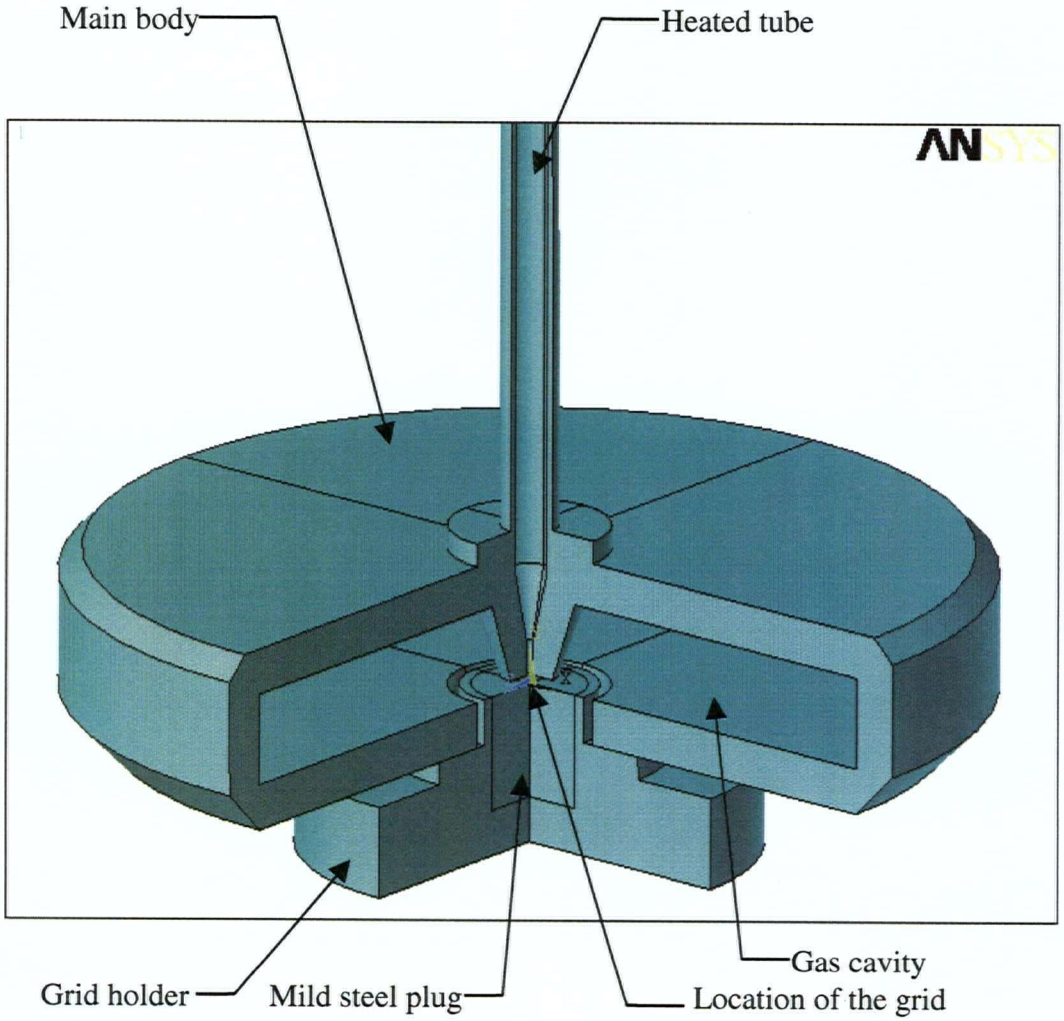

Figure A3: Close view of the main body of the sampler

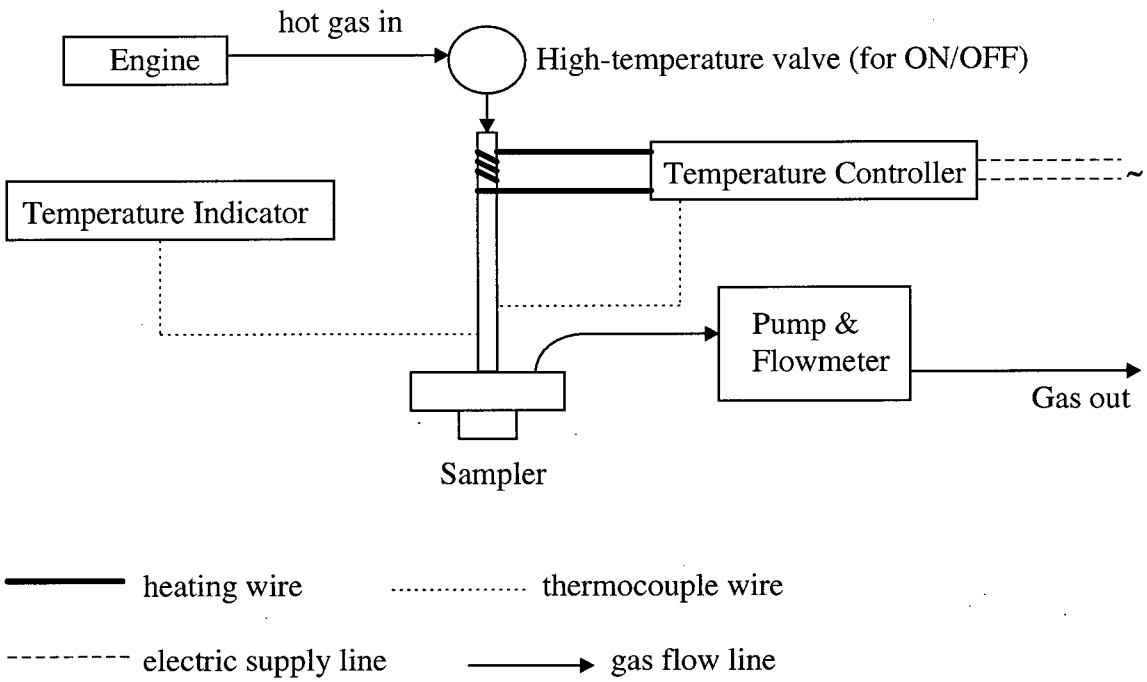

Figure A4: Block diagram of the sampling system

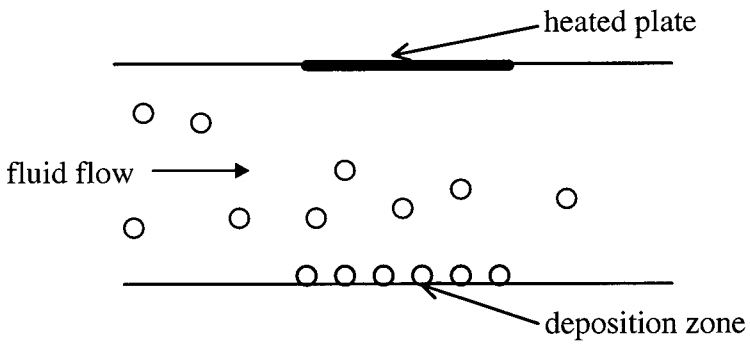

Figure A5: Conceptual diagram of a thermophoretic precipitator

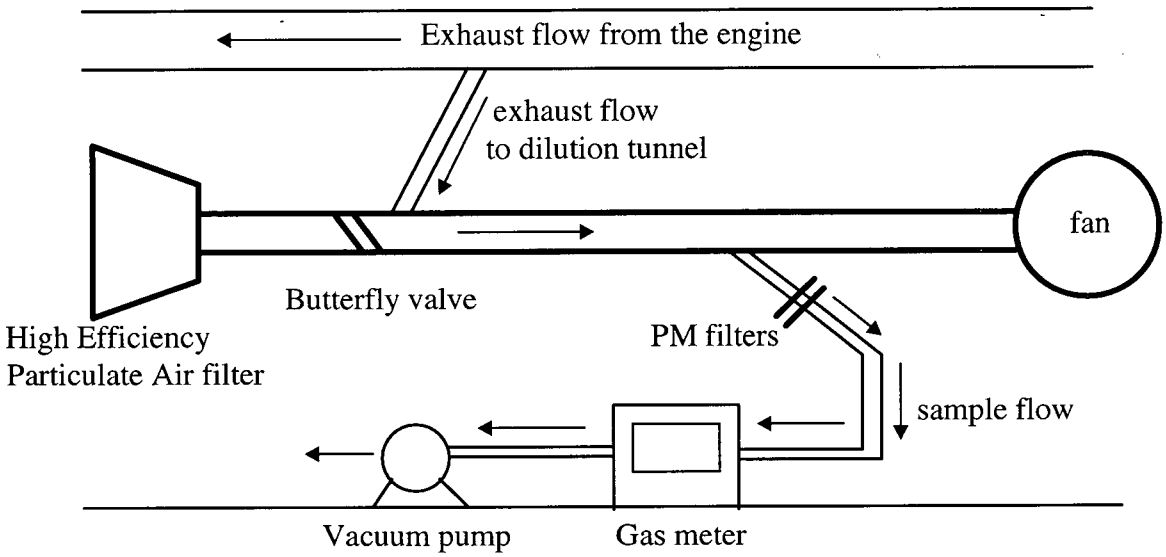

Figure A6: Mini-dilution tunnel system for measuring particulates

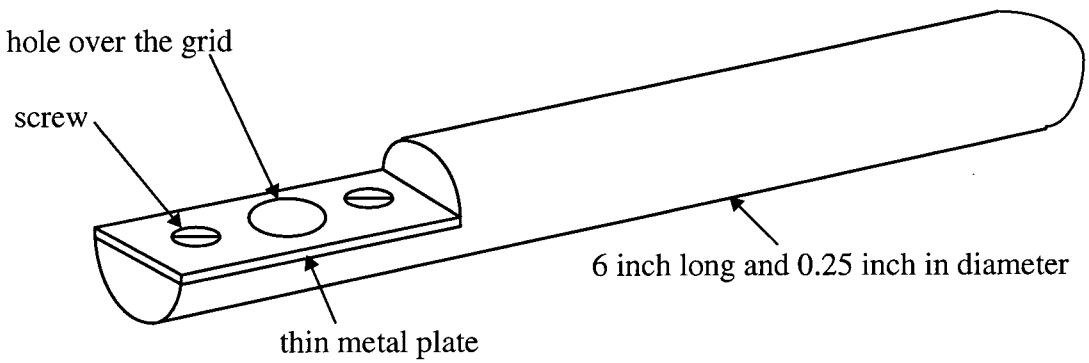

Figure A7: Holder for TEM grid in dilution tunnel
(Not to scale)

APPENDIX: B

DESIGN CALCULATIONS

B.1 Theoretical calculations for deposition through various modes

As mentioned in Chapter 2, the major assumptions for the theoretical calculations for the design are -

- The incoming gas jet is at a uniform temperature as adjusted by the temperature control unit, just before it impinges on the grid
- There is no loss of particles anywhere in the sampler unit upstream of the grid site
- Even though the exhaust particles have weird shapes, they are assumed to be perfect spheres with specific diameters (equivalent diameters of spheres of carbon with the same volume)
- Since sampling is done at a location not too far from the cylinder outlet, lack of sufficient time to oxidize/react in the new conditions preserves the homogeneity of the particles and as a result, the particles are composed of pure carbon only
- Density of elemental carbon is 2300 kg/m^3
- The density of exhaust gas is the same as that of atmospheric air
- Viscosity of exhaust gas and air are the same
- The thermal conductivity of exhaust gas is same as that of air

Even though the sampler is primarily of thermophoretic in nature, all the important modes of particle deposition, viz. Diffusion and Inertial impaction also play their role in the overall process.

In the following calculations, assumptions are made on the emission of particles and also on the average size of them. Soot emission from a typical diesel engine is assumed to be 20 mg/m^3.

Average diameter of particles is assumed as 200 nm. Volume of each particle = $(4/3).\pi.r^3$ = $4/3 \times \pi \times (100 \times 10^{-9})^3 = 4.189 \times 10^{-21}$ m^3, where 'r' is the radius of the particle. We have the density of pure carbon as 2300 kg/m^3. This shows that 20 mg of carbon occupies

a volume of 8.7×10^{-9} m^3. Hence the number of particles per m^3 of exhaust gas can be calculated as $(8.7 \times 10^{-9} / 4.189 \times 10^{-21}) = 2.076 \times 10^{12}$.

B.1.1 Deposition through the Thermophoretic mode

The temperature maintained for the exhaust gas is supposed to be 400°C and the temperature of the grid is assumed to be 21°C.

Thermophoretic velocity, $V_{th} = (-3.\eta.C_c.H.\nabla T)/(2.\rho_g.T)$ [Hinds, 1999]

where η = viscosity in $Ns/m^2 = 18.325 \times 10^{-6}$ (same as that of air),

∇T = temperature gradient in $K/m = 9.9 \times 10^6$ (calculations shown in section B.5),

ρ_g = density of gas in $kg/m^3 = 1.2041$,

T = temperature of the particle in K = 673.

$C_c = 1 + (2.52\lambda/d) = 1 + (2.52 \times 65 \times 10^{-9})/(200 \times 10^{-9}) = 1.819$,

where C_c = a constant

λ = mean free path of particles in meter $= 65 \times 10^{-9}$

d = diameter of each particle in meter $= 200 \times 10^{-9}$

$H = (1/(1 + 6\lambda/d)).((k_a/k_p + 4.4\lambda/d)/(1 + 2k_ak_p + 8.8\lambda/d)) = 0.1257$,

where H = a constant

k_a = thermal conductivity of gas in $W/m\text{-}K = 241 \times 10^{-4}$

k_p = thermal conductivity of the particle in W/m-K = 5

Hence $V_{th} = 0.077$ m/s for a particle size of 200 nm.

Deposition rate of particles on to the grid,

$number/m^2/sec = number/m^3 \times V_{th} = 2.076 \times 10^{12} \times 0.077 = 1.594 \times 10^{11}$

Therefore the number of particles deposited per square hole on the grid per minute is 95640, considering uniform deposition of particles over the grid (the grid has a fine mesh on it which has a lot of square holes with each hole's side dimension being 0.1 mm). Thus it is assured that sufficient number of particles will be deposited on the grid through this method.

Deposition efficiency at different particle sizes for thermophoretic mode

The deposition efficiencies for particles with different sizes are given in the table below. Deposition efficiency is calculated by dividing the number of particles that are expected to get deposited on the grid by the number of particles contained in the gas flowing through the sampling zone. It is expressed as percentage in the table. Particulate concentration of 20 mg/m^3 and gas flow rate of 2 litres per minute were assumed for all cases. The assumed and calculated parameters are:

Particle mean free path (m) =	6.50E-08
Thermal conductivity of air (W/mK) =	2.41E-02
Thermal conductivity of particle (W/mK) =	5
Density of air (Kg/m3) =	1.2041
Temperature of exhaust (K) =	673
Temperature of the grid (K) =	294
Temperature gradient (K/m) =	9.90E+06
Viscosity of air (Ns/m2) =	1.83E-05
Density of carbon (kg/m3) =	2300
Diameter of grid (m) =	3.00E-03
Area of square hole in the grid (m2) =	1.00E-08
Acceleration due to gravity (m/s2) =	9.80E+00

Dia. (nm)	Concentration (#/m^3)	V_{th} (m/s)	#/grid/min	Deposition eff. (%)
10	1.66 e+16	0.062	4.4 e+11	1.32
20	2.07 e+15	0.063	5.6 e+10	1.34
50	1.33 e+14	0.065	3.7 e+9	1.38
100	1.66 e+13	0.067	4.7 e+8	1.42
500	1.33 e+11	0.058	3.3 e+6	1.24

B.1.2 Deposition through the Diffusion mode

As mentioned earlier, deposition of particles takes place due to the concentration gradient between the surface and the flow field adjoining it.

The diffusion coefficient, $D = (kTC_c)/(3\pi\eta d)$, [Hinds, 1999]

where k = Boltzmann constant = 1.38×10^{-23} J/K

Thus D could be calculated as 4.89×10^{-10} m^2/s. Considering that the situation is equivalent to an infinite volume of stagnant aerosol maintained at a concentration of n_0

outside the gradient region, number of particles deposited during 1 minute is given by the expression, $2.n_0.(Dt/\pi)^{1/2}$,

where t = time in seconds = 60

n_0 = concentration of particles = $2.076 \times 10^{12}/m^3$

Thus the deposition rate could be computed as 401247614 $/m^2$ per minute. This shows that the number of particles deposited per square hole of the grid during one minute is 4. This mode is very weak compared to the thermophoretic method of deposition.

B.1.3 Deposition through the Inertial Impaction mode

Relatively larger particles are affected by this method. Hence the exact particle size distribution of the test-engine is required for accurate calculations of particle deposited under various conditions. However, a simple calculation to find the impaction efficiency is given here.

We have Impaction efficiency, $E_I = \Delta/h$, where Δ is the radial displacement of the particle from its original streamline and 'h' is the radius of the nozzle tip.

Relaxation time, τ, is the product of mass and mobility. Thus, $\tau = (\rho_p.d^2.C_c/18.\eta)$ [Hinds, 1999] = 5.073×10^{-7} s. Consider the velocity of the incoming jet, U, is 2 m/s. Hence $\Delta = (\pi/2).\tau.U = 1.594 \times 10^{-6}$ m. Therefore, $E_I = 3.188 \times 10^{-3}$.= 0.3188 %.

Volume of gas passing through the nozzle per second = $(\pi/4) \times 10^{-6} \times 2 = 1.57 \times 10^{-6}$ m^3. Since 1 m^3 of exhaust gas contains 2.076×10^{12} particles, this volume has 3259320 particles. Thus, taking the impaction efficiency into consideration, 10390 particles will be collected on the grid per second. Thus 882 particles will be deposited onto a square hole in one minute. This shows that this method is not as prominent as the thermophoretic mode.

B.2 Calculation of velocity at the tip of the nozzle

The flow rate is the same at the entrance to the tube and at the tip of the nozzle. Standard-sized tube with an outer diameter of 0.25 inch and an inside diameter of 0.1875 inch is chosen for conveying the gas to the grid. The opening at the tip of the nozzle is chosen as a circular one with an inside diameter of 1 mm (0.04 inch). Thus area at the tube is 1.7814×10^{-5} m^2 and at the nozzle is 7.854×10^{-7} m^2. Thus the velocity at the tip of the nozzle is 22.68 times that at the tube entry.

Thus, the mass flow rate = density × area × velocity = 2.145×10^{-5} kg/s, if the velocity through the tube is assumed as 1 m/s.

B.3 Calculation of approximate minimum length required for the heating pipe

Reynolds number for the flow, $Re = \rho dV/\eta = 312.93$, considering a velocity of 1 m/s through the tube. Hence laminar flow conditions apply for this problem.

For laminar flow, entrance length, Le, is calculated from $(Le/D) \geq 0.05Re$ [Burmeister, 1993]. Hence Le is at least 7.45 cm.

We have the heat transfer coefficient, $h = (3/2).(k/\delta_T) = 15.18$ W/m^2K,

where k = thermal conductivity of exhaust gas = 241×10^{-4} W/mK

δ_T = thermal boundary layer thickness = inner radius of the tube

Considering the temperature of exhaust gas entering the tube to be 473 K (in actual case, this will be higher), heat transfer to the gas from the inner surface of the tube after the entry length, $Q = h.A.\Delta T = 15.18 \times (\pi \times 0.0047625 \times L) \times (673 - 473) = 45.42L$ J/sec = $45.42L^2$ Joules/'l'.sec.

Time taken by the gas to travel the distance L = L sec.

Mass flow rate = 2.145×10^{-5} ; Specific heat of gas (air) = 0.993 kJ/kgK

Mass flow in L sec = $2.145 \times 10^{-5} \times L$

Hence heat capacity of the gas = $0.993 \times 2.145 \times 10^{-5} \times L = 2.13 \times 10^{-5} \times L$ kJ/K = $2.13 \times 10^{-2} \times L$ J/K. Therefore L = 9.38 cm, considering Q, heat capacity and temperature rise.

Thus the total minimum length required for the tube is 16.83 cm. The length of the tube should be at least 7 inches to supply enough heat to the gas.

B.4 Calculation of power requirement

The tube is to be heated by a flexible coiled heating element. The tube in turn transfers heat to the gas flowing inside it to raise its temperature to the required level. The tube is made up of stainless steel with the specific heat capacity of 510 J/kgK.

Mass of the tube = density $\times$ volume = $7930 \times (\pi/4) \times (0.00635^2 - 0.0047625^2) \times 0.1778$ = 0.0195 kg.

Consider the initial temperature of the tube be 300 K. Hence ΔT = 373 K

Therefore, the heat required to raise the temperature = 3709.5 J. If this is to be done in one minute, power required = 61.83 W.

Considering that heat is lost from tube only to the gas inside, heat lost in one minute to the gas (if gas has initial temperature of 473 K) is 255.6 J/min. Hence additional power requirement for maintaining the temperature of the tube for one minute is 4.25 W. Thus the minimum net power requirement for the tube is 66.08 W. In actual case, the power required depends on the rating for the heating element used. There are other power consuming accessories like the air blower (for cooling), flow-meter (for digital indication) and for a pump, if it is used in the circuit.

B.5 Calculation of heat transfer to and from the grid

The flow over the grid from the jet will be rotationally symmetric stagnation flow. For this flow, the condition is $Nu/(\sqrt{Re}.Pr^{0.4}) = 0.76$ [Burmeister, 1993]

Nusselt number, $Nu = hx/k = h \times 0.001/(241 \times 10^{-4})$,

where h = heat transfer coefficient in W/m^2K

x = D = diameter of the jet = 0.001 m

k = thermal conductivity of the gas in W/mK

Prandtl number, $Pr = \eta Cp/k = 0.755$

$Re = \rho UD/\eta = 1490.3$ (laminar flow)

Hence $h = 631.8\ W/m^2K$, to satisfy the condition.

For the calculation of heat transfer to the grid, the presence of carbon film is ignored. Let initial temperature of the grid be 294 K and that of gas be 673 K. Hence $Q = hA\Delta T = 1.666$ J/s. The maximum sampling time expected is 60 seconds, during which 99.96 joules of heat will be transferred to the grid. The temperature gradient over the grid will be 9.9×10^6 K/m.

Volume of the grid = $7.07 \times 10^{-10}\ m^3$ (approx.)

Mass of nickel grid (density is 8900 kg/m^3) = 6.2923×10^{-6} kg

Mass of copper grid (density is 8930 kg/m^3) = 6.31×10^{-6} kg

Specific heat capacity of nickel is 0.46 kJ/kgK

Specific heat capacity of copper is 0.385 kJ/kgK

Specific heat capacity of brass is 0.37 kJ/kgK

Density of brass = 8500 kg/m^3

The brass holder is larger than a cylindrical brass piece (diameter of 15 mm and height of 10 mm) having a mass of 15 g. Hence we can safely assume that the heat from the grid will be dissipated to at least 15 g. Thus the heat transferred to the grid indicates that the approximate rise in temperature of the grid and surroundings will be 18° per minute. This is concluded by assuming that the whole heat gained by the grid due to transfer from the incoming gas is dissipated to its holder material. The increase in the temperature of the grid causes inconsistencies between the actual deposition and the theoretical thermophoretic calculations. Inorder to minimize the error thus created, external air cooling using a cold air pump could be employed. The cooling should be done as near the grid as possible.

APPENDIX: C

FINITE ELEMENT MODEL ANALYSIS OF THE SAMPLER

C.1 Problem statement and objectives

The gas sampler is used to collect solid particulates in the exhaust through the process of thermophoresis, i.e. by creating a temperature gradient between the gas and the surface of the grid. The grid, made of nickel is placed 1 mm beneath the nozzle, so that the gas impinges on it directly from the tube. This causes convective heat flux to be induced on to the grid. The grid temperature also increases due to conduction from the tube, whose outer surface is maintained at a particular temperature by a heating wire. The temperature rise in the grid is not desired, since it diminishes the thermophoretic sampling efficiency. It is required to get data on the increase in grid temperature to get an idea of the reliability of the sampler. Information about the temperature rise in other parts of the sampler is also required. The temperature data at various conditions have been recorded experimentally. Finite element thermal analysis of the sampler after modelling it in the most suitable way and sub-modelling the grid region are needed to compare the results thus obtained with the experimental values.

The heat input values are the convective heat flux from the gas and conductive heat input from the outer surface of the tube. The loss of heat from the outer surfaces of the sampler body is to be neglected, since it is expected to be very small compared to the heat inputs.

The objectives of the thermal analysis using Finite Element Method (FEM) are -

- to find the temperature distribution throughout the model, 60 minutes after the start of application of external heat load.
- to find the temperature distribution at other time intervals like 15 minutes and 30 minutes.
- to solve the submodel to compute temperature rise in the grid after 60 minutes.
- to compare the results with experimental data available.

C.2 Finite Element Model

The modelling and thermal analysis using Finite Element Method (FEM) were carried out using the finite element software package, ANSYS 5.6. The various pictures of the model using ANSYS are given in Appendix A.

C.3 Element types used

The element types used for the project were Solid 75 (4-noded, 2D axisymmetric) for the whole model. Since the physical model of the sampler itself is axisymmetric, only one-half of the vertical section through the central axis of the model needed to be analyzed. Axisymmetric elements were specifically chosen to meet the realities of the problem. This means the data in the section could be used for the entire physical model. 3D solid (Solid 70) was tried as the element type after extruding the axisymmetric section through 360°. In this case, the complete model could be analyzed just like the actual physical model. But the model could not compute the temperature data and it collapsed due to the fact that it was difficult to keep the relative sizes of the elements at various locations in the model within a comparable limit. For example, the element sizes in the tube section were very small compared to that in other locations of the sampler. Axisymmetric solid (plane) elements permitted the use of sharp edges in the physical model.

C.4 Problem type

The problem was a 2D axisymmetric thermal analysis problem. The temperature at various locations in the sampler changes at each time interval and hence the problem was solved through transient thermal analysis. Steady state analysis was tried, but obviously, it gave a uniform temperature distribution for the sampler. Structural analysis was not done in this case since there were no considerable application of force on the sampler. There is no moving part in the sampler, which could make the problem to be solved using the dual mode for thermal and structural analyses. Since the only area of

concern in the model was thermal data, it was solved using pure thermal analysis. The problem was solved using the common h-method.

C.5 Boundary conditions

The modes of heat transfer in the sampler were conduction from the tube outer surface and convective heat flux from the hot gas. Radiation effects were neglected. Heat loss from the outer body surface of the model was also neglected. The outside surface temperature of the tube was maintained at 400° C (673 K) throughout. The incoming gas which is in contact with all the inner surfaces of the model was assumed to have an initial temperature of 400° C. Since the gas is heated through the application of thermal energy from the outer surface by maintaining a constant temperature, the temperature of 400° C was assumed to be maintained by the gas throughout the model. Convective heat transferred from the gas to the inner surfaces of the model was considered as an input heat flux in the computations. This could be accounted for 10 seconds only since it is the sampling time during which the hot gas flows inside the sampler body. The initial temperature of the whole model was assumed to be 21° C (294 K). The reference temperature for calculating thermal strain was also specified to be 21° C. The single boundary condition of constant temperature of 300° C at the outer surface of tube was tried for 3 time intervals to check whether the model was in consistency with experimental measurements.

C.5.1 Loads used

The main load used in the program was heat load through conduction from the outer surface of the sampler. This was specified as a constant temperature throughout the process in all cases of analysis. In some preliminary computations, the temperature was specified as 300° C, inorder to validate the model and to verify the results with that of experimental measurements. This value for temperature was used in three cases of different time intervals - 5 minutes, 10 minutes and 15 minutes. During this analysis, only

conduction was considered. During the subsequent analyses, the temperature was specified as 400° C. Inorder to get an idea about the trends in temperature distribution, pure conduction case was tried in all of the analyses with this temperature value. The heat flux loads due to convection was calculated using ΔT as the maximum possible temperature difference between the gas (at 673 K) and the inner surfaces (at 294 K) of the sampler. The general formula used was $Q_f = h*\Delta T$. The value of heat transfer coefficient (h) was assumed to be 15.18 W/m^2 K, which is the value computed analytically for the heat transfer in the inner surface of the tube region. Combined effects of conduction and convection was tried for 10 seconds (sampling time) and it was found that the convective heat load has no significant influence on the overall temperature rise in the sampler. As mentioned earlier, other effects like radiation, heat loss from the outer body surface etc. were neglected.

C.6 Submodel and boundary conditions for the submodel

The nickel grid is 3 mm in diameter and has a thickness of almost 0.1 mm with the coating on top. The temperature build-up in the grid is not desired during the process, since this could decrease the efficiency of the sampler in trapping particulates on to the grid. Inorder to determine the actual temperature rise in the grid, a submodel with the grid and surrounding areas of the mild steel plug were subjected to separate analysis. The boundary conditions were the (1) heat flux to the grid from the hot gas and (2) the temperature of the surrounding areas in the mild steel plug. The values of the temperature in the surrounding areas of the grid were taken from the temperature data output in the master-model in the same region. In the submodel also, the uniform initial temperature was specified as 294 K. The reference temperature was also specified as 294 K. The convective heat load was assumed to be there for 60 minutes, inorder to get the highest possible value of the temperature rise in the grid in 60 minutes.

For the submodel, the loads considered were the heat flux from the hot gas and conduction from the areas in the vicinity of the grid. The heat flux was computed as

mentioned earlier and the temperature values for the various nodes near the grid were taken from the results of the main model.

C.7 Analysis highlights

The problem was a case of pure thermal analysis and was basically a heat transfer problem. Transient analysis was done for the model in all cases since the temperature widely varied with time and as part of the main objectives, it was required to know the temperature data at various intervals of time. Steady state analysis gave uniform temperature distribution for the analysis. Transient analysis was done for various time steps with numerous sub-steps in each case.

The model was assumed to have a uniform initial temperature of 294 K. the reference temperature for calculating the thermal strains was also specified as 294 K. The analysis was done in such a way that at each time sub-step, the preliminary values were those computed during the earlier time step. For the first time sub-step, the boundary conditions specified were helpful in computing the initial data. In most cases, the program did sub-steps more than the minimum number specified.

C.8 Material properties

The materials used for the analysis were Stainless Steel (SS), Mild Steel (MS), Brass and Nickel. The properties (constant isotropic) of these metals, which are of importance to the program are indicated below :

Metal	*Density (kg/m^3)*	*Thermal Conductivity (W/mK)*	*Specific Heat (J/kgK)*	*Remarks*
Stainless Steel	7930	15	510	Used in the main model

Mild steel	7860	63	420	Used in the main and sub models
Brass	8500	110	370	Used in the main model
Nickel	8900	59	460	Used in the submodel

C.9 Finite Element model verification

The FE model was verified to know whether the results were reliable. For this, pure conduction mode was assumed and this was specified as constant temperature load of 300° C (573 K) on the outer surface of the tube. The analysis was done for three time intervals with suitable time sub-steps - 5 minutes, 10 minutes and 15 minutes. The initial uniform temperature and reference temperature were both 294 K. The results of this were compared with actual experimental measurements as:

Time interval	*FE analysis (° C)*	*Experimental (° C)*
5 minutes	23.57	23
10 minutes	31.6	29
15 minutes	42.33	36

It could be seen that the values are almost in agreement. The values in FE analysis is slightly larger due to the fact that heat losses from the outer body surface was not considered. But the results generally indicate the validity of the model and its ability to compute temperature distribution in a reliable way for the original physical model. In addition to this, a temperature input same as the assumed uniform initial temperature was specified and analysed for different time steps. In all cases, the result was uniform

temperature distribution throughout the model, with the temperature value being the assumed one.

C.10 Results and discussion

The results of the analyses at various conditions are given as plots. The analyses were done for 15 minutes, 30 minutes and 60 minutes. The element type for the analyses was Solid 75 (4-noded, 2D axisymmetric). Pure conduction cases were tried in each time steps, inorder to determine the average heat flux from the gas, which generally depends on the temperature difference between the inner surfaces of the model and the hot gas.

The temperature distribution results for the cases of 15 minutes, 30 minutes and 60 minutes are given in this section. The other basic details of the analyses are given in the tabular form below :

Details	*Solid 75 model*
Number of nodes	394
Number of elements	301
Degree of freedom	Temperature

The average value of temperature in the nodes in the vicinity of the grid was computed and used as boundary condition for the submodel. Generally, the temperature was concentrated in the tube region and decreased slowly towards the bottom surface in all time steps. As could be seen from the results by comparing the temperature values for pure conduction cases and dual mode cases, the convective heat flux was a minor heat load compared to conduction heat transfer.

The submodel was analyzed as mentioned earlier. The analysis of the submodel verifies the results of the master model in giving the same results for the vicinity under observation. The details of the sub-model analysis is tabulated below:

Details	*Sub-model*	*Remarks*
Element type used	Solid 75	since the model is plane, axisymmetric
Type of sub-problem	2D axisymmetric transient thermal analysis	one-half of the vertical section through the grid region was considered
Number of nodes	160	The elements and thus nodes were concentrated at the grid region
Number of elements	131	Elements in the grid region were perfectly rectangular in shape
Degree of freedom	Temperature	Single DOF
Temperature in the grid region	443 K	a temperature rise of 149° C at the grid
Whether consistent with the main model	Yes	Verification of results of the main model

The major sources of error which caused the results of the FE analyses to vary slightly from the experimental measurements and theoretical predictions are :

1. Neglecting the heat losses from the outer surfaces of the sampler body. In practice, there are vibrations during sampling from the engines, which make the heat loss more from the surface.
2. Neglecting radiation effects.
3. Errors in assuming constant convective heat flux (The heat flux in reality is a time-dependent function).
4. Use of constant isotropic values for the material properties.
5. There could be variations in the temperature provided by the heating wire to the outer surface of the tube in practice.

6. A constant initial temperature condition at a higher value was given as boundary condition for the sub-model, whereas in actual case, the initial temperature starts from 294 K and rises up to the value which was the boundary condition of the submodel.

C.11 Conclusions

The major conclusions of the finite element thermal analysis are -

1. The FE model gave results which are near-consistent with the experimental data.
2. The temperature rise in the grid was 149 K above the initial temperature of 294 K.
3. The high temperature was generally concentrated in the tube region.
4. As can be seen from the results, the mode of convection was much weak in raising the overall temperature.
5. The sources of error as mentioned earlier caused slight variations in the results when compared to the experimental data.
6. The submodel computation was consistent with the master model.

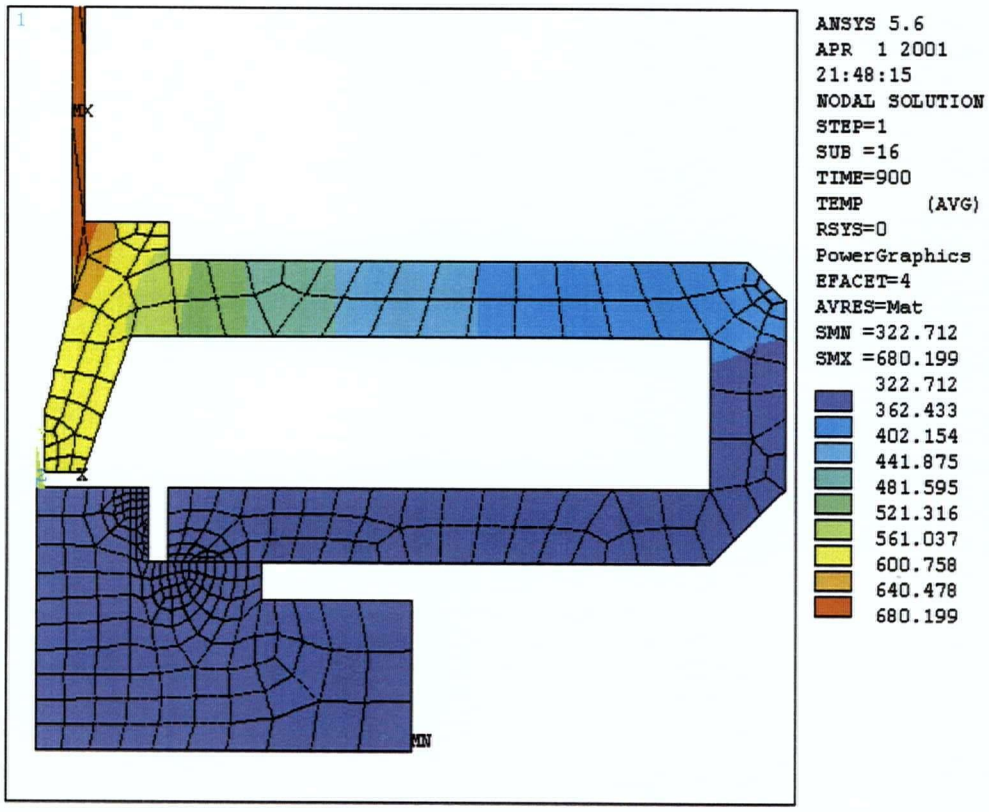

Figure C1: Temperature distribution in the main body of the sampler after 15 minutes

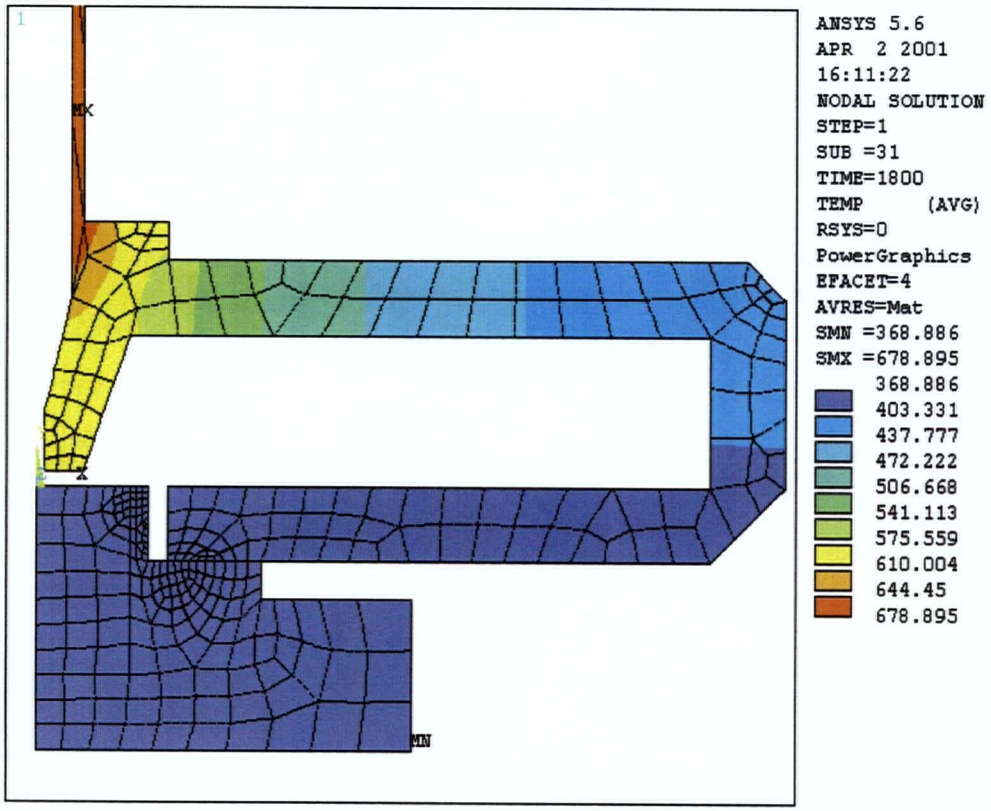

Figure C2: Temperature distribution in the main body of the sampler after 30 minutes

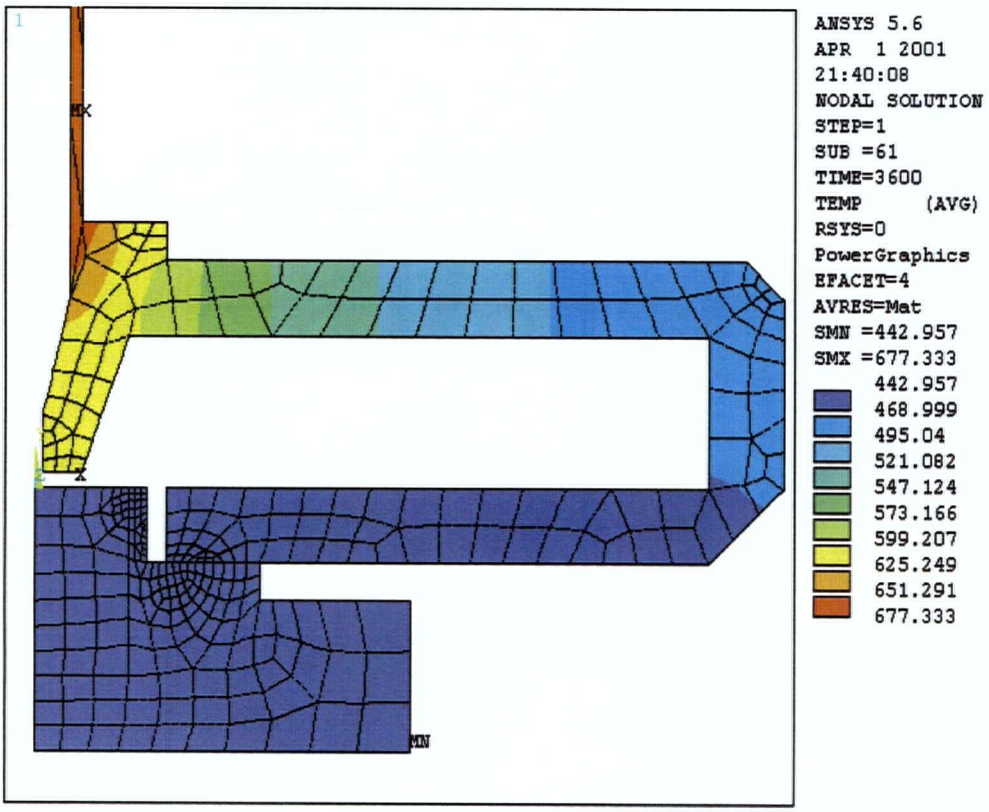

Figure C3: Temperature distribution in the main body of the sampler after 60 minutes

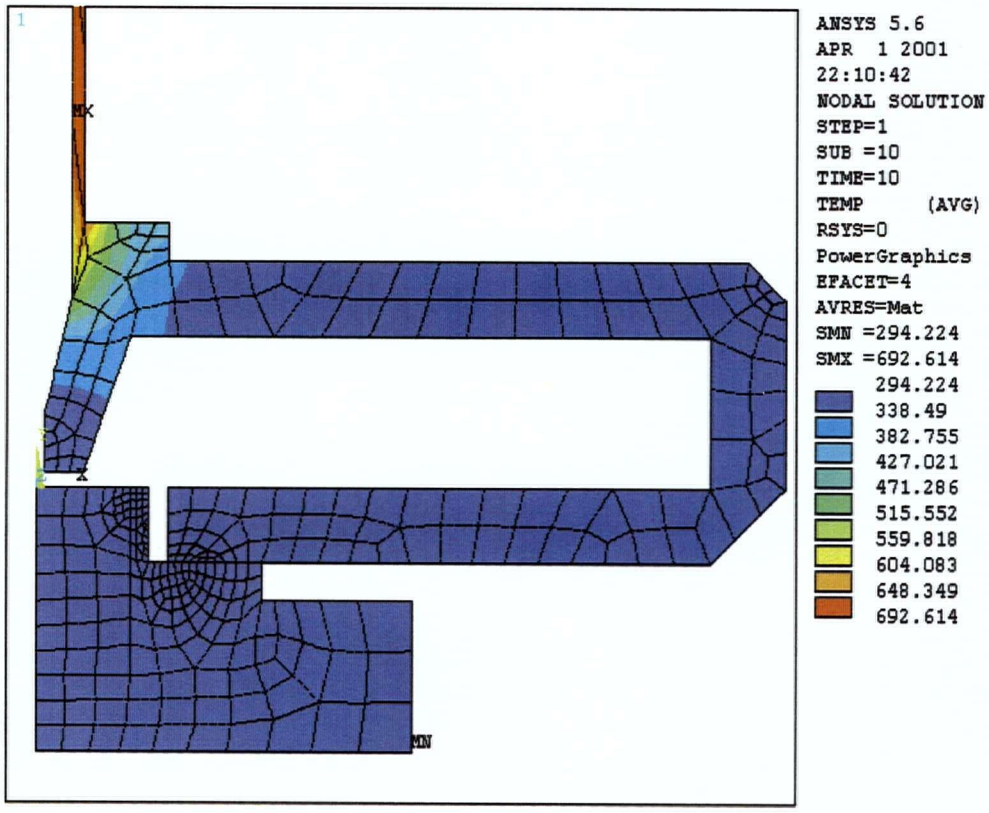

Figure C4: Temperature distribution in the main body of the sampler after 10 seconds (sampling time) with combined conduction (from heating wire) and convection (from hot exhaust gas). Convective heat flux occurs when gas flows through the sampler, i.e., during the sampling period. The temperature distribution shows that the convective heat flux due to the hot gas during the sampling period has no significant effect on the overall rise in temperature in the body of the sampler. Note that in actual operation, the heater is turned on 4-5 minutes before sampling, so the nozzle is hot during operation, not cold as shown in this figure.

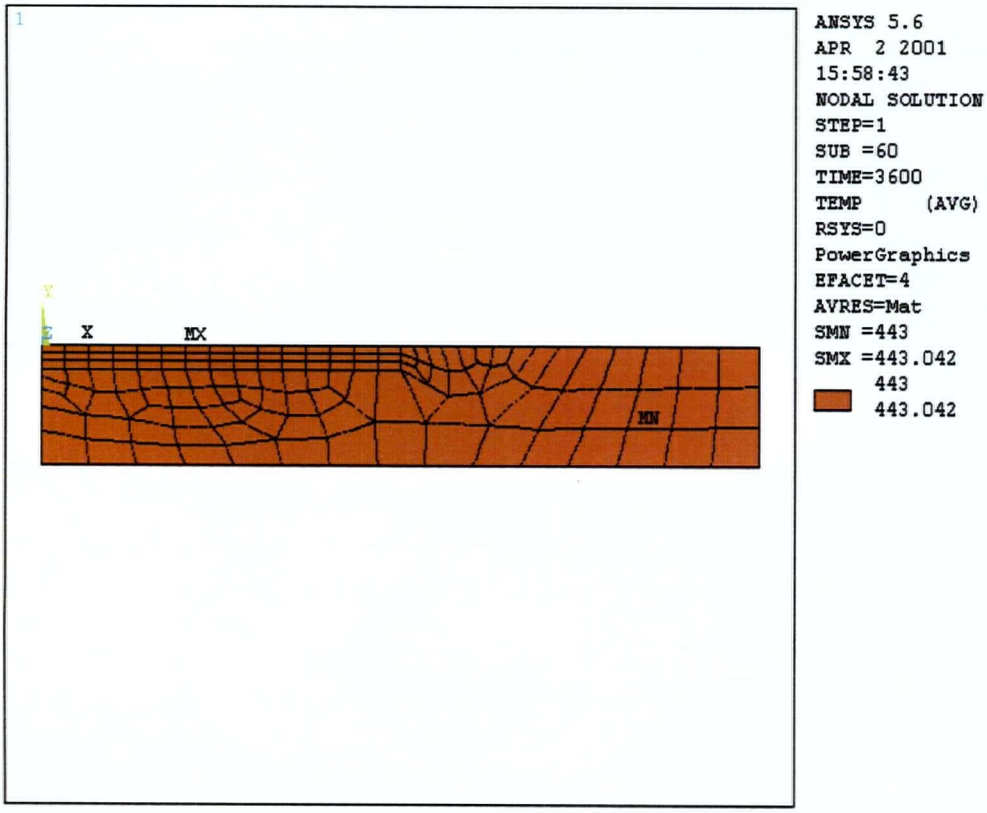

Figure C5: Temperature distribution in the submodel after 60 minutes - shows that the grid region will acquire a temperature of about 443 K. The grid region is the one with uniform-sized rectangular elements. The region of this submodel is a portion of the main model in the vicinity of the grid.

APPENDIX: D

MICROGRAPH DATA

D.1 Selected Micrographs

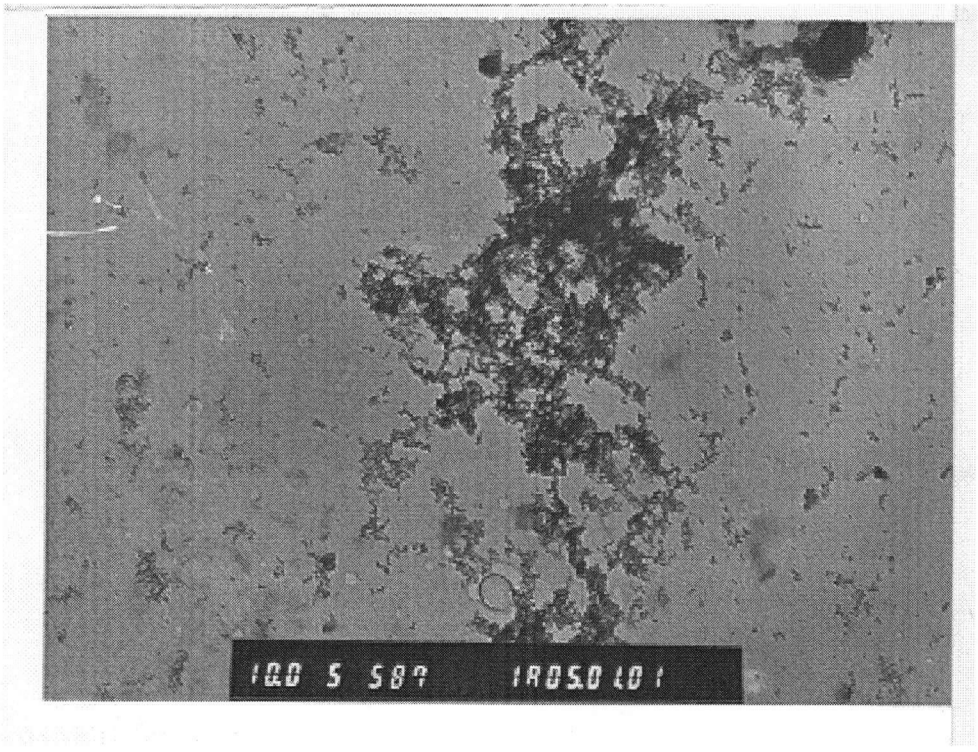

Figure D5-587 (Picture-width = 9.2 μm)

Figure D5-589 (Picture-width = 4.6 μm)

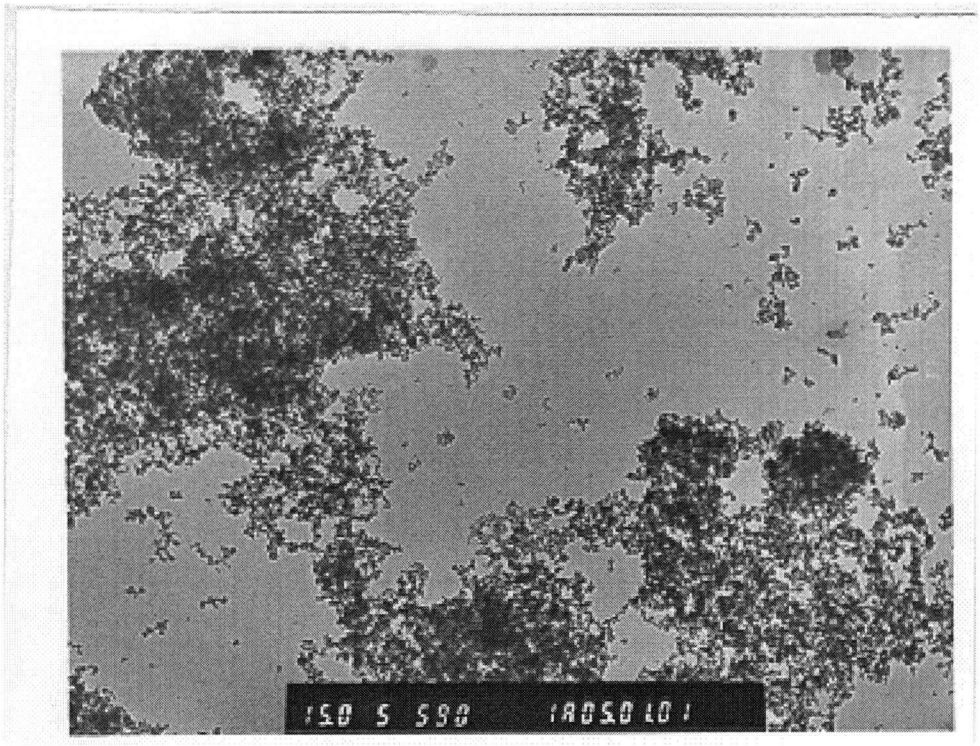

Figure D5-590 (Picture-width = 6.1364 μm)

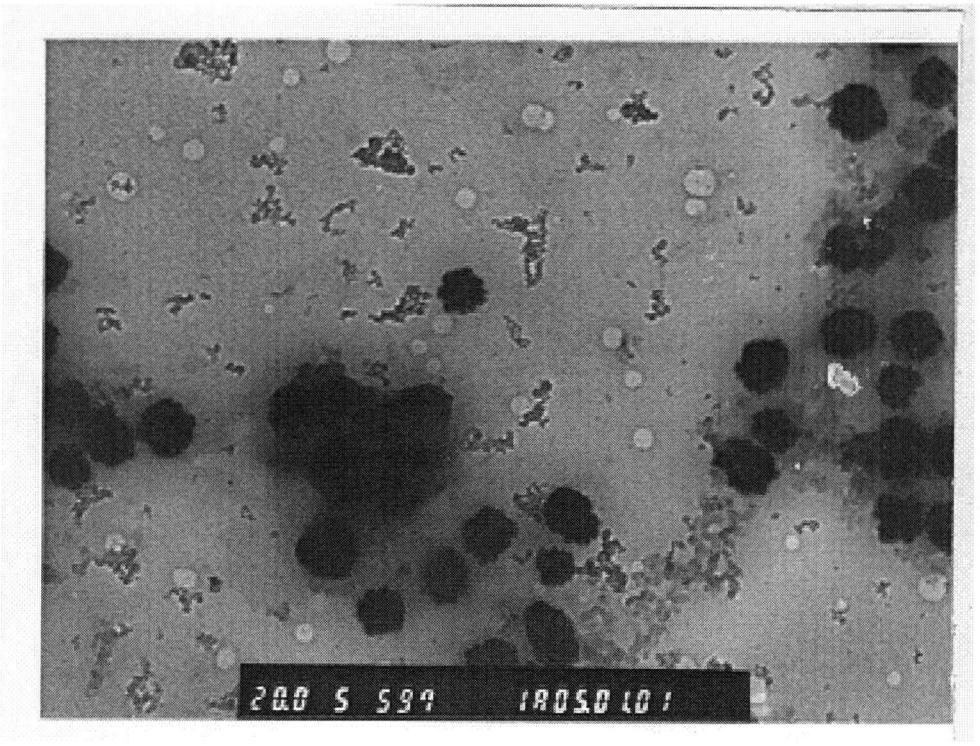

Figure D5-597 (Picture-width = 4.6 μm)

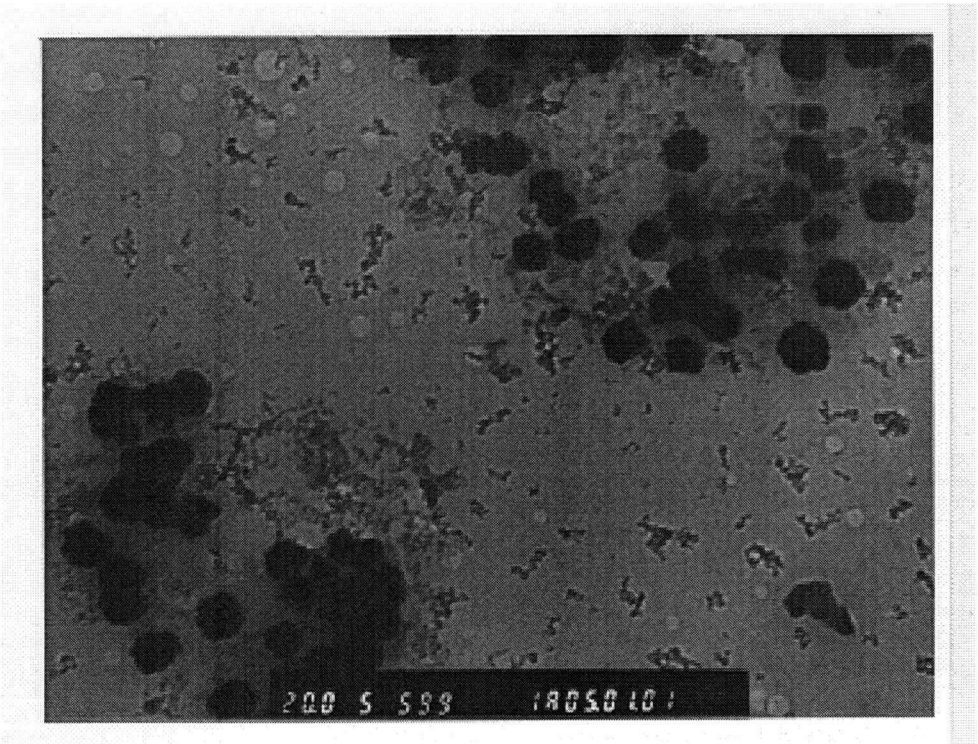

Figure D5-599 (Picture-width = 4.6 μm)

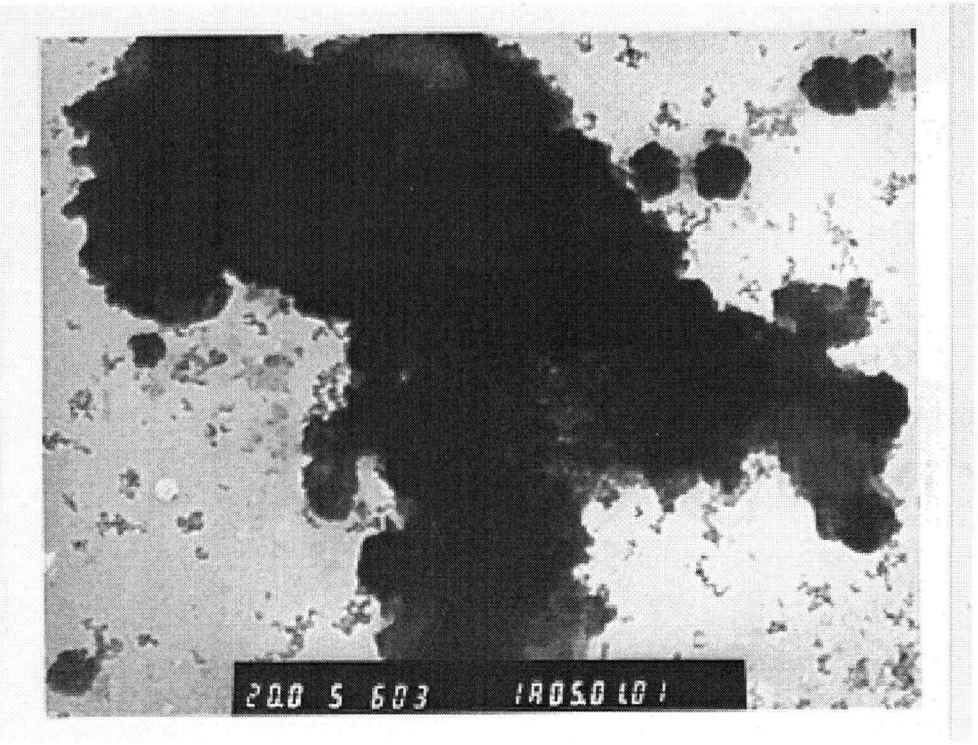

Figure D5-603 (Picture-width = 4.6 μm)

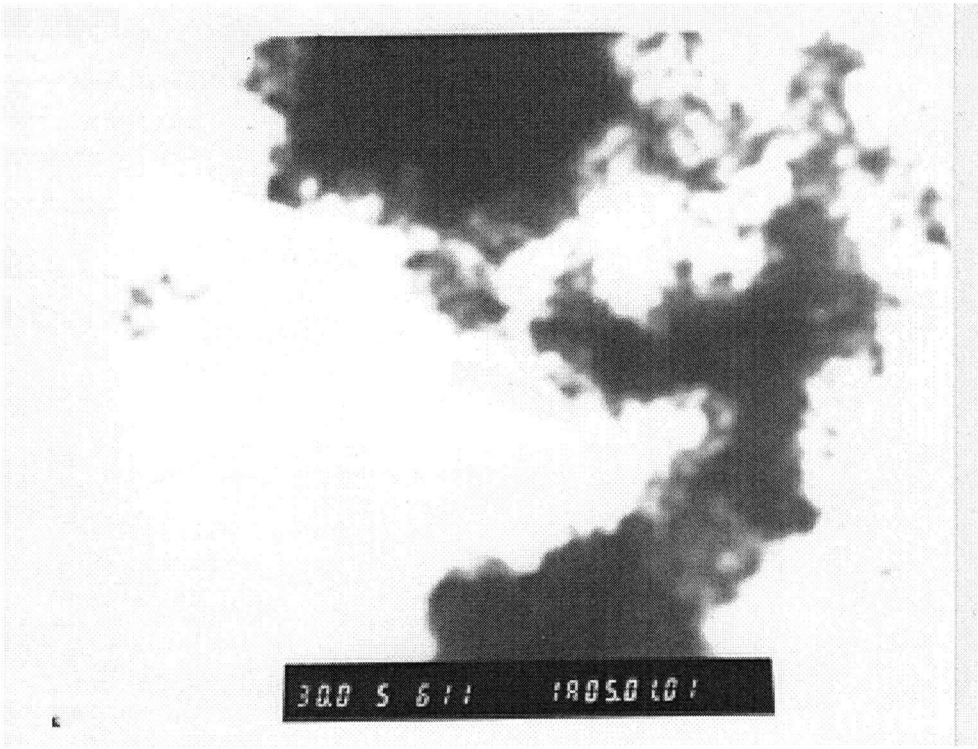

Figure D5-611 (Picture-width = 3.0636 μm)

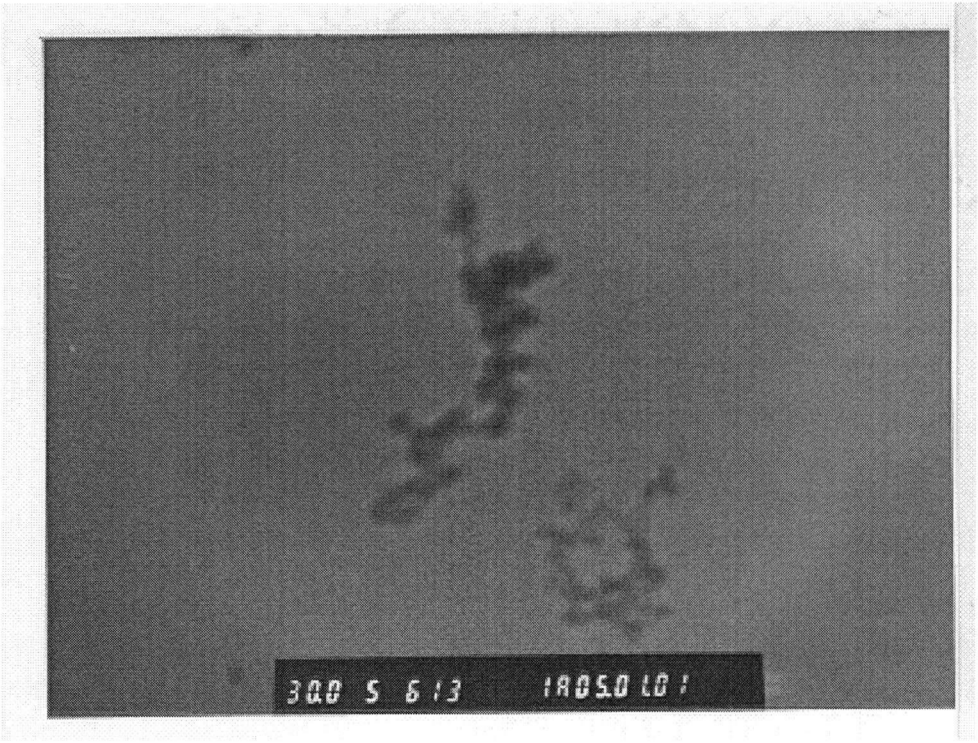

Figure D5-613 (Picture-width = 3.0636 μm)

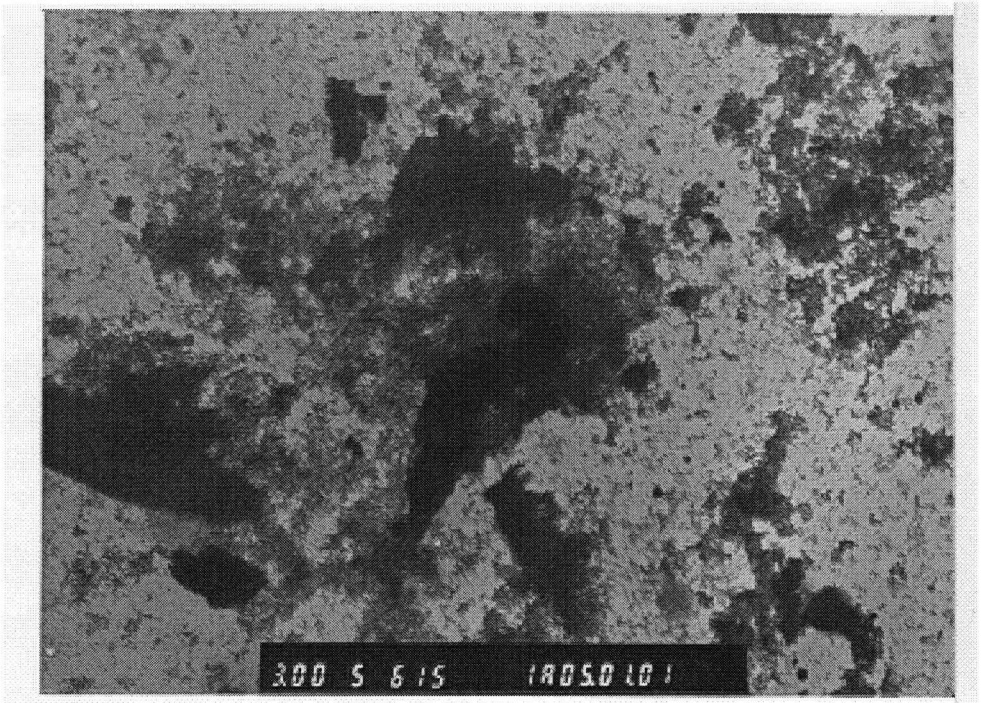

Figure D5-615 (Picture-width = 30.636 μm)

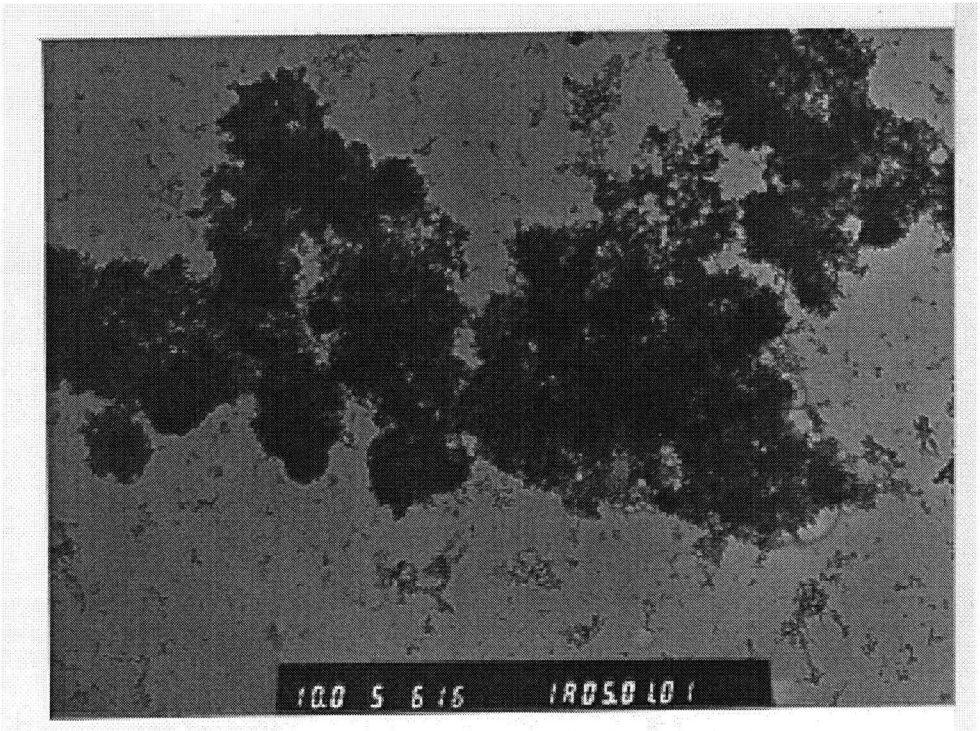

Figure D5-616 (Picture-width = 9.2 μm)

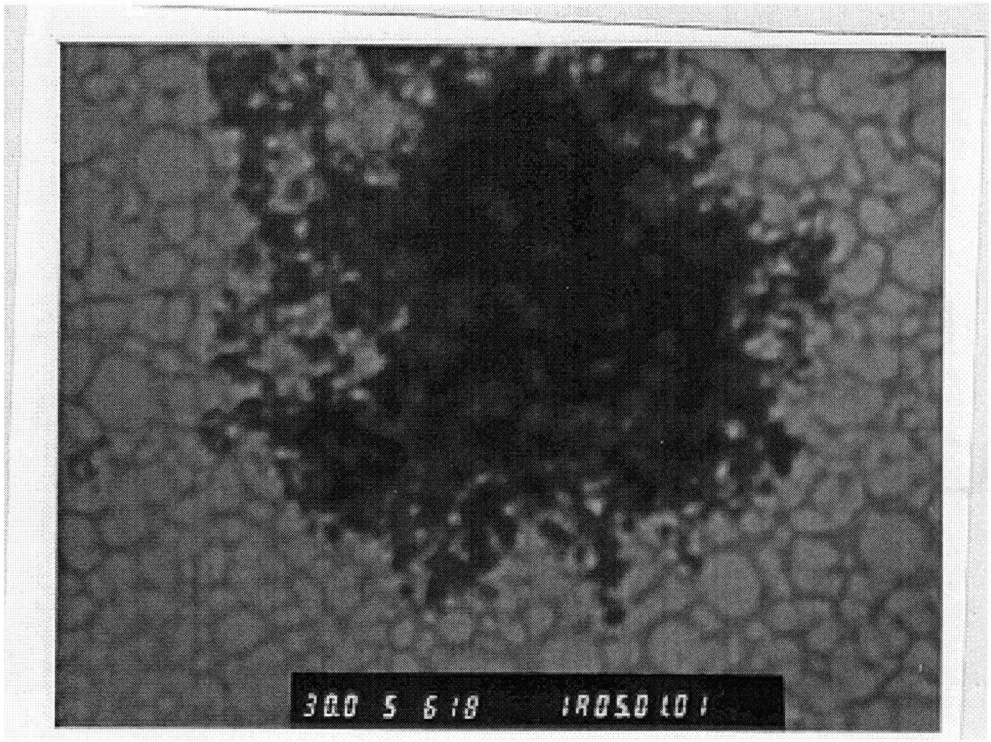

Figure D5-618 (Picture-width = 3.0636 μm)

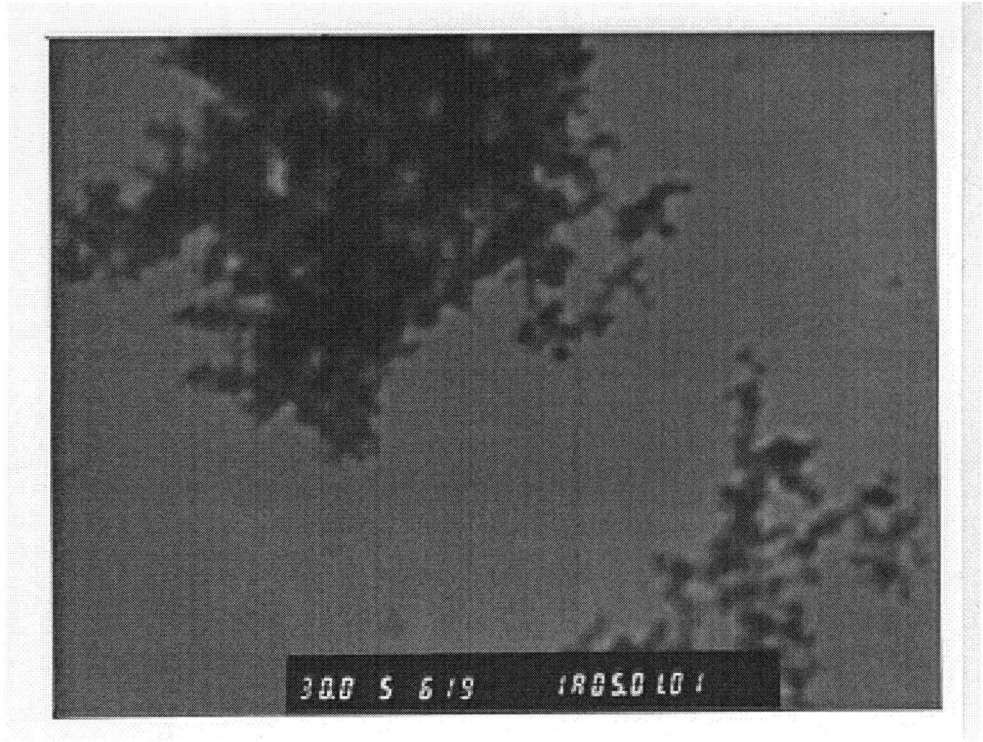

Figure D5-619 (Picture-width = 3.0636 μm)

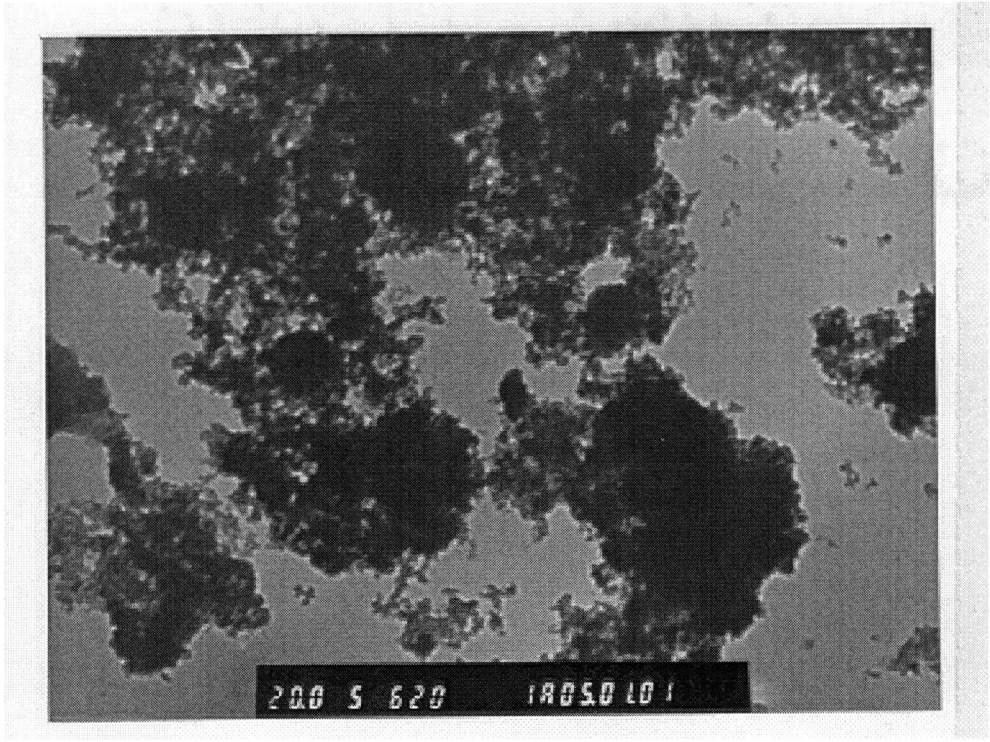

Figure D5-620 (Picture-width = 4.6 μm)

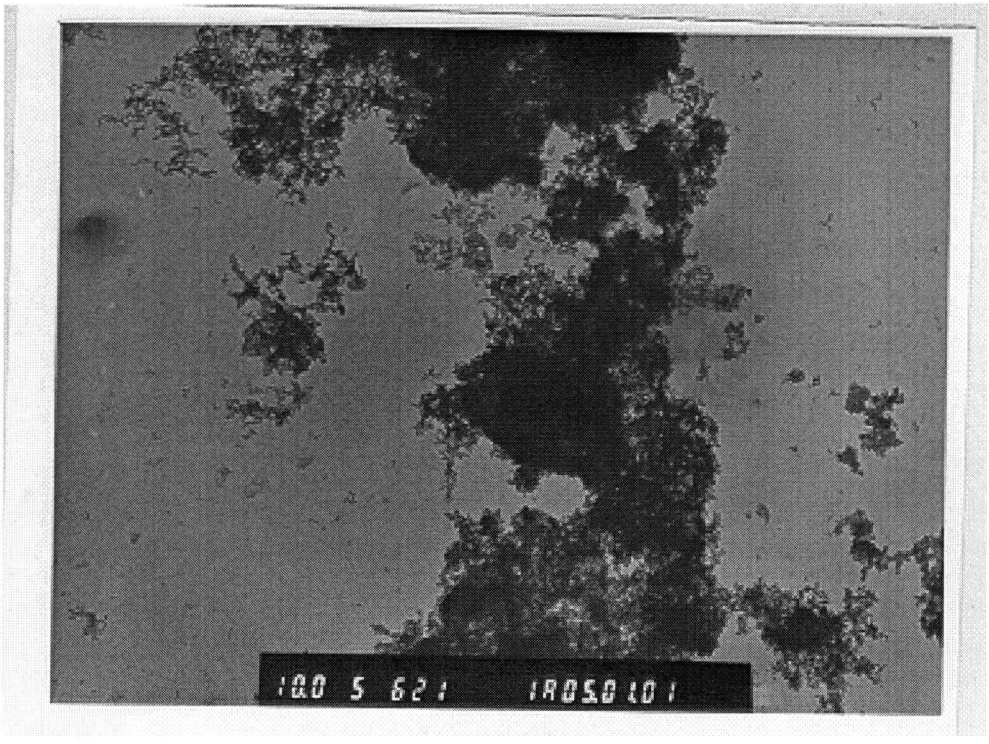

Figure D5-621 (Picture-width = 9.2 μm)

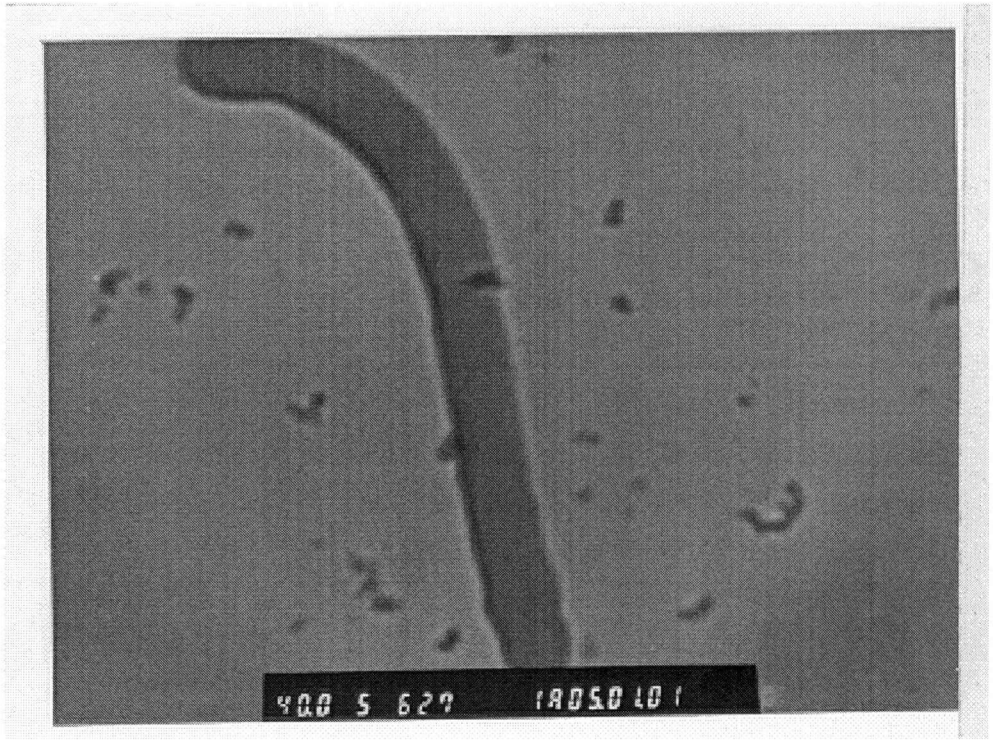

Figure D5-627 (Picture-width = 2.3 μm)

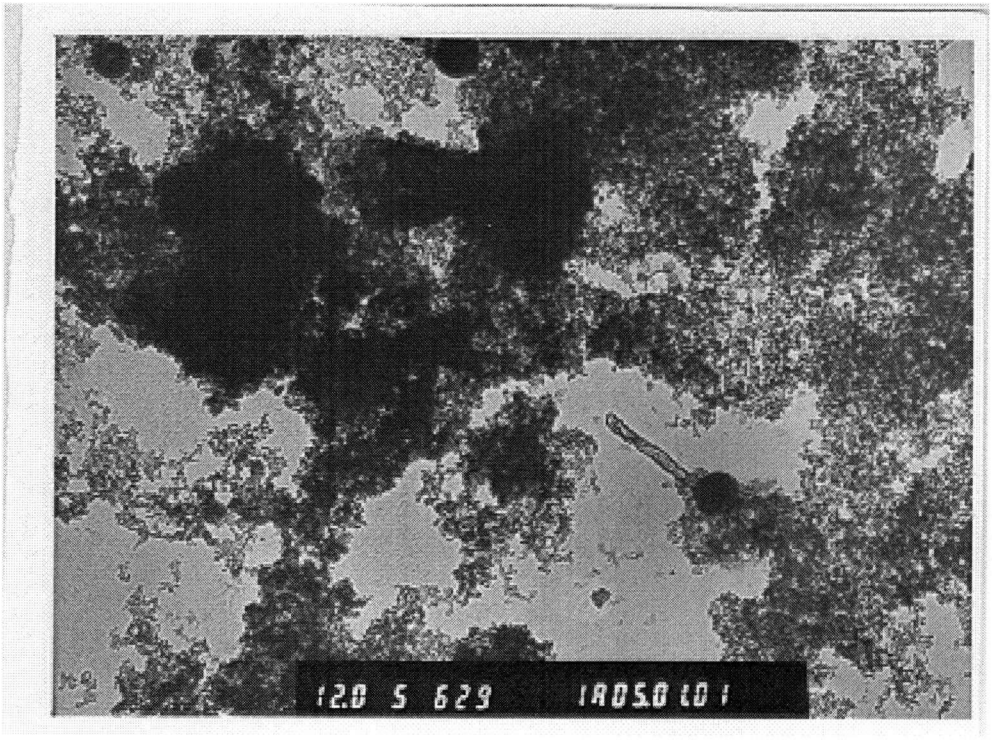

Figure D5-629 (Picture-width = 7.6636 μm)

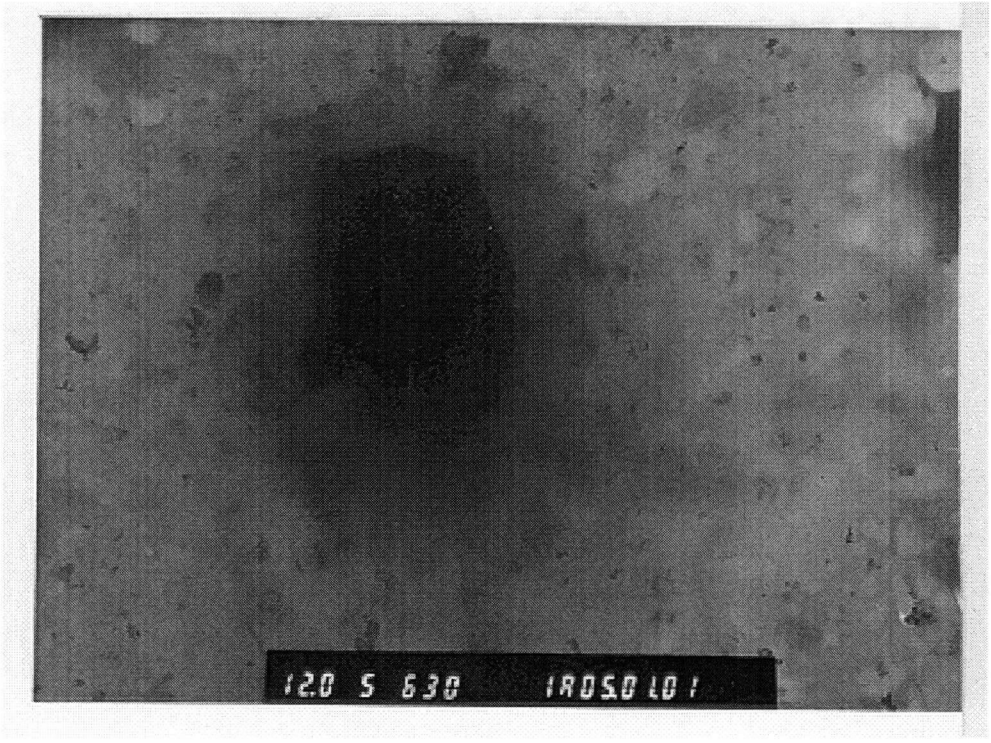

Figure D5-630 (Picture-width = 7.6636 μm)

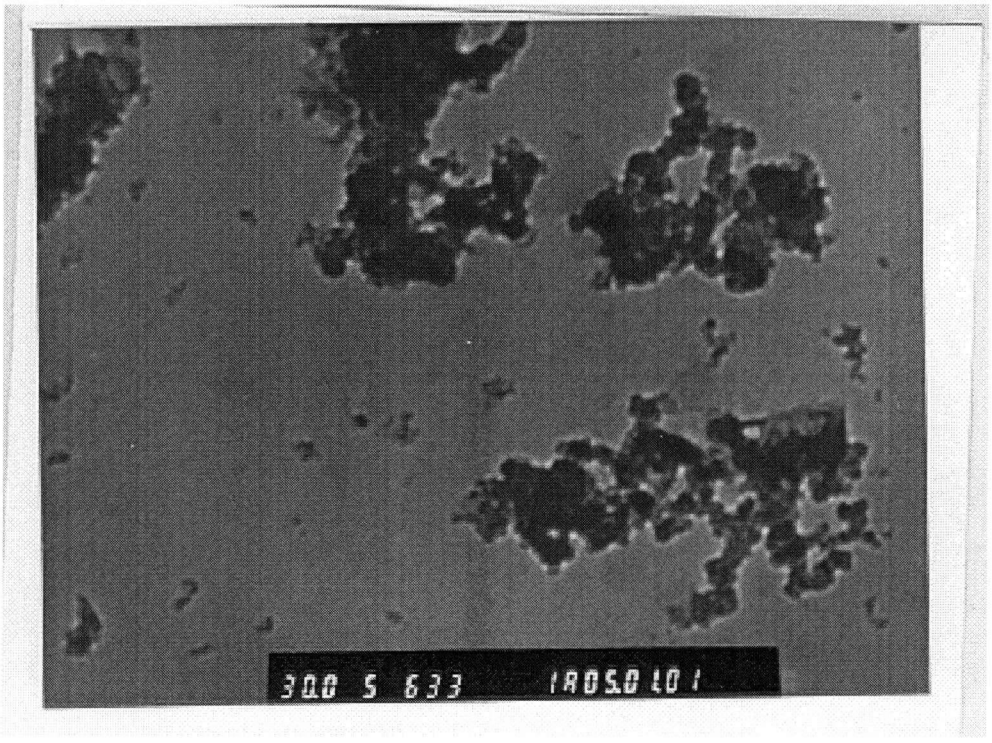

Figure D5-633 (Picture-width = 3.0636 μm)

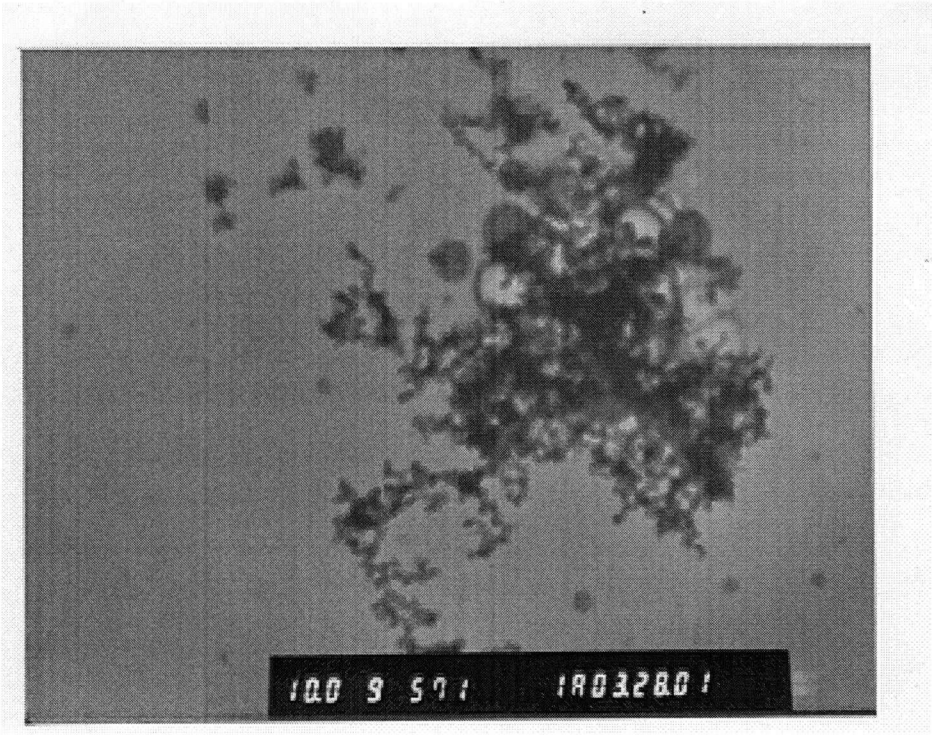

Figure D9-571 (Picture-width = 8 μm)

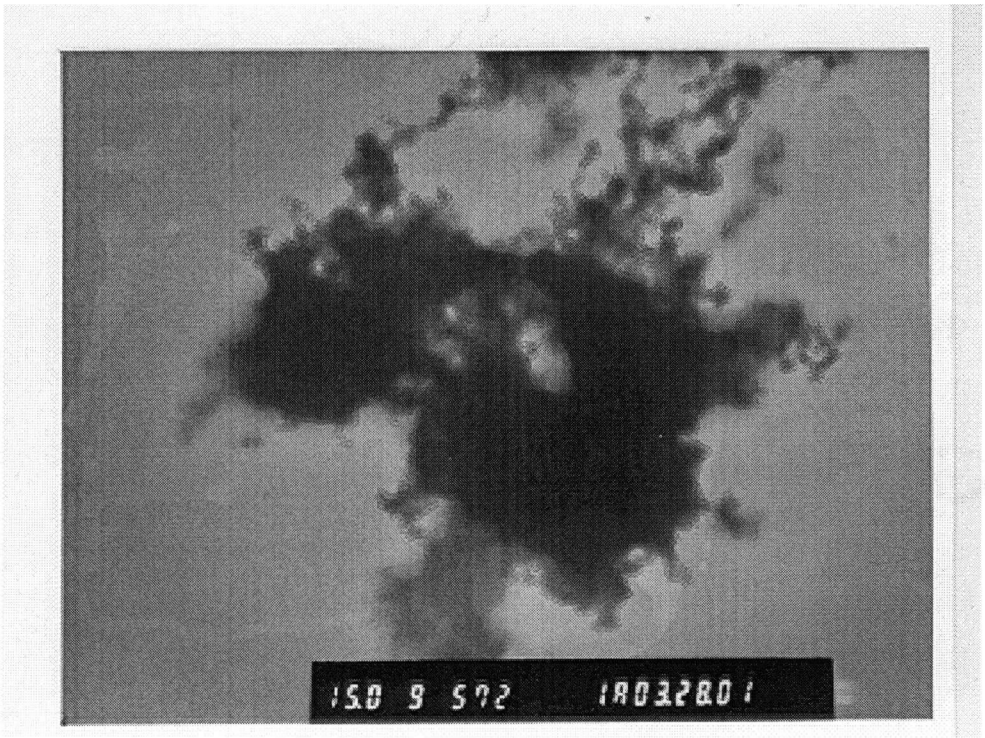

Figure D9-572 (Picture-width = 5.336 μm)

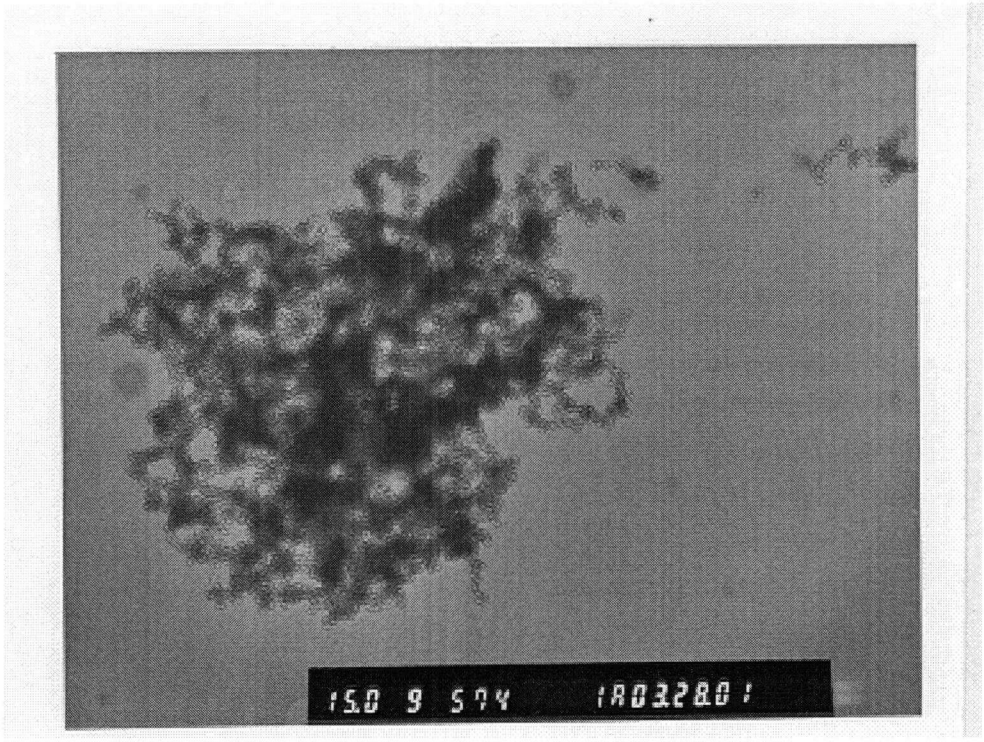

Figure D9-574 (Picture-width = 5.336 μm)

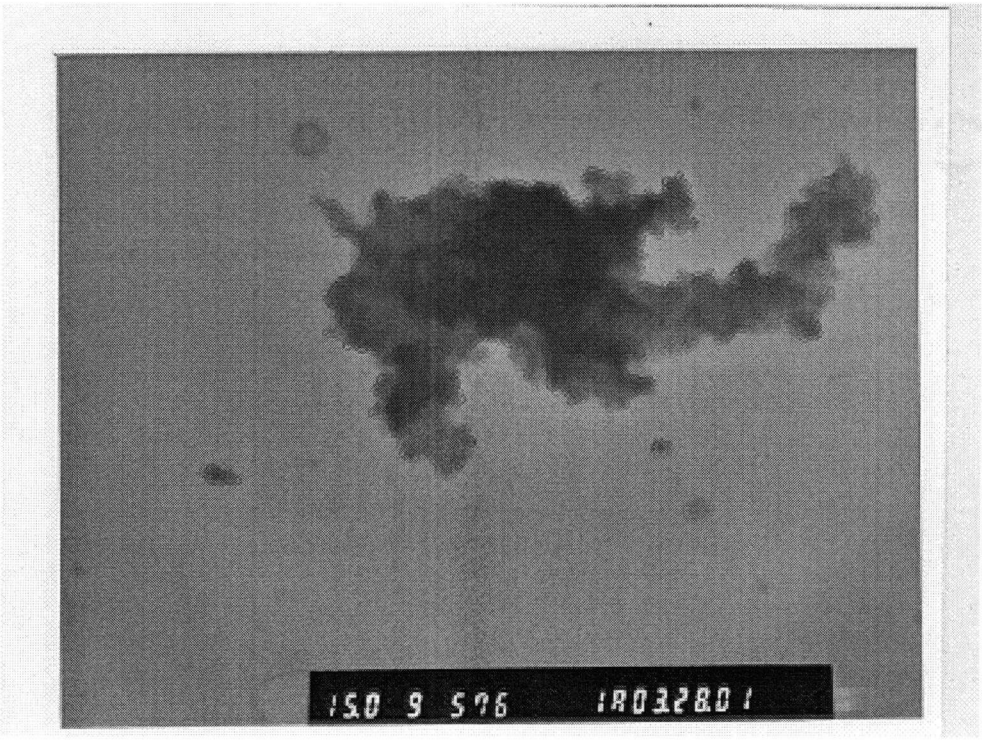

Figure D9-576 (Picture-width = 5.336 μm)

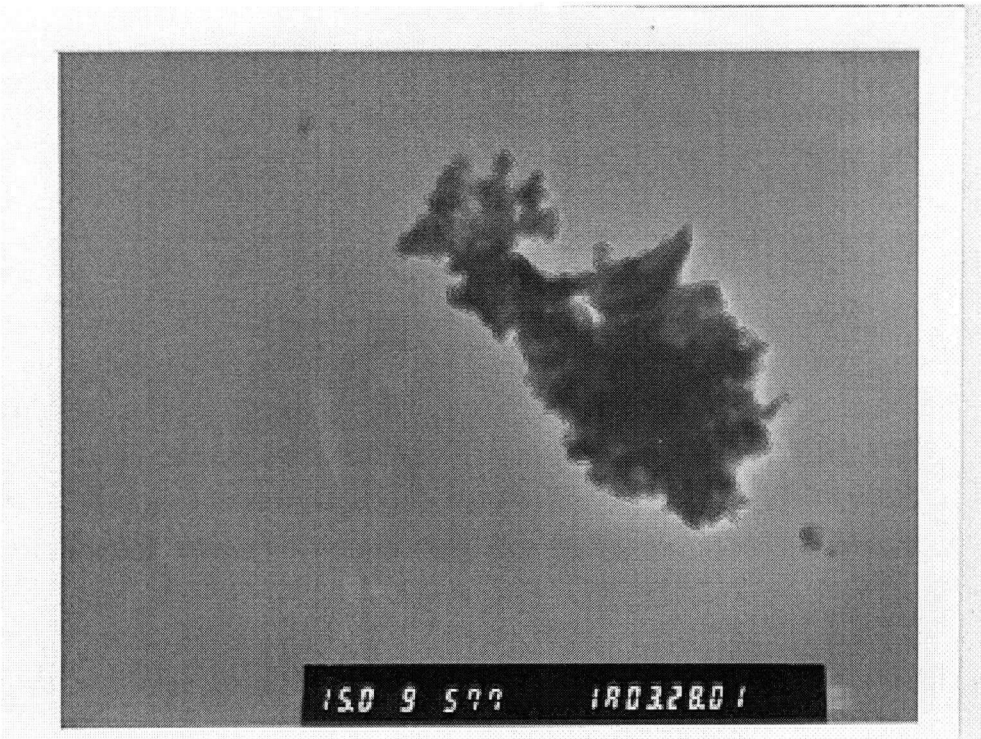

Figure D9-577 (Picture-width = 5.336 μm)

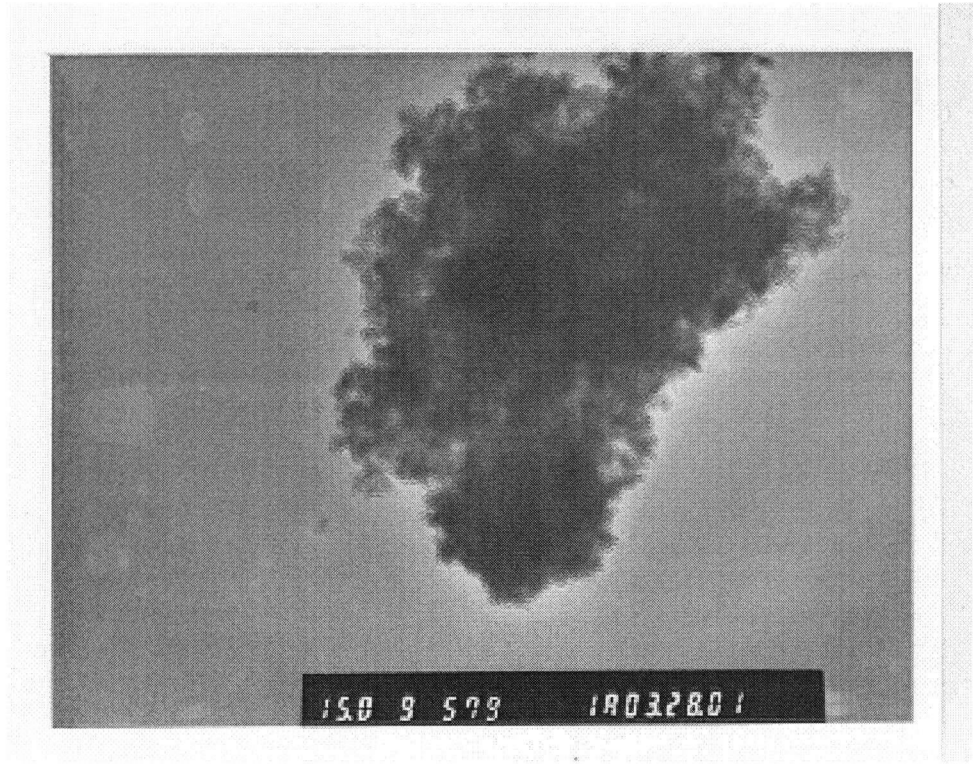

Figure D9-579 (Picture-width = 5.336 μm)

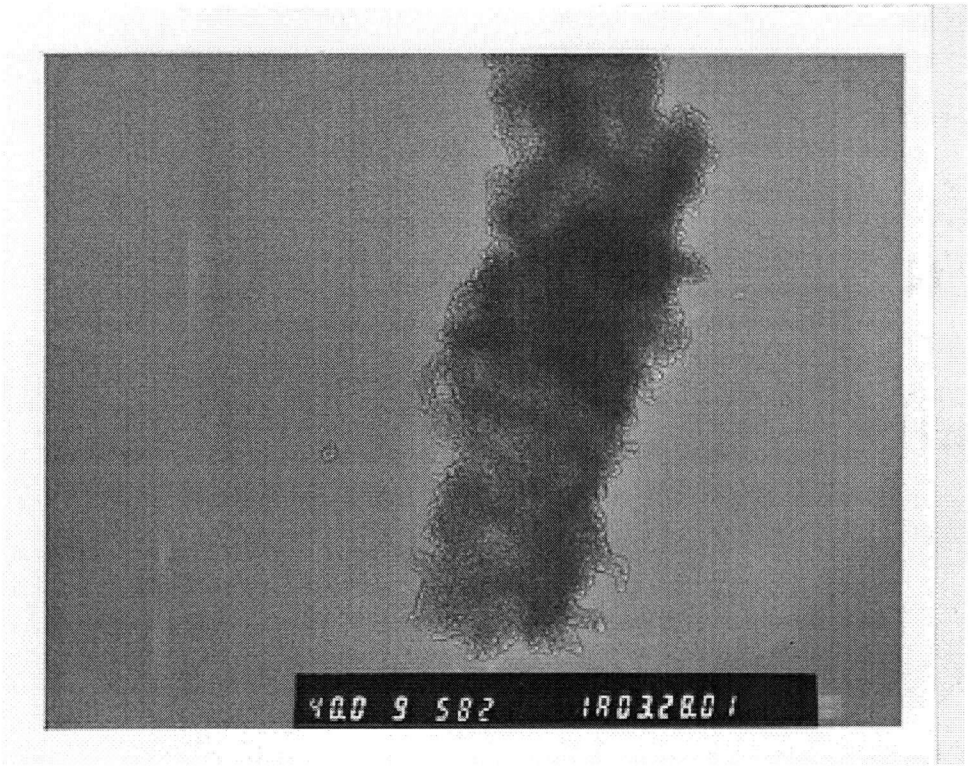

Figure D9-582 (Picture-width = 2 μm)

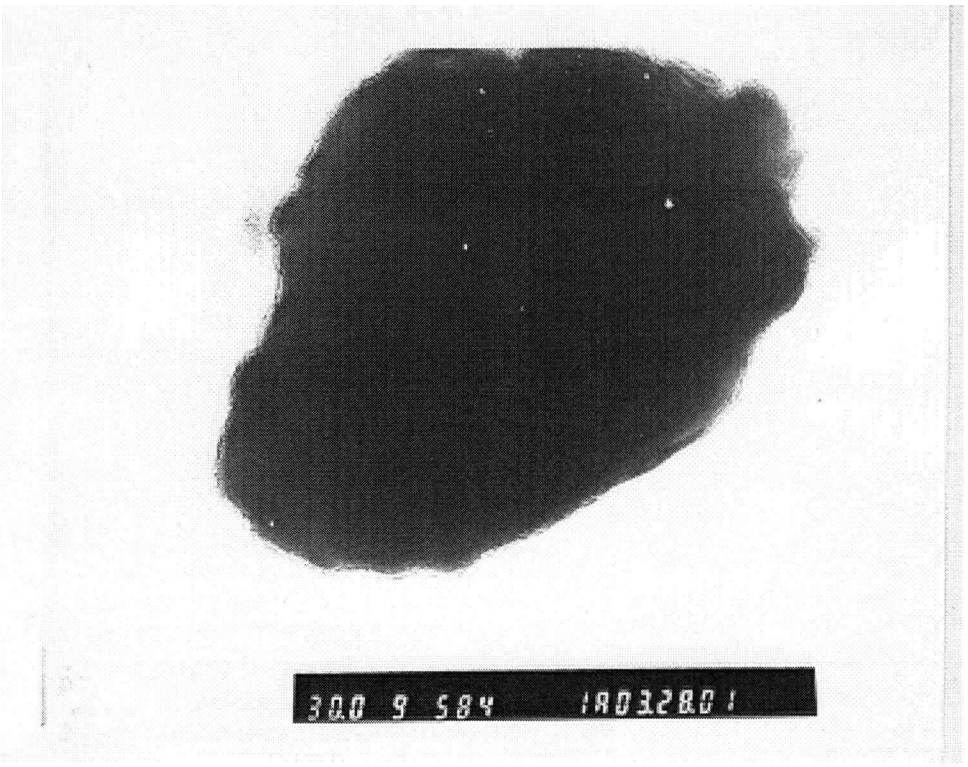

Figure D9-584 (Picture-width = 2.664 μm)

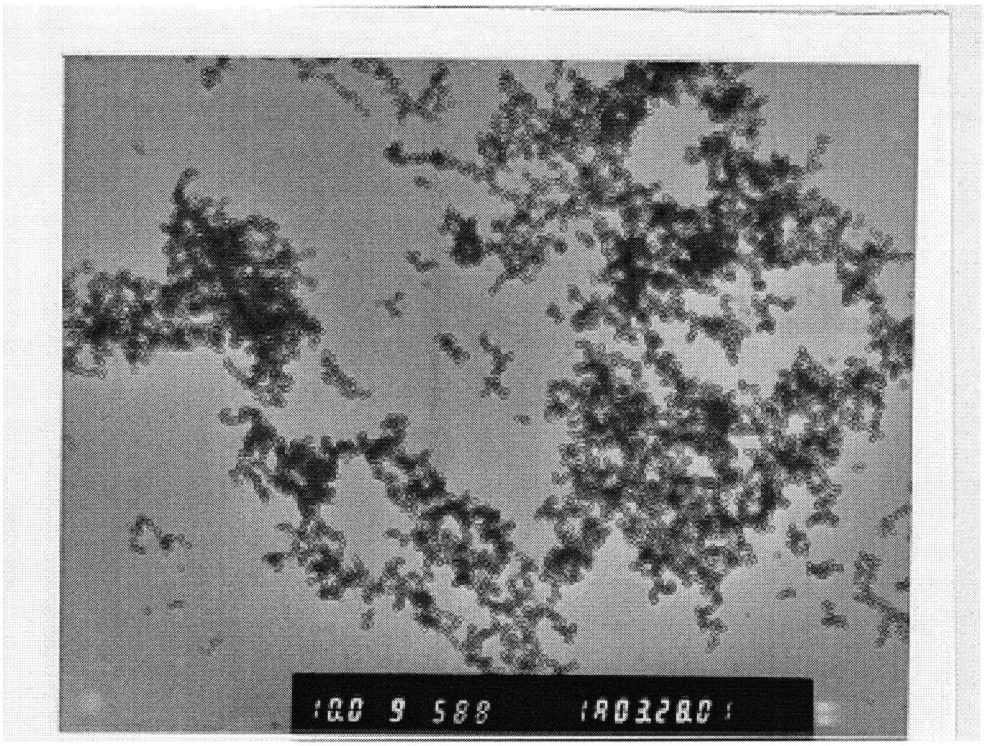

Figure D9-588 (Picture-width = 8 μm)

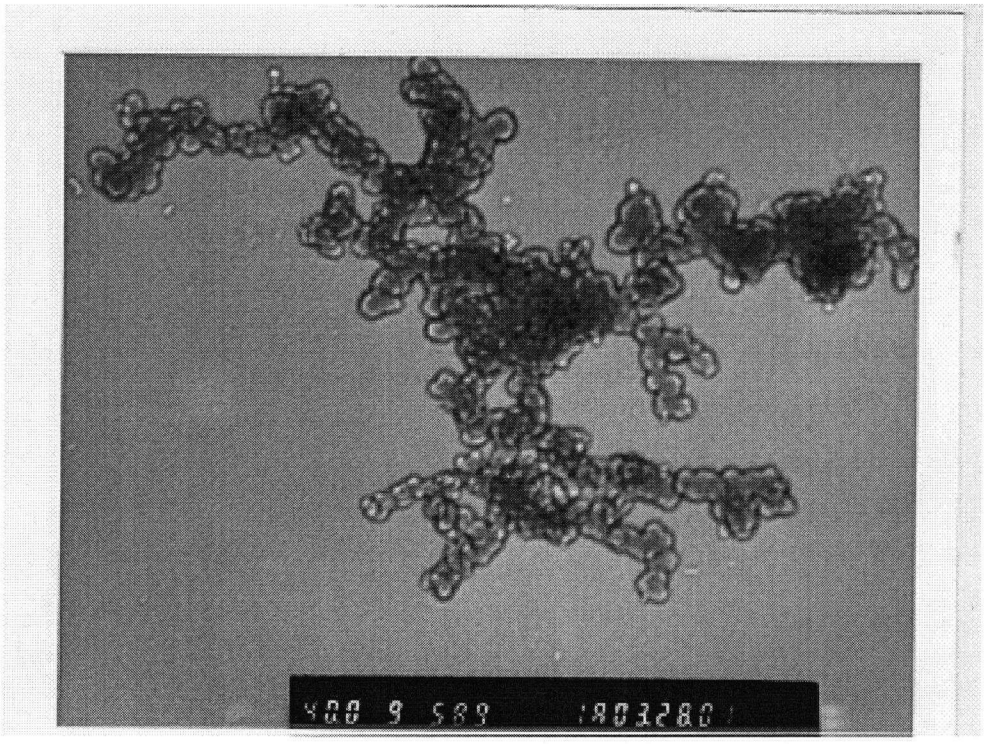

Figure D9-589 (Picture-width = 2 μm)

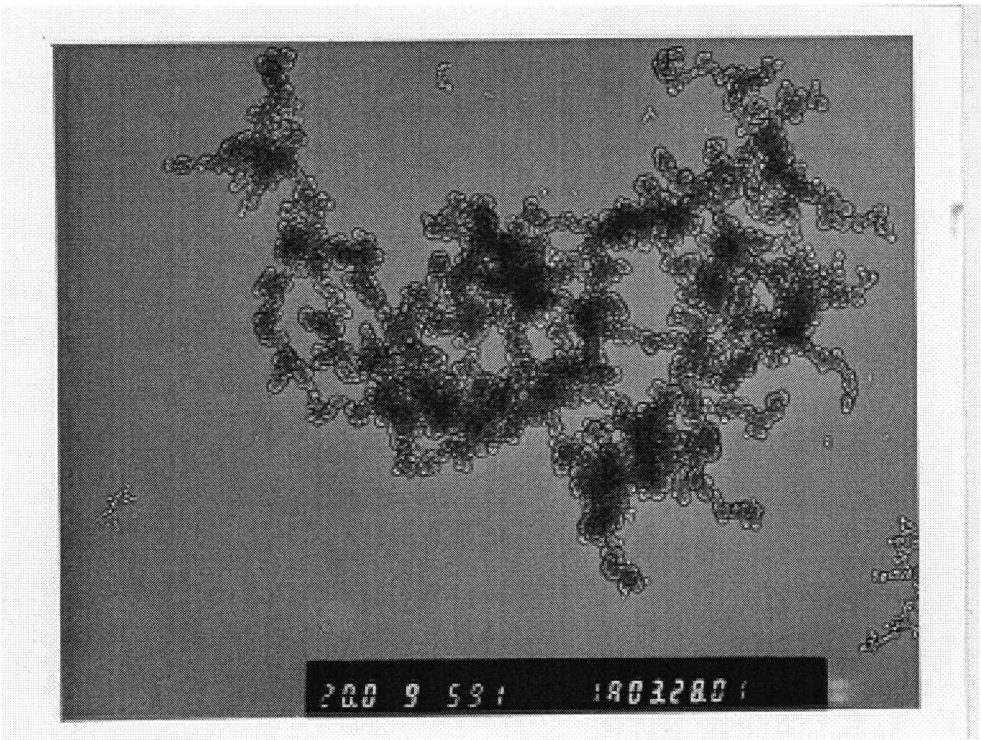

Figure D9-591 (Picture-width = 4 μm)

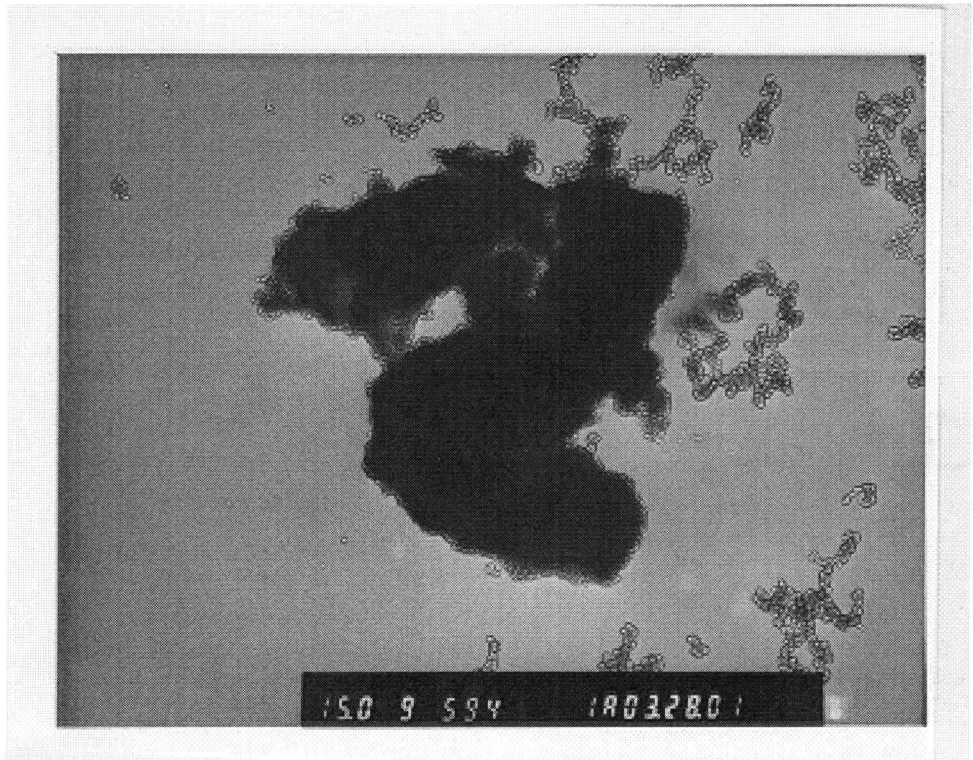

Figure D9-594 (Picture-width = 5.336 μm)

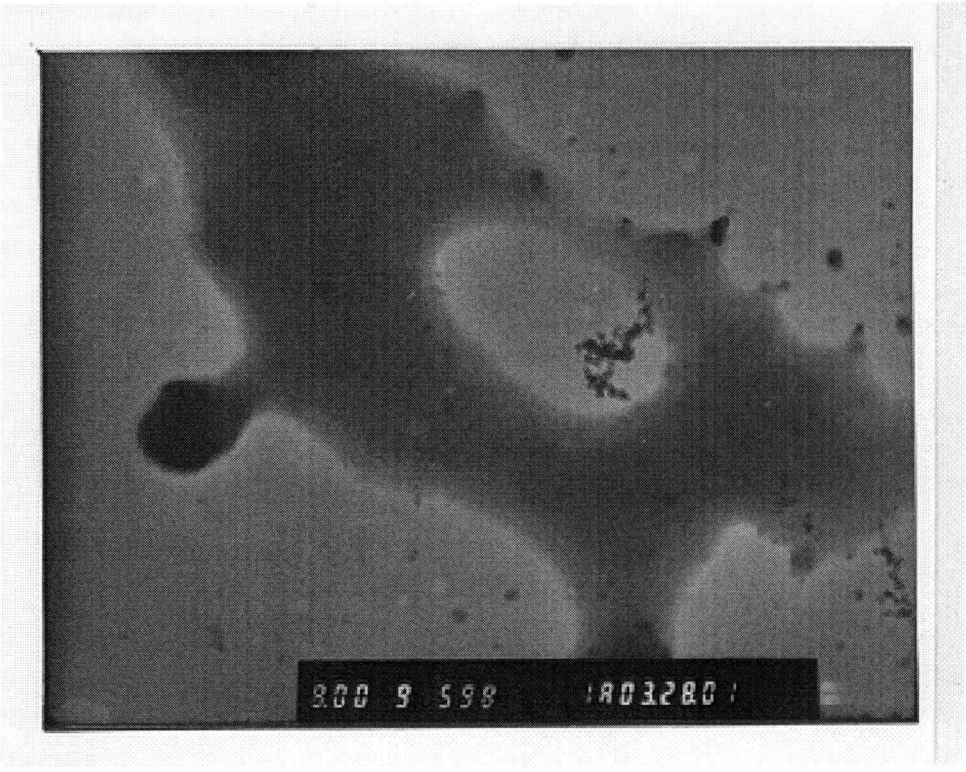

Figure D9-598 (Picture-width = 10 μm)

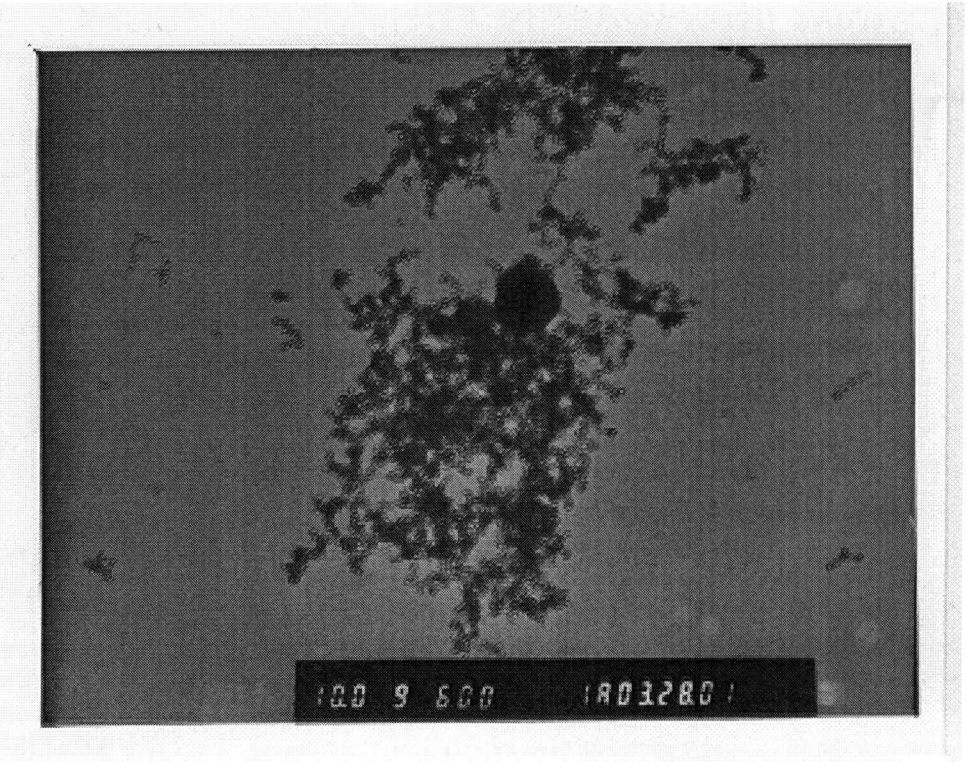

Figure D9-600 (Picture-width = 8 μm)

D.2 Magnification and relative sizes of particles in micrographs

Different magnification values were used for taking pictures of particles using the Transmission Electron Microscope. The selection of magnification was case-dependent with more emphasis on the clarity and relative sizes of particles. The various values of magnification used were 3K, 4K, 5K, 8K, 10K, 12K, 15K, 20K, 30K, 40K and 60K (For example, 20K means 20,000 times the size of the original particle). The error in magnification for the TEM could be ± 5%. The maximum value of magnification attainable using TEM was 600K. But the clarity of particles had to be compromised in most cases after 60 K. The following table shows the size-representation in the negatives of the micrographs (these are not strictly applicable to the micrographs given in section D.1 since they are not of the exact sizes of corresponding negatives).

TEM magnification (in terms of K)	Dimension in nm represented by 1 cm in the negative of micrograph
3	3333
4	2500
5	2000
8	1250
10	1000
12	833
15	667
20	500
30	333
40	250
60	167
100	100
600	17

D.3 Details of all micrographs taken

A total of 103 pictures were taken from different samples from both engines. Out of these, 81 micrographs were taken under test conditions for detailed analysis.

Sl. No.	Micrograph Number	Engine	Sampling condition of engine
1	5-586	A	75% load and 1800 RPM
2	5-587	A	"
3	5-588	A	"
4	5-589	A	"
5	5-590	A	"
6	5-591	A	"
7	5-592	A	"
8	5-593	A	"
9	5-594	A	"
10	5-595	A	"
11	5-596	A	"
12	5-597	A	"
13	5-598	A	"
14	5-599	A	"
15	5-600	A	"
16	5-601	A	"
17	5-602	A	"
18	5-603	A	"
19	5-604	A	"
20	5-605	A	"
21	5-606	-	Grid placed with sampled ones, but which was not used for sampling
22	5-607	-	"
23	5-608	-	"
24	5-609	-	Grid without exposure to sampled ones and which was not used for sampling
25	5-610	-	"
26	5-611	A	5% load and 1800 RPM
27	5-612	A	"
28	5-613	A	"
29	5-614	A	"
30	5-615	A	85% load and 1800 RPM
31	5-616	A	"
32	5-617	A	"
33	5-618	A	25% load and 1800 RPM
34	5-619	A	"
35	5-620	A	50% load and 1800 RPM
36	5-621	A	"
37	5-622	A	"
38	5-623	A	50% load and 1500 RPM
39	5-624	A	"

40	5-625	A	"
41	5-626	A	"
42	5-627	A	"
43	5-628	A	"
44	5-629	A	"
45	5-630	A	50% load and 1600 RPM
46	5-631	A	"
47	5-632	A	50% load and 1700 RPM
48	5-633	A	"
49	9-568	B	Pilot pulse-width at 1.1 ms
50	9-569	B	"
51	9-570	B	"
52	9-571	B	"
53	9-572	B	"
54	9-573	B	"
55	9-574	B	"
56	9-575	B	"
57	9-576	B	"
58	9-577	B	Pilot pulse-width at 0.48 ms
59	9-578	B	"
60	9-579	B	"
61	9-580	B	"
62	9-581	B	"
63	9-582	B	"
64	9-583	B	"
65	9-584	B	"
66	9-585	B	"
67	9-586	B	Pilot pulse-width at 0.65 ms
68	9-587	B	"
69	9-588	B	"
70	9-589	B	"
71	9-590	B	"
72	9-591	B	"
73	9-592	B	"
74	9-593	B	"
75	9-594	B	"
76	9-595	B	"
77	9-596	B	"
78	9-597	B	"
79	9-598	B	"
80	9-599	B	"
81	9-600	B	"

In addition to this, 22 pictures were taken from samples collected during preliminary tests to optimize the conditions for the sampler. None of these pictures are given in section D.1 or mentioned in Chapter 2, since detailed analyses were not done on the samples. All the pictures show particles from Engine A, with which the tests were carried out. The details of the pictures are given below.

Sl. No.	Micrograph Number	Serial Number for conditions of the tests as given in Table 2.1
1	9-503	2
2	9-504	"
3	9-505	"
4	9-506	"
5	9-507	"
6	9-508	"
7	9-509	"
8	9-510	"
9	9-511	"
10	9-512	"
11	9-513	3
12	9-514	"
13	9-515	"
14	9-516	"
15	9-517	"
16	9-518	1
17	9-519	4
18	9-520	"
19	9-521	6
20	9-522	5
21	9-523	7
22	9-524	8

APPENDIX: E

DESCRIPTION OF ALL ELECTRONIC DATA

The following table indicates the details of all data stored electronically. All the files are available in the hard disk of "ENERGIA".

Sl. No.	Filename	Description
1	c:\Anil\MASc-Thesis\Westport\Engine A	Directory of data files for Engine A
2	c:\Anil\MASc-Thesis\Westport\Engine B	Directory of data files for Engine B
3	c:\Anil\MASc-Thesis\Westport \Grid collection.xls	MS Excel file for design calculations of deposition rate and efficiency
4	c:\Anil\MASc-Thesis\Westport \Test Modes.doc	MS Word file indicating the possible test-modes in HPDI engines
5	c:\Anil\MASc-Thesis\Westport \Test-records.doc	MS Word file for the test recording sheet for the preliminary round of tests
6	c:\Anil\MASc-Thesis\Thesis-Structure \FEM files	Directory of all source files for finite element modelling of the sampler using ANSYS
7	c:\Anil\MASc-Thesis\Thesis-Structure \Text	Directory of all files in the text portion of the thesis
8	c:\Anil\MASc-Thesis\Thesis-Structure \Appendices	Directory of all files in the appendices of the thesis (includes FEM results, figures, Scanned micrographs, Design calculations, FEM model assignment and information on micrographs

Contact address for further details: ***anil_global@hotmail.com***